

---

Unterschrift des Betreuers



TECHNISCHE  
UNIVERSITÄT  
WIEN  
Vienna University of Technology

## DIPLOMARBEIT

# Search for supersymmetry in the single lepton final state in 13 TeV pp collisions with the CMS experiment

Ausgeführt am Atominstitut der Technischen Universität Wien  
in Verbindung mit dem Institut für Hochenergiephysik (HEPHY)  
der Österreichischen Akademie der Wissenschaften

unter der Anleitung von  
Univ.Prof. Dipl.-Phys. Dr.rer.nat. Jochen Schieck  
und  
Dipl.-Ing. Dr.techn. Robert Schöffbeck

durch

Daniel Spitzbart

Deinhardsteingasse 29/34  
1160 Wien

---

Datum

---

Unterschrift



*“Look closely. The beautiful may be small.”*

Immanuel Kant



# Abstract

Supersymmetry is among the most promising theories of physics beyond the Standard Model, but until now any direct evidence in its support is still missing. A search for events with a single charged lepton in the final state, coming from supersymmetric processes, is performed using proton-proton collision data taken by the CMS experiment at the CERN LHC in the 2015 run with a center of mass energy of 13 TeV. The integrated luminosity of the dataset corresponds to  $2.3\text{fb}^{-1}$ .

The signal model describes gluino pair production with masses in the TeV range. The cascade decay of each gluino involves production of 1st and 2nd generation quark jets and a neutral stable supersymmetric particle in the final state, the lightest neutralino, which provides a significant amount of missing transverse energy. Exactly one charged lepton is required in the final state, which comes from the decay of one of the involved W bosons. At the same time, multijet events are highly suppressed by this requirement. The other W boson will decay hadronically.

After applying a baseline selection to suppress the bulk of background events, the remaining events are split into a few signal regions with different kinematic requirements. A robust method to estimate background events from Standard Model processes using control samples in data is then introduced. This method is validated both in simulated samples and in data. Systematic uncertainties of the background prediction and simulated signal samples are studied.

The observation in the signal regions is in good agreement with the expectation from the Standard Model. Therefore, exclusion limits on gluino and neutralino masses of the tested model are set. Gluinos with masses up to 1400 GeV and neutralinos up to 850 GeV are excluded with 95% confidence level in the considered model, improving previous mass limits by several hundred GeVs.



# Kurzfassung

Supersymmetrie ist eine der vielversprechendsten Theorien zur Erweiterung des Standardmodells der Teilchenphysik, bisher gibt es aber keine direkten experimentellen Hinweise zu ihren Gunsten. Eine Suche nach supersymmetrischen Ereignissen mit einem geladenen Lepton im Endzustand wird mit Daten von Proton-Proton Kollisionen im CMS Experiment am CERN LHC durchgeführt. Die Daten, welche einer integrierten Luminosität von  $2.3\text{fb}^{-1}$  entsprechen, wurden während des Laufs im Jahr 2015 bei einer Schwerpunktsenergie von 13 TeV aufgezeichnet.

Das Signalmodell beschreibt die paarweise Produktion von Gluinos mit Massen im TeV Bereich. Der Kaskadenzerfall der Gluinos beinhaltet jeweils die Produktion von leichten Quarkjets sowie ein neutrales, stabiles supersymmetrisches Teilchen im Endzustand, das leichteste Neutralino. Da das Neutralino elektrisch nicht geladen ist und nur schwach wechselwirkt, kann es im CMS Detektor nicht direkt nachgewiesen werden, es erhöht jedoch das Impulsungleichgewicht. Genau ein geladenes Lepton im Endzustand vom Zerfall eines der involvierten W Bosonen wird vorausgesetzt. Diese Voraussetzung reduziert die Anzahl von QCD Multijet Prozessen erheblich, welche einen Großteil der Ereignisse bei Proton-Proton Kollisionen ausmachen. Das andere W Boson zerfällt hadronisch.

Ein Großteil der Hintergrundereignisse wird durch kinematische Grundvoraussetzungen unterdrückt. Die verbleibenden Ereignisse werden in mehrere Signalregionen aufgeteilt. Eine robuste Methode zur Abschätzung der Rate an Hintergrundprozessen aus Standardmodell Ereignissen in diesen Signalregionen, basierend auf Daten aus Kontrollregionen, wird vorgestellt. Die Methode wird sowohl mittels simulierter Pseudodaten als auch gemessener Daten verifiziert. Systematische Unsicherheiten der Hintergrundabschätzung und der simulierten Signalsamples werden diskutiert und ermittelt.

Die Anzahl der gemessenen Datenereignisse wird gut von der erwarteten Anzahl an Standardmodell Hintergrundereignissen beschrieben. Daher werden Massengrenzen für Gluinos und Neutralinos mit einem Konfidenzintervall von 95% bestimmt. Gluinos mit Massen bis zu 1400 GeV und Neutralinos bis zu 850 GeV werden ausgeschlossen, was eine Verbesserung der Massengrenzen um bis zu mehreren hundert GeV ergibt.





# Acknowledgements

After one intense year of work on the topic of this thesis a few words of gratitude are more than appropriate. First I want to thank my supervisor and director of HEPHY, Jochen Schieck, for the opportunity to work in this interesting and challenging field at the frontiers of physics. Many thanks go to Robert Schöfbeck, who encouraged me to write my master's thesis in his analysis group, and always motivates his students to give their absolute best. I want to address special thanks to Wolfgang Adam, who, although only being available remotely most of the time, always took time to discuss and explain problems.

Furthermore I want to thank all the people at HEPHY for an outstanding working atmosphere at the outsourced offices at Wohllebengasse, especially my (frequently changing) office mates David, Ece, Josef, Lukas, Mateusz, Navid and Verena.

Thank you also to all my friends, especially Christopher, Jojo and Matthias, and fellow students.

An especially big thank you goes to my girlfriend Madeleine, who always stood by my side and kept me going in the sometimes stressful phases. Finally, I want to thank all my family: my parents Elisabeth and Ernst, my sisters Christina and Sonja and my brother-in-law Holger for always supporting me in any possible way and reminding me that there are other interesting topics outside physics, too.

Without all of you this would not have been possible.



# Contents

<b>Abstract</b>	<b>iv</b>
<b>Kurzfassung</b>	<b>vii</b>
<b>Acknowledgements</b>	<b>ix</b>
<b>1 Standard Model and Supersymmetry</b>	<b>1</b>
1.1 Standard Model . . . . .	2
1.1.1 The electromagnetic interaction . . . . .	4
1.1.2 The weak interaction . . . . .	5
1.1.3 Electroweak unification and symmetry breaking . . . . .	5
1.1.4 The strong interaction . . . . .	7
1.1.5 Shortcomings of the Standard Model . . . . .	8
1.2 Supersymmetry . . . . .	9
1.2.1 Minimal Supersymmetric Standard Model . . . . .	10
1.2.2 Solution to the hierarchy problem . . . . .	12
1.2.3 Dark matter candidate . . . . .	13
1.2.4 Simplified models . . . . .	13
1.2.5 SUSY after LHC Run 1 . . . . .	14
1.2.6 Expectations for LHC Run 2 . . . . .	16
<b>2 The Large Hadron Collider at CERN</b>	<b>19</b>
2.1 The accelerator complex . . . . .	19
2.2 Features and properties . . . . .	20
<b>3 The CMS experiment at the LHC</b>	<b>23</b>
3.1 Superconducting magnet . . . . .	24
3.2 Tracker . . . . .	25
3.3 Electromagnetic calorimeter . . . . .	26
3.4 Hadronic calorimeter . . . . .	27
3.5 Muon system . . . . .	27
3.6 Trigger and data acquisition system . . . . .	28
<b>4 Event reconstruction and selection</b>	<b>29</b>
4.1 Electrons . . . . .	30
4.2 Muons . . . . .	31
4.3 Jets . . . . .	32

---

4.4	Tagged jets . . . . .	33
4.5	Missing transverse energy . . . . .	34
<b>5</b>	<b>Searches for SUSY events in the single lepton final state</b>	<b>37</b>
5.1	Simulated samples . . . . .	44
5.2	Triggers . . . . .	44
5.3	Background estimation . . . . .	45
5.3.1	Background composition in control regions . . . . .	47
5.3.2	QCD multijet events . . . . .	49
5.3.3	$t\bar{t}$ + jets events . . . . .	50
5.3.4	W+jets events . . . . .	53
5.3.5	Other backgrounds . . . . .	55
<b>6</b>	<b>Systematic uncertainties and validation</b>	<b>57</b>
6.1	$R_{CS}$ stability dependence on $\cancel{E}_T$ measurements . . . . .	57
6.2	QCD multijet events contamination in signal regions . . . . .	62
6.3	Systematic uncertainties . . . . .	64
6.3.1	Background uncertainties . . . . .	64
6.3.2	Signal uncertainties . . . . .	70
6.4	Validation of the background estimation . . . . .	71
<b>7</b>	<b>Results with first data of Run 2</b>	<b>75</b>
7.1	Limits . . . . .	76
7.2	Comparison with other results . . . . .	80
<b>8</b>	<b>Conclusion</b>	<b>83</b>
	<b>Appendices</b>	<b>85</b>
	<b>A Sideband region plots</b>	<b>87</b>
	<b>List of Figures</b>	<b>93</b>
	<b>List of Tables</b>	<b>95</b>
	<b>Bibliography</b>	<b>97</b>

*To my family.*



# Chapter 1

## Standard Model and Supersymmetry

The Standard Model of particle physics (SM) is a very successful theory in describing the behavior and interactions of matter particles. With the announcement of the discovery of a Higgs boson with a mass of 125 GeV both by the CMS and ATLAS collaborations at CERN on July 4th 2012 the last missing piece of the Standard Model was found [1, 2]. In the last decades, its properties have been heavily tested and so far there is no direct evidence of physics beyond the SM at collider experiments. Still, there are some inconsistencies within this powerful framework, the most obvious one being the lack of an explanation for the gravitational force. Additionally, it is known from cosmological observations that only about 5% of the mass-energy content of the universe are made of ordinary matter, while dark matter accounts for roughly 27% [3]. Dark energy makes up the remaining 68% of the mass-energy content. Since the SM does not include a satisfactory dark matter candidate it only describes about 15% of the total mass of the universe.

Technically the SM is a gauge quantum field theory and as such involves loop corrections, which in the case of the scalar Higgs boson mass leads to unnaturally large values in the presence of a cutoff. A fine tuned renormalization has to stabilize the Higgs mass. This fine tuning is considered unnatural, ensuing huge efforts towards a more natural solution to this so called hierarchy problem.

Supersymmetry (SUSY) or more precise supersymmetric extensions of the SM are considered possible solutions to these shortcomings [4–10]. By introducing an additional symmetry to the SM, each fermionic state gets accompanied by a bosonic state, and vice versa. This results in additional particle content, so called superpartners of the SM particles. These superpartners provide a Higgs mass at the experimentally measured

value of 125 GeV without requiring unnatural fine tuning. The lightest supersymmetric particle is considered to be stable in many models and therefore makes a viable dark matter candidate.

## 1.1 Standard Model

The Standard Model of particle physics is one of the most thorough tested theories in physics and is extremely successful in describing phenomena on the microscopic scale. It describes three of the four fundamental interactions, excluding only gravity. In particle physics this is not a big concern as gravitational interactions are predicted to be negligible at microscopic scales. The strong, electromagnetic and weak interaction are well described in the SM. Each interaction is associated with a charge: the strong force with color charge, the electromagnetic force with electric charge and the weak interaction with weak charge. The strong force is responsible for binding elementary particles in nuclei of atoms and the formation of all sorts of hadrons. The electromagnetic force binds electrons to the nucleus and thus explains atoms and molecules as bound states. The weak force describes several decays, most prominently the  $\beta$  decay of neutrons into a proton, electron and antineutrino. In the SM, the weak and the electromagnetic force are unified [11].

The SM matter particles are fermions, while the force carriers are vector bosons. Fermions have half integer spin and obey Fermi-Dirac statistics. Bosons on the other hand have integer spin and therefore act in the framework of Bose-Einstein statistics.

Fermions are first subdivided into quarks and leptons. Quarks are massive particles that are charged under the strong force. They are found in the nucleus of atoms and also carry electric and weak charge, therefore participating in all interactions. Leptons are further subdivided into charged and neutral leptons. Neutral leptons, also called neutrinos, only interact weakly, while charged leptons also participate in the electromagnetic interaction. All leptons are massive, but the exact magnitude of neutrino masses is unknown. The mass generation mechanism for neutrinos is also not known, as their coupling to the Higgs field needs to be very small. Fermions are furthermore grouped into three generations of increasing mass, reflecting the fact that a pattern of particles with similar properties is found.

Bosons are divided into spin 1, so called vector bosons, and spin 0, or scalar bosons. To date, only one spin 0 boson is known: the Higgs boson, which gives mass to the other fundamental particles. The vector bosons include the photon, associated with the electromagnetic force, the W and Z bosons which are responsible for the weak



interaction, and the 8 gluons (the dimension of the adjoint representation of the gauge group  $SU(3)$  of the strong interaction) which mediate the strong force. Out of these, only W and Z bosons carry mass, which explains the short range of the weak interaction. The hypothetical graviton is a massless spin 2 boson.

An overview of all particles contained in the SM is given in Fig. 1.1. Atoms and other long-lived bound states are made of first generation fermions (up and down quarks, electrons). Second and third generation fermions (marked as exotic matter) are found in cosmic rays and can be produced in high energy particle collisions. Antiparticles double the number of SM fermions.

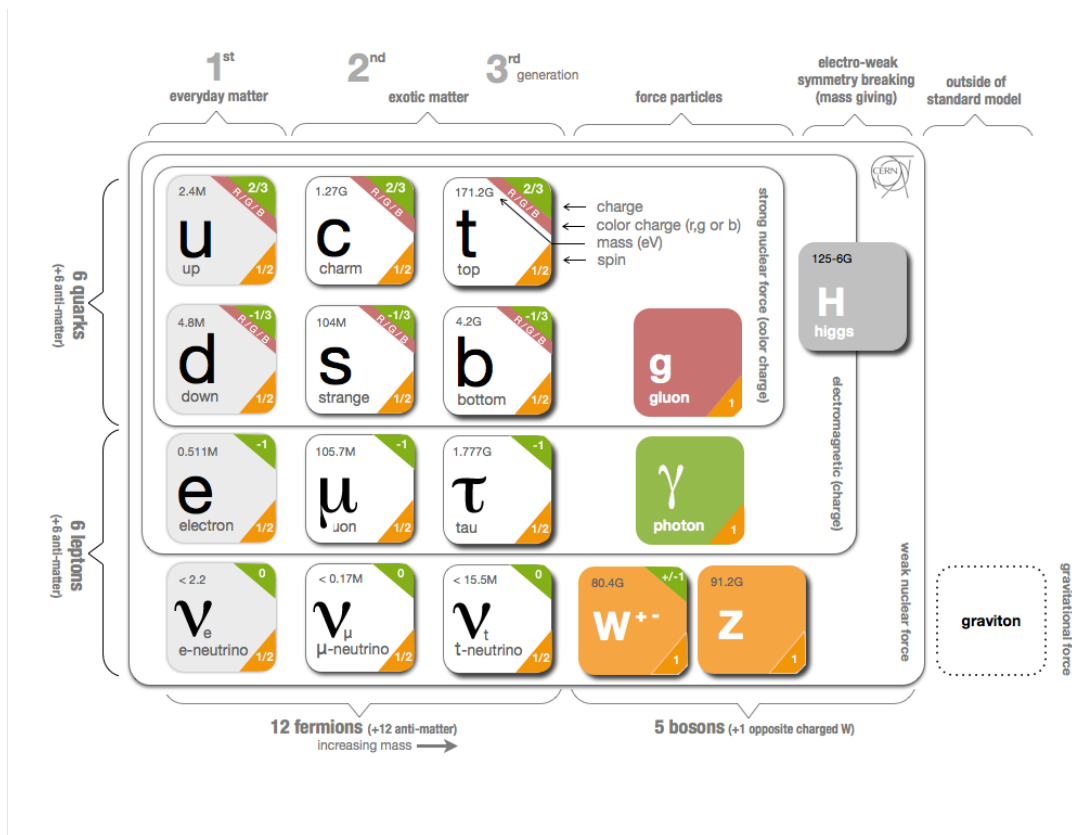


FIGURE 1.1: Overview of the particles contained in the framework of the SM [12]. Fermions are divided into 3 generations with similar properties. Quarks participate in all 3 interactions, while charged leptons interact via the electroweak forces. Neutrinos only interact through the weak force. Of the vector bosons, only W and Z bosons are massive, while the photon and the 8 gluons are massless. The Higgs boson is the only scalar particle of the theory. Particles acquire mass due to the coupling to the Higgs field.

A short introduction to the mathematical principles of the SM is given in the following paragraphs. More examples and exhaustive descriptions as well as calculations can be found in [13, 14].

As a gauge field theory the SM is built on the foundation of quantum physics together with special relativity. A classical system with a potential  $V$  is described by a Lagrange function of the coordinates  $q$  and their derivatives  $\dot{q}$

$$L(q, \dot{q}) = \sum_i \frac{m_i}{2} \dot{q}_i^2 - V(q) \quad . \quad (1.1)$$

The action  $\mathcal{S}$  is given by

$$\mathcal{S} = \int dt L(q, \dot{q}) \quad . \quad (1.2)$$

Using the minimal action principle  $\delta\mathcal{S} = 0$  one obtains the Euler-Lagrange equation

$$\frac{\partial L}{\partial q_i} - \frac{\partial}{\partial t} \frac{\partial L}{\partial \dot{q}_i} = 0 \quad , \quad (1.3)$$

which gives the equations of motion. In case of a field theory with fields  $\phi$  one rather uses the Lagrange density  $\mathcal{L}$  where

$$L = \int d^3x \mathcal{L}(\phi, \partial_\mu \phi) \quad , \quad (1.4)$$

$$\mathcal{S} = \int d^4x \mathcal{L}(\phi, \partial_\mu \phi) \quad \text{and} \quad (1.5)$$

$$\frac{\partial \mathcal{L}}{\partial \phi_i} - \partial_\mu \frac{\partial \mathcal{L}}{\partial (\partial_\mu \phi_i)} = 0 \quad . \quad (1.6)$$

### 1.1.1 The electromagnetic interaction

For a free Dirac fermion one uses a Lagrangian density

$$\mathcal{L}_D = \bar{\psi}(i\gamma^\mu \partial_\mu - m)\psi \quad (1.7)$$

with  $\psi$  being the Dirac spinor in the chiral basis

$$\psi = \begin{pmatrix} \psi_L \\ \psi_R \end{pmatrix} \quad . \quad (1.8)$$

Using the Euler-Lagrange equation one gets

$$(i\gamma^\mu \partial_\mu - m)\psi = 0 \quad (1.9)$$

which is exactly the Dirac equation. One can now couple the fermion to an electromagnetic field  $A_\mu$  and use local gauge invariance  $U(1)$  to obtain the Dirac equation

$$(i\gamma^\mu D_\mu - m)\psi = 0 \quad (1.10)$$

where  $D_\mu$  reflects the covariant derivative which is obtained by requiring local gauge invariance

$$D_\mu = \partial_\mu + iqA_\mu \quad . \quad (1.11)$$

The Lagrangian density then takes the form

$$\mathcal{L} = \bar{\psi}(i\gamma^\mu D_\mu - m)\psi - \frac{1}{4}F_{\mu\nu}F^{\mu\nu} - J^\mu A_\mu \quad (1.12)$$

with the field strength tensor  $F_{\mu\nu}$  from the electromagnetic field and external currents  $J^\mu$ . By applying the Euler-Lagrange equation to the Lagrangian density of the electromagnetic field one obtains the covariant form of the Maxwell equations.

### 1.1.2 The weak interaction

In the low energy limit one can define effective Lagrangians to describe certain weak phenomena such as  $\beta$  decay, muon decay and neutrino scattering. A more elaborate list is given in [14]. The weak force can then be described as extended two vector current interaction, first introduced by Fermi to explain the  $\beta$  decay [15]. As an example, the Lagrangian density of the muon decay can be written as

$$\mathcal{L}_\ell = -2\sqrt{2}G_F g_{\mu\nu} j^\mu j^{\nu\dagger} \quad \text{with} \quad (1.13)$$

$$j^\mu = \sum_\ell \bar{\Psi}_\ell \gamma^\mu \frac{1}{2}(1 - \gamma^5)\nu_\ell \quad (1.14)$$

where  $\ell$  stands for electrons, muons and tau leptons, and  $G_F$  is the Fermi constant.  $\gamma^5$  is associated with chirality and defined as  $\gamma^5 = i\gamma^0\gamma^1\gamma^2\gamma^3$ .

The weak interaction is maximally parity violating, which manifests itself in the non-existence of right handed neutrinos. Only left handed fermions participate in the weak interaction.

### 1.1.3 Electroweak unification and symmetry breaking

The weak and the electromagnetic interaction can be unified in the  $SU(2)_L \times U(1)_Y$  group. Again, one requires local gauge invariance under local  $U(1)$  and  $SU(2)$  transformation. Therefore, the Lagrangian density for the field  $\Phi$

$$\mathcal{L}_\phi = (\partial_\mu \Phi^\dagger) \partial^\mu \Phi - V(\Phi^\dagger \Phi) \quad \text{with} \quad (1.15)$$

$$\Phi = \begin{pmatrix} \Phi_A \\ \Phi_B \end{pmatrix} \quad \text{and} \quad (1.16)$$

$$\Phi_A = \frac{1}{\sqrt{2}}(\phi_1 + i\phi_2) \quad (1.17)$$

has to be modified with a covariant derivative fulfilling the invariance requirements.  $\Phi_B$  is defined likewise. One arrives at

$$D_\mu = \partial_\mu + i\frac{g_1}{2}B_\mu + i\frac{g_2}{2}\mathbf{W}_\mu \quad (1.18)$$

where  $B_\mu$  is a scalar gauge field and  $\mathbf{W}_\mu$  a vector gauge field.  $g_1$  and  $g_2$  are coupling constants of the theory, the factors of 2 are convention. The Lagrangian density then reads

$$\mathcal{L}_\phi = (D_\mu\Phi)^\dagger D^\mu\Phi - V(\Phi^\dagger\Phi) \quad (1.19)$$

The dynamic part of the Lagrangian density is built using field strength tensors. One now uses a potential of the form

$$V(\Phi^\dagger\Phi) = \frac{m^2}{2\phi_0^2}(\Phi^\dagger\Phi - \phi_0^2)^2 \quad (1.20)$$

which, with real fields, reads as

$$V(\Phi^\dagger\Phi) = \frac{m^2}{2\phi_0^2}(\phi_1^2 + \phi_2^2 + \phi_3^2 + \phi_4^2 - \phi_0^2)^2 \quad (1.21)$$

Using the gauge freedom one can set  $\Phi_A$  to zero and set  $\Phi_B$  as real. The ground state is then

$$\Phi = \begin{pmatrix} 0 \\ \phi_0 \end{pmatrix} \quad (1.22)$$

while general states are of the form

$$\Phi = \begin{pmatrix} 0 \\ \phi_0 + h(x)/\sqrt{2} \end{pmatrix} \quad (1.23)$$

with a real field  $h(x)$ . Therefore, the  $SU(2)$  symmetry is broken, while the  $U(1)$  symmetry, which will be associated with the electromagnetic force, remains intact [16, 17]. If this is inserted into Eq. 1.15 one arrives at a Lagrangian density which contains a free massive neutral scalar boson field, one free neutral massive vector boson field and two massive charged vector bosons interacting with the electromagnetic field. The vector fields are associated with the W and Z bosons, the scalar field with the Higgs boson.

Leptons and quarks are coupled to the gauge bosons. To acquire mass, a coupling to the Higgs field is required as well. This Higgs term of the Lagrangian density for the first lepton generation reads as

$$\mathcal{L}_{Higgs}^e = -c_e \left[ (L^\dagger\Phi)e_R + e_R^\dagger(\Phi^\dagger L) \right] \quad (1.24)$$

where  $L$  is the left handed doublet which participates in the weak interaction. Using the symmetry breaking, one can identify the mass term as

$$\mathcal{L}_{mass}^e = -c_e \phi_0 \left( e_L^\dagger e_R + e_R^\dagger e_L \right) - c_e \frac{h}{\sqrt{2}} \left( e_L^\dagger e_R + e_R^\dagger e_L \right) \quad . \quad (1.25)$$

There is no right handed neutrino  $\nu_R$  (maximal parity violation of the weak force).  $c_e$  is the coupling of the electron to the Higgs field. Quarks couple to the Higgs field similarly, however, the coupling constant is replaced by the Cabibbo-Kobayashi-Maskawa (CKM) matrix.

It was shown that by implying local gauge invariance and spontaneous symmetry breaking the electromagnetic and the weak interaction can be unified. Both the arising  $W^\pm$  and  $Z$  vector bosons as well as the fermions of the SM acquire mass from coupling to the Higgs field.

#### 1.1.4 The strong interaction

Interactions of quarks are described by quantum chromodynamics (QCD). The Lagrangian density of QCD is invariant under local  $SU(3)$  transformations, the so called color degrees of freedom. This additional quantum number is considered as another type of charge, mediated by gluons. Again, a covariant derivative has to be defined

$$D_\mu = \partial_\mu + ig\mathbf{G}_\mu \quad (1.26)$$

with  $g$  the strong coupling constant and the gauge field

$$\mathbf{G}_\mu = \sum_{a=1}^8 G_\mu^a F_a \quad (1.27)$$

with  $F_a$  the generators of the transformation, fulfilling the Lie algebra

$$[F_a, F_b] = if_{abc} F_c \quad . \quad (1.28)$$

Due to the non-vanishing commutator of the generators, the strong interaction is a non abelian gauge theory. The dynamic part of the Lagrangian density associated with the quarks reads as

$$\mathcal{L}_{quark} = \sum_{f=1}^6 (\bar{q}_f i\gamma^\mu D_\mu q_f - m_f \bar{q}_f q_f) \quad . \quad (1.29)$$

One can again define field strength tensors which, in this case, represent the gluon field

$$\mathcal{L}_{gluon} = -\frac{1}{4} \sum_{a=1}^8 G_{\mu\nu}^a G^{a\ \mu\nu} . \quad (1.30)$$

Although gluons are considered as massless, the strong interaction is short ranged. All particles found in nature are color neutral, therefore quarks have to come at least in pairs. This is known as quark confinement. If quarks are separated, new bound states (hadrons) are formed immediately, a process which is called hadronization. In contrary, at short ranges the strength of the interaction between quarks gets smaller, which is known as asymptotic freedom and allows for perturbative calculations [18, 19].

### 1.1.5 Shortcomings of the Standard Model

Although being very successful in describing the nature of matter, there are unsolved problems and phenomena not explained by the SM. These missing pieces include:

- Missing incorporation of General Relativity / gravity  
General Relativity is a classical theory and can not be unified with quantum theories from the SM. So far, quantum gauge theories of gravity are not renormalizable [20].
- Unification of coupling constants at the GUT scale  
It is expected that the coupling constants of the three fundamental forces (strong, electromagnetic, weak) are unified at the Grand Unified Theory (GUT) scale, which is not the case in the SM. At the even higher Planck scale, also gravity is unified with the other fundamental forces.
- No cold dark matter candidate  
Neutrinos fulfill the properties needed for a dark matter particle as they are only weakly interacting. However, due to the small mass, neutrinos are always relativistic and therefore *hot* and not a viable *cold* dark matter candidate [21].
- Hierarchy/naturalness problem  
The Higgs mass is sensitive to corrections from new physics at higher scales due to loop processes. An unnaturally fine-tuned cutoff is needed to fix the mass at the measured value if there are no other cancellations.
- Neutrino masses  
Within the SM neutrinos are massless. The observed oscillations of neutrinos between the three generations can only be explained if neutrinos are massive [22].

Only upper bounds could be measured so far. However, the already low upper bounds on the neutrino masses require a very small coupling to the Higgs field. The see-saw mechanism, involving heavy right handed neutrinos, provides a solution to this problem [23].

SUSY is one of the most prominent theories for extending the SM as it can solve a few of these problems at a time. Additional particles that resolve the hierarchy problems through cancellations are introduced by SUSY. If R-parity is conserved, the lightest sparticle will be stable and if it has a mass of  $O(100)$  GeV it provides a good dark matter candidate [24]. Gauge coupling constants of the fundamental forces are dependent on the energy scale. The evolution of the renormalization group of inverse SM gauge couplings does not lead to a unified value. However, the particle content of the minimal supersymmetric extensions of the SM ensures that gauge couplings can unify at a high scale, shown in Fig. 1.2. Unification of the three forces at the GUT scale is therefore achieved in many models.

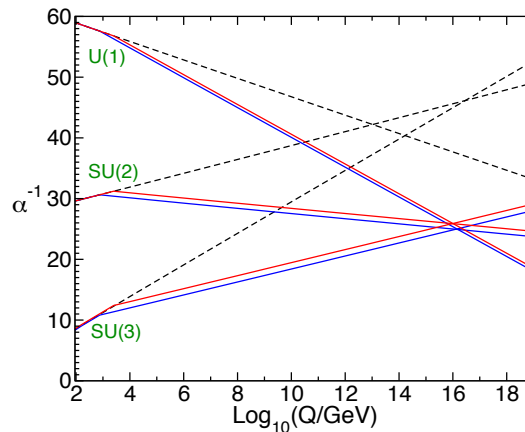


FIGURE 1.2: Evolution of the inverse gauge couplings in the SM (dashed lines) and the supersymmetric extensions of the SM (solid lines) [25].

## 1.2 Supersymmetry

This short introduction will to a large extent follow the very nice and pedagogical version found in [25]. In SUSY, an additional symmetry is introduced to the SM which relates fermionic states to bosonic states with an operator  $Q$ .

$$\begin{aligned}
 Q |\text{fermion}\rangle &= |\text{boson}\rangle \\
 Q |\text{boson}\rangle &= |\text{fermion}\rangle
 \end{aligned}
 \tag{1.31}$$

$Q$  and its Hermitian conjugate are fermionic operators, carrying spin  $1/2$ . Therefore,  $Q$  changes the spin of states it is applied to by  $1/2$ , turning spin  $1/2$  fermions into spin  $0$  scalars and spin  $1$  bosons into spin  $1/2$  fermions. The symmetry transformation of the scalar Higgs boson results in a spin  $1/2$  fermion as well. SM fermions and their corresponding scalar particles, also called sparticles, can be arranged in a chiral supermultiplet, shown in Tab. 1.1. The Higgs sector is increased to five Higgs bosons contained in two chiral supermultiplets in order to avoid gauge anomalies.

Name	notation	spin 0	spin 1/2
squarks, quarks (3 generations)	$Q$	$(\tilde{u}_L \tilde{d}_L)$	$(u_L d_L)$
	$\bar{u}$	$\tilde{u}_R^*$	$u_R^\dagger$
	$\bar{d}$	$\tilde{d}_R^*$	$d_R^\dagger$
sleptons, leptons (3 generations)	$L$	$(\tilde{\nu} \tilde{\ell}_L)$	$(\nu \ell_L)$
	$\bar{\ell}$	$\tilde{\ell}_R^*$	$\ell_R^\dagger$
Higgs, higgsinos	$H_u$	$(H_u^+ H_u^0)$	$(\tilde{H}_u^+ \tilde{H}_u^0)$
	$H_d$	$(H_d^0 H_d^-)$	$(\tilde{H}_d^0 \tilde{H}_d^-)$

TABLE 1.1: The chiral supermultiplets. Spin-0 fields are complex scalars, half integer spin fields are left-handed two-component Weyl fermions.

Likewise, SM gauge bosons form gauge supermultiplets with their fermionic superpartners, shown in Tab. 1.2.

Name	spin 1/2	spin 1
gluino, gluon	$\tilde{g}$	$g$
winos, W boson	$\tilde{W}^\pm, \tilde{W}^0$	$W^\pm, W^0$
zinos, B boson	$\tilde{B}^0$	$B^0$

TABLE 1.2: The gauge supermultiplets.

All superpartners are new particles, attempts to combine SM particles into supermultiplets have failed. Although the superpartners have the same masses as their SM partners, none of these particles has been discovered yet. This leads to the conclusion that supersymmetry has to be a broken symmetry.

### 1.2.1 Minimal Supersymmetric Standard Model

The Minimal Supersymmetric Standard Model (MSSM) is the minimal extension of the SM, as it is the model with the least number of additional particles and degrees of freedom. The MSSM introduces only one additional symmetry, hence it is also called  $N = 1$  SUSY.



The interaction eigenstates are shown in Tab. 1.1 and Tab. 1.2. However, these states mix to different mass eigenstates shown in Tab. 1.3.

Name	Spin	$P_R$	Gauge eigenstate	Mass eigenstate
Higgs bosons	0	+1	$H_u^0 H_d^0 H_u^+ H_d^-$	$h^0 H^0 A^0 H^\pm$
squarks	0	-1	$\tilde{u}_L \tilde{u}_R \tilde{d}_L \tilde{d}_R$	(same)
			$\tilde{s}_L \tilde{s}_R \tilde{c}_L \tilde{c}_R$	(same)
			$\tilde{t}_L \tilde{t}_R \tilde{b}_L \tilde{b}_R$	$\tilde{t}_1 \tilde{t}_2 \tilde{b}_1 \tilde{b}_2$
sleptons	0	-1	$\tilde{e}_L \tilde{e}_R \tilde{\nu}_e$	(same)
			$\tilde{\mu}_L \tilde{\mu}_R \tilde{\nu}_\mu$	(same)
			$\tilde{\tau}_L \tilde{\tau}_R \tilde{\nu}_\tau$	$\tilde{\tau}_1 \tilde{\tau}_2 \tilde{\nu}_\tau$
neutralinos	1/2	-1	$\tilde{B}^0 \tilde{W}^0 \tilde{H}_u^0 \tilde{H}_d^0$	$\tilde{\chi}_1^0 \tilde{\chi}_2^0 \tilde{\chi}_3^0 \tilde{\chi}_4^0$
charginos	1/2	-1	$\tilde{W}^\pm \tilde{H}_u^\pm \tilde{H}_d^\pm$	$\tilde{\chi}_1^\pm \tilde{\chi}_2^\pm$
gluino	1/2	-1	$\tilde{g}$	(same)
goldstino	1/2	-1	$\tilde{G}$	(same)
gravitino	3/2	-1		(same)

TABLE 1.3: The additional particle content of the MSSM with gravity incorporated.

The neutral higgsinos, winos and binos mix to four so called neutralinos, while the charged ones mix to two charginos. The goldstino arises from global supersymmetry breaking, while incorporation of gravity requires a local symmetry. This local supersymmetry is called *supergravity*. The hypothetical spin 2 graviton gets a spin 3/2 superpartner, the gravitino. With unbroken SUSY the gravitino is massless (like the graviton), but due to the symmetry breaking it acquires mass by absorbing the goldstino, which is a similar process to the electroweak symmetry breaking and therefore called *super-Higgs* mechanism.

Although the MSSM is the minimal extension of the SM, it still introduces 105 new parameters in addition to the 19 parameters of the SM. Several models were built which further constrain some of these parameters.

In the unconstrained MSSM (uMSSM) no further constraints or simplifications are applied, leaving the 105 parameters to be determined. This results in a technical problem as scans over these parameters are extremely computationally expensive. The phenomenological MSSM (pMSSM) reduces the number of free parameters to 19 by constraining SUSY to not introduce new CP violating sources, requiring no flavor changing neutral currents and first and second generation universality [26]. A further minimized model is the constrained MSSM (cMSSM) with only five free parameters, which uses minimal supergravity as symmetry breaking mechanism as described above, and is therefore often referred to as mSUGRA.

### 1.2.2 Solution to the hierarchy problem

As a scalar particle, the Higgs boson is sensitive to loop corrections from other particles, as well as to potential corrections from new physics. For a coupling of the Higgs boson to a Dirac fermion one obtains the contribution to the Higgs mass of

$$\Delta m_H^2 = \frac{|\lambda_f|^2}{8\pi^2} [-\Lambda_{UV}^2 + 3m_f^2 \ln(\Lambda_{UV}/m_f) + \dots] \quad (1.32)$$

with a ultraviolet momentum cutoff  $\Lambda_{UV}$  to regulate the loop integral. New physics at or close to the Planck scale therefore induce large corrections to the Higgs mass  $\Delta m_H^2$ , about 32 orders of magnitude larger than the physical Higgs mass. A Higgs boson with a measured mass of roughly 125 GeV therefore requires an unnatural fine tuning

$$m_H^2|_{\text{physical}} = m_H^2|_{\text{bare}} - \Delta m_H^2 \quad . \quad (1.33)$$

However, there is an opposite sign in the correction term for fermion and boson contributions, with the scalar boson corrections reading as

$$\Delta m_H^2 = \frac{\lambda_S}{16\pi^2} [\Lambda_{UV}^2 - 2m_S^2 \ln(\Lambda_{UV}/m_S) + \dots] \quad . \quad (1.34)$$

This leads to a systematic cancellation of the correction terms. Diagrams of fermion and boson loop corrections to the Higgs boson are shown in Fig. 1.3. With an unbroken supersymmetry the quadratic sensitivity to high mass scales vanishes. Due to the fact that supersymmetry is broken, the cancellation is not exactly fulfilled. Again, quadratic divergences enter the radiative corrections

$$\Delta m_H^2 = \frac{1}{8\pi^2} [(\lambda_S - |\lambda_f|^2)\Lambda_{UV}^2 + \dots] \quad . \quad (1.35)$$

Therefore, the symmetry breaking mechanism needs to be *soft*, which means that the effective Lagrangian density can be written as

$$\mathcal{L} = \mathcal{L}_{\text{SUSY}} + \mathcal{L}_{\text{soft}} \quad . \quad (1.36)$$

$\mathcal{L}_{\text{SUSY}}$  contains gauge and Yukawa interactions while  $\mathcal{L}_{\text{soft}}$  only violates the symmetry. Now the corrections to the Higgs mass only contain logarithmic divergences and read as

$$\Delta m_H^2 = -m_{\text{soft}}^2 \left[ \frac{\lambda}{16\pi^2} \ln(\Lambda_{UV}/m_{\text{soft}}) + \dots \right] \quad . \quad (1.37)$$

With the natural requirement

$$|\Delta m_H^2| < m_H^2|_{\text{physical}} \quad (1.38)$$

one can estimate  $m_{\text{soft}}$  in the TeV range. This indicates that SUSY particles should be accessible at the LHC.

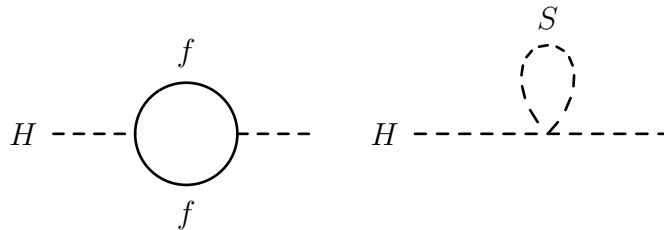


FIGURE 1.3: Diagrams of corrections to the Higgs mass from fermions (left) and scalars (right).

### 1.2.3 Dark matter candidate

Besides the elegant way of solving the hierarchy problem, SUSY also provides a dark matter candidate. This candidate arises from the conservation of an additional symmetry, the R-parity or matter parity. Baryon and lepton number conservation are no intrinsic properties of the MSSM, but violation leads to rapid proton decay. Since there is no experimental observation of proton decays, imposing this new symmetry is a sensible choice. R-parity is a multiplicatively quantum number defined as

$$P_R = (-1)^{3(B-L)+2s} \quad (1.39)$$

where  $B$  is the baryon number,  $L$  the lepton number and  $s$  the spin [24]. All SM particles have even R-parity ( $P_R = +1$ ), while SUSY particles have odd R-parity ( $P_R = -1$ ). In general, vertices contain an even number of R-parity odd particles. This results in at least pair production of SUSY particles and a stable lightest supersymmetric particle (LSP). The LSP is then a viable dark matter candidate.

### 1.2.4 Simplified models

The wide spectrum of different SUSY models with a huge variety of free parameter makes it challenging to test large areas of phase space. Instead of testing experimental results against full models, simplified topologies are constructed, involving only part of the parameter space. This is done by considering only a few particles and interactions,

while other particles do not play a role in specific limits or are integrated out [27]. At the same time, simplifications of branching ratios and decay widths are applied. Setting the branching ratios to 100% further reduces the parameters, for mixed decays a linear combination of such models can be used. The remaining parameters such as particle masses are directly observable in collider experiments in typical experimental signatures. These typical experimental signatures can be produced in several ways even within the MSSM. Results and limits on production cross sections and branching ratios can then be extracted from the simplified models and be used to constrain more specific models [28]. Simplified models are widely used in searches for supersymmetry.

An example of a simplified model is the direct threebody decay of a gluino into two light quarks and the lightest neutralino

$$\tilde{g} \rightarrow q\bar{q}' \tilde{\chi}_1^0$$

which dominates in SUSY models with decoupled squarks or squarks with soft masses at the TeV scale, but larger than the gluino mass. This is the case in split-supersymmetry. The minimal set of parameters in this example includes the masses of the gluino and the neutralino,  $m_{\tilde{g}}$  and  $m_{\tilde{\chi}_1^0}$ , and the production cross section of the gluino  $\sigma(pp \rightarrow \tilde{g} \tilde{g} + X)$ . In gauge mediated symmetry breaking (GMSB) SUSY models the direct decay is not dominating, leading to decays like

$$\begin{aligned} \tilde{g} \rightarrow q\bar{q}' \tilde{\chi}_1^\pm &\rightarrow q\bar{q}'(W^\pm \tilde{\chi}_1^0) \quad \text{or} \\ \tilde{g} \rightarrow q\bar{q}' \tilde{\chi}_2^0 &\rightarrow q\bar{q}'(Z^0 \tilde{\chi}_1^0) \quad . \end{aligned}$$

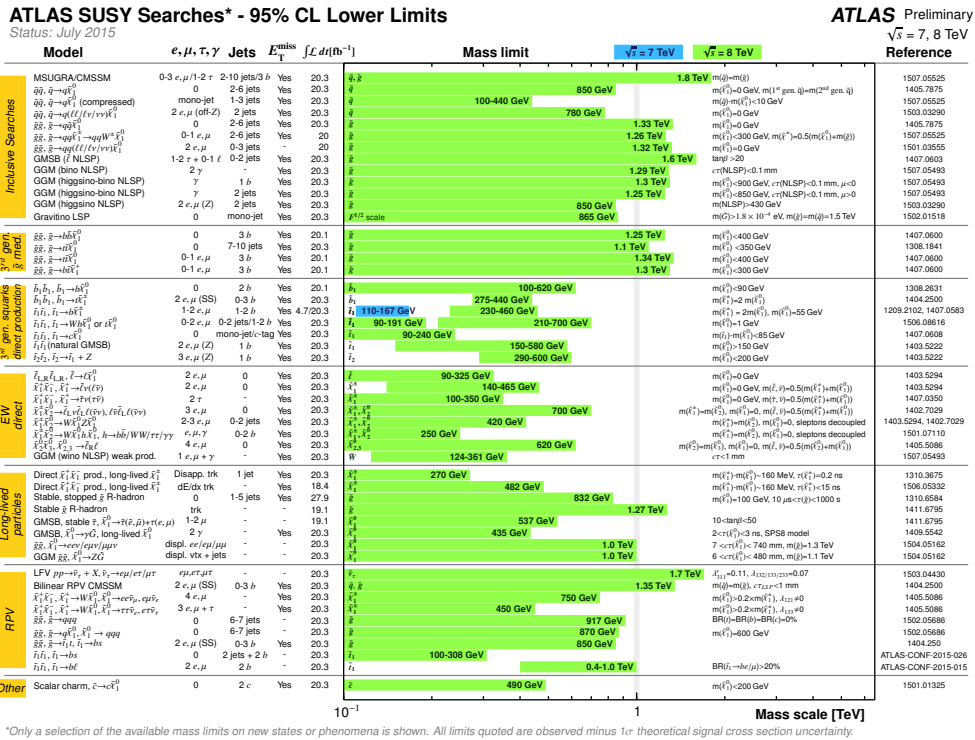
In this case, the parameters also include the mass of the intermediate particle, either a chargino  $\tilde{\chi}_1^\pm$  or a heavier neutralino  $\tilde{\chi}_2^0$ . To reduce the four-dimensional space, mass slices at fixed values of  $m_{\tilde{\chi}_1^\pm}$  or  $m_{\tilde{\chi}_2^0}$  are used.

$$m_{\tilde{\chi}_1^\pm} = m_{\tilde{\chi}_1^0} + r(m_{\tilde{g}} - m_{\tilde{\chi}_1^0}) \quad (1.40)$$

The choice of  $r$  alters the kinematics of the decay. Usually a few values of  $r$  are used to cover a variety of kinematics. The branching ratio to chargino or neutralino is usually set to 100% to keep the number of parameters low.

### 1.2.5 SUSY after LHC Run 1

The 2011 and 2012 runs of the LHC (also called Run 1) have been very successful, and two large datasets at a center of mass energy of 7 and 8 TeV have been accumulated and



\*Only a selection of the available mass limits on new states or phenomena is shown. All limits quoted are observed minus 1 $\sigma$  theoretical signal cross section uncertainty.

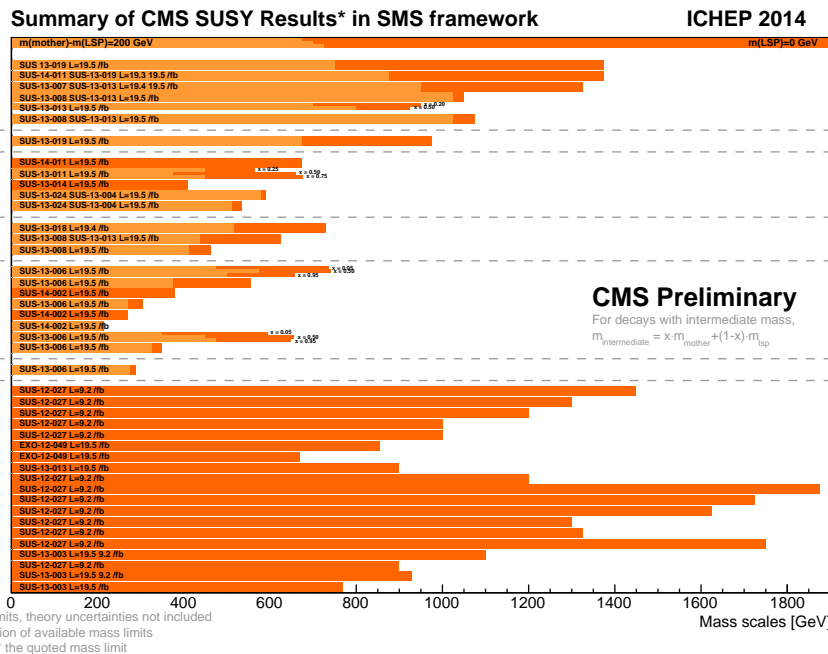


FIGURE 1.4: Exclusion limits on sparticle masses from searches for SUSY from the 7 and 8 TeV runs by the ATLAS and CMS collaborations [29, 30].

analyzed. The abundance of significant excesses in the vast amount of analyses carried out by the collaborations of the two multi-purpose experiments, ATLAS and CMS, covering several different topologies and large regions of phase space have left part of the physics community disappointed. Strong limits on SUSY particle masses up to 1.8 TeV for several models, shown in Fig. 1.4, imply tight constraints. If superpartners preserve the naturalness of the SM, their abundance at the TeV scale already raises doubts whether SUSY exists in the presumed forms [31]. In the case of the cMSSM there are already claims of exclusions of the model [32].

### 1.2.6 Expectations for LHC Run 2

Although significant excesses were missing in Run 1, a few small deviations from SM expectations were observed [33, 34]. Therefore, testing these models for clarifications was one of the first targets for Run 2.

The cross section of gluino and squark productions are drastically increased, implying enhanced sensitivity already with small datasets. Diagrams of gluino pair production processes in hadron colliders like LHC are shown in Fig. 1.5. A comparison of gluino cross sections between center of mass energies of 7, 8 and 13 TeV is shown in Fig. 1.6. For gluino masses of 1.5 TeV, the cross section increases from 0.4 fb to 14 fb [35, 36].

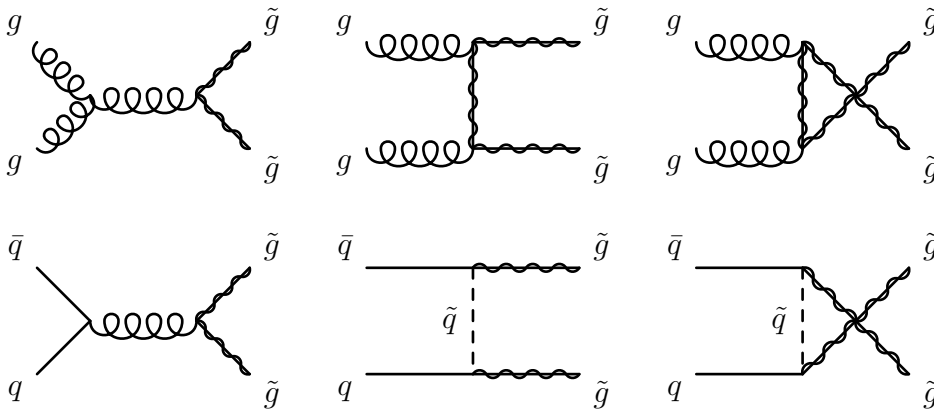


FIGURE 1.5: Diagrams of gluino pair production at hadron colliders, via gluon fusion (upper row) and quark-antiquark annihilation processes (lower row). The diagrams show the s-channel (left), t-channel (center) and u-channel (right).

At the same time, cross sections of SM processes are increased as well. The evolution of production cross sections over the center of mass energy is shown in Fig. 1.7.

Confirming existing mass limits and performing improved searches in models which already are under tight constraints should not be the only strategy of analyses in Run 2 of the LHC. Signals without high amount of missing transverse energy are not so heavily

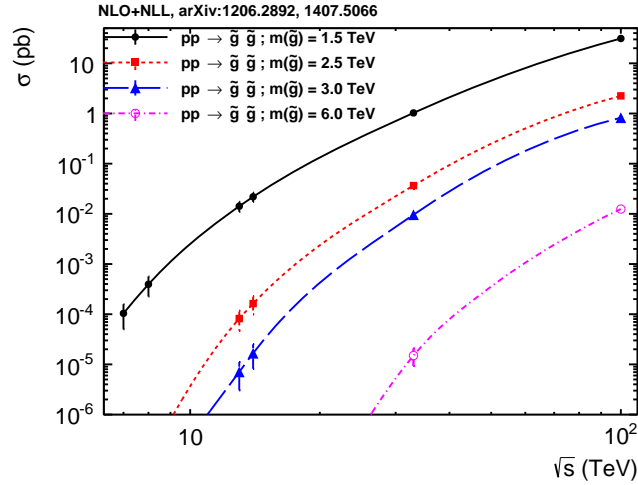


FIGURE 1.6: Cross sections of gluino pair production for different mass points, as functions of center of mass energy [35]. An increase of more than factor of 10 between 8 TeV and 13 TeV is expected, enhancing the reach of searches already for small amounts of accumulated proton proton collision data.

constrained yet, so searches in more compressed SUSY spectra, for R parity violating models (RPV) and stealth SUSY are well motivated [38]. Searches for non-minimal models are also under less pressure from null results at the LHC. Natural SUSY (light third generation and heavy first and second generation sparticles), supersoft SUSY (same mass scale for all squarks, but decoupled gluino), colorless SUSY (top partners at low energies QCD neutral), focus point SUSY (same mass scale squarks, but elimination of the radiative sensitivity of the weak scale on the soft masses) and unnatural SUSY (allowing for a moderate amount of fine tuning, with higher squark masses) are models beyond the probed phase space and therefore are much less constrained from LHC limits so far. A short introduction to these models is given in [38].

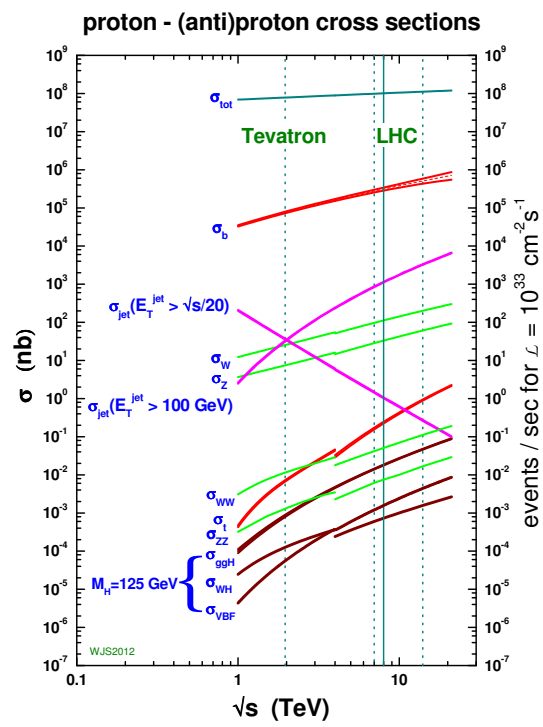


FIGURE 1.7: Cross sections of SM processes at the LHC [37].



## Chapter 2

# The Large Hadron Collider at CERN

The Large Hadron Collider (LHC) is located at the European Organization for Nuclear Research (CERN) at the French-Swiss border near Geneva. With a circumference of 27 km it is the largest particle accelerator ever built. Currently, protons are accelerated in bunches and collided with a center of mass energy  $\sqrt{s} = 13$  TeV, which makes it the most powerful particle collider to date. It is also claimed to be the largest single machine in the world.

### 2.1 The accelerator complex

The LHC is the final accelerator and storage ring for protons after a few stages of pre-acceleration. The LHC accelerator complex is shown in Fig. 2.1. Hydrogen is ionized in order to obtain protons, which are then accelerated to 50 MeV by a linear accelerator (Linac2). Next, the proton synchrotron booster (PS Booster) and proton synchrotron (PS) accelerate the protons further to energies of 1.4 GeV and 25 GeV, respectively. The proton synchrotron was commissioned in 1960 and therefore is in use over 50 years already. The final step of pre-acceleration is performed in the super proton synchrotron (SPS), with an extraction energy of 450 GeV. The SPS was formerly used as a collider as well, and with the detection of W and Z bosons in the UA1 and UA2 experiments it laid groundwork for further collider experiments [39, 40]. After all proton bunches are filled into the two counter-rotating rings of the LHC, the beams get accelerated to the final energy, which accounts for 6.5 TeV per beam at the moment. Beams are colliding in four intersection points where the detectors of the experiments are located. The two multi-purpose detectors, the CMS (Compact Muon Solenoid) and ATLAS (A Toroidal

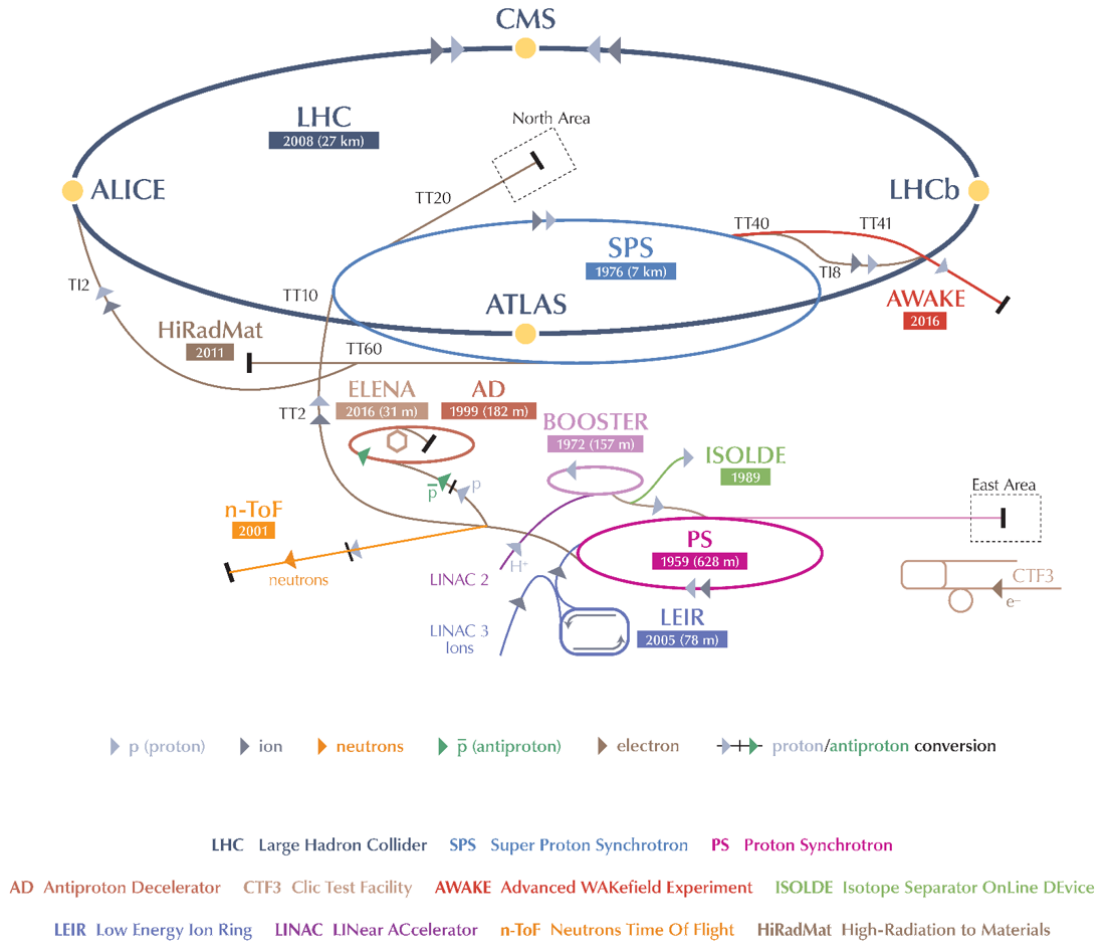


FIGURE 2.1: CERN's accelerator complex [41].

LHC AparatuS), are accompanied by the LHCb (LHC Beauty) and ALICE (A Large Ion Collider Experiment) experiments. The LHCb experiment is designed to probe decays of b and c hadrons, while ALICE is mainly looking for quark gluon plasma in lead ion collisions.

## 2.2 Features and properties

The most important features of the LHC are introduced here with all details available in the design reports [42–44]. Protons are filled in packets, called bunches, with  $1.15 \times 10^{11}$  protons each, which, with a total of 2808 bunches, accounts for about  $3 \times 10^{14}$  protons per beam. The bunch spacing, the time distance between two bunches, is 25 ns, which infers a collision rate of 40 MHz. The beam cross section at the intersection points measures about 0.06 mm. Superconducting dipole magnets used to bend the proton beam to describe a circular track orbit provide a magnetic field of up to 8.3 T. Higher order magnets such as quadrupoles and sextupoles are used for orbital and momentum

focusing. One main parameter of colliding beam experiments is the luminosity, which, when multiplied with the cross section of a specific process, gives the expected event rate of that process

$$\frac{dN}{dt} = \mathcal{L} \cdot \sigma \quad (2.1)$$

where  $\sigma$  is the cross section of a process and  $\mathcal{L}$  the instantaneous luminosity, calculated by

$$\mathcal{L} = \frac{N_b^2 n_b \nu \gamma}{4\pi \epsilon_n \beta^*} F \quad (2.2)$$

with  $N_b$  the number of protons per bunch,  $n_b$  the number of bunches,  $\nu$  the revolution frequency,  $\gamma$  the relativistic gamma (Lorentz) factor,  $\epsilon_n$  the normalized beam emittance,  $\beta^*$  the beta function of the beam at the intersection and  $F$  a correction factor for the angle of the beam crossing. In previous collider experiments like Tevatron and LEP the luminosity was of the order  $\mathcal{L} = 10^{32} \text{ cm}^{-2}\text{s}^{-1}$ . For the LHC, the design luminosity is  $\mathcal{L} = 10^{34} \text{ cm}^{-2}\text{s}^{-1} = 10 \text{ nb s}^{-1}$ . A commonly used parameter is the integrated luminosity, which is a measure for the total number of interactions in a time period, usually of one data taking run

$$L = \int \mathcal{L} dt \quad . \quad (2.3)$$

The integrated luminosity of proton-proton collisions delivered to the CMS experiment in the 7 and 8 TeV runs accounted for 6.1 and 23.3  $\text{fb}^{-1}$ , respectively.



## Chapter 3

# The CMS experiment at the LHC

A brief overview of the CMS experiment, one of the four main experiments at the CERN LHC, is given here. More detailed descriptions can be found in [45–47].

The CMS experiment is located at Point 5 of the LHC, one of the four collision points. The CMS detector is used to identify and measure elementary particles coming from proton-proton collisions at a center of mass energy of  $\sqrt{s} = 13$  TeV. Several sub-systems are needed to accomplish this task: A high magnetic field to bend the tracks of charged particles for momentum measurements is created by a superconducting magnet. Tracks of charged particles are reconstructed using a silicon tracker system. Energy deposits of all particles besides neutrinos and possible new uncharged, weakly interacting particles are measured in the electromagnetic (ECAL) or hadronic (HCAL) calorimeters. Muons are finally measured in the dedicated muon system. A 3D view of the CMS detector is shown in Fig. 3.1 to give an idea of its size and structure. The detector has a length of about 22 m with a diameter of 15 m and a weight of roughly 14000 t.

The coordinate system is defined as follows: The origin is located at the nominal interaction point. The x axis points radially inwards to the center of the LHC, while the y axis points vertically upwards and the z axis points in the beam direction towards the Jura mountains, as seen from point 5. The azimuthal angle  $\phi$  is measured from the x axis in the transverse x-y plane. The polar angle  $\theta$  is measured from the z axis, with the pseudorapidity defined as  $\eta = -\ln \tan(\theta/2)$ . The detector is subdivided into the barrel ( $|\eta| < 1.3$ ), endcap ( $1.3 < |\eta| < 3$ ) and forward region ( $3 < |\eta| < 5$ ). A slice of the cross section of the CMS detector is shown in Fig. 3.2. It shows the onion-like structure, with the tracking system and the calorimeters inside the superconducting magnet. The outermost shell consists of the muon system. Tracks of different particle types are shown as well: A photon passes the tracker system without leaving a track, while its energy is measured in the ECAL. Likewise, neutral hadrons do not leave a trace in the tracker

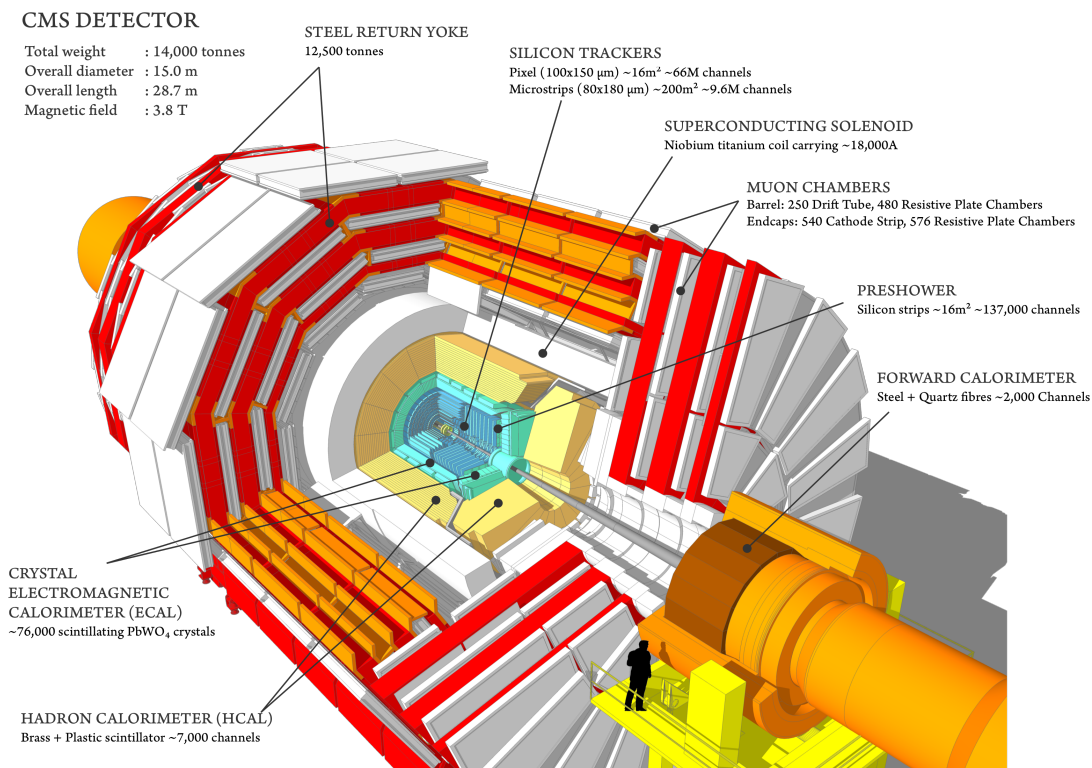


FIGURE 3.1: 3D model with sectional view on the different subdetectors of the CMS detector [48].

and in the ECAL, their energy is measured in the HCAL. Electrons leave a bent track in the tracking system before being stopped in the ECAL. Tracks and energy deposits mainly in the HCAL are used to measure charged hadrons. Muons are first measured in the tracker, before interacting with the dedicated muon system located outside of the magnet.

### 3.1 Superconducting magnet

The superconducting solenoid magnet produces a field of 3.8 T and is crucial for the precise measurements of charged particles. The inner bore of the magnet has a diameter of 6.3 m to accommodate the tracking and calorimeter systems. A nominal current of over 19 kA results in a stored energy of 2.6 GJ. The superconducting coil is operated at 4.5 K, provided by a helium refrigeration plant.

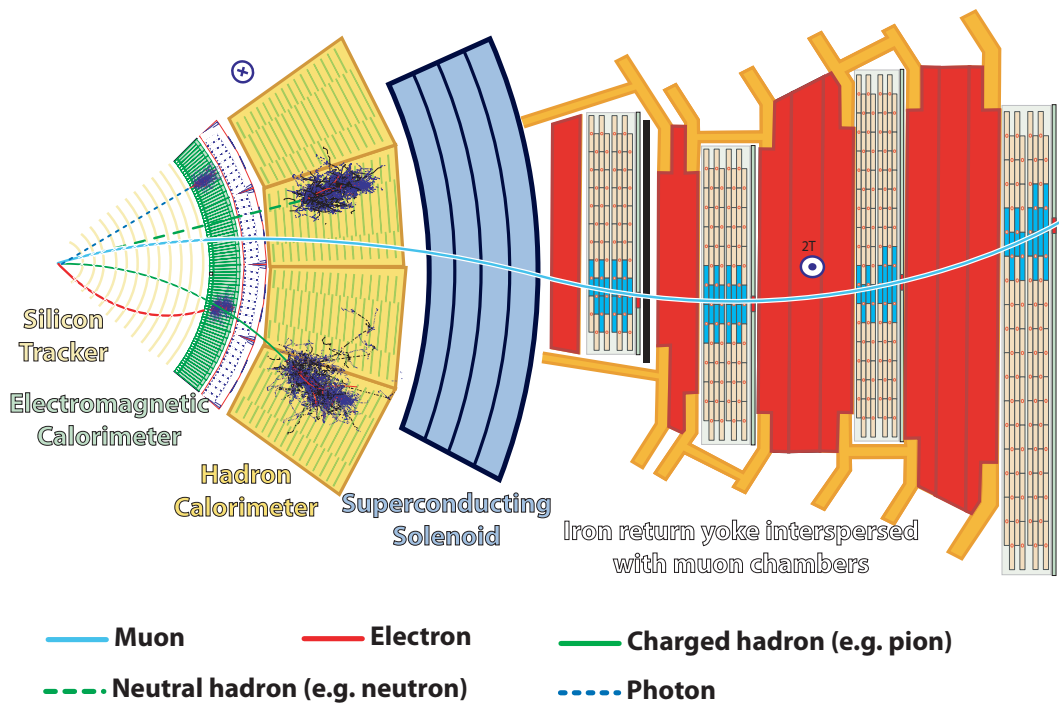


FIGURE 3.2: Cross section of a slice of the CMS detector.

### 3.2 Tracker

The tracker system consists of silicon pixel and strip sensors. It is used to measure the trajectories of charged particles and reconstruct secondary vertices. The material choice of silicon was made due to the requirements of a low amount of material to reduce unwanted interactions, as well as radiation hardness. At full luminosity, about one billion inelastic events per second are expected to take place within the detector, causing severe energy deposits in the tracking system. In the barrel region, the tracker consists of three pixel detector layers with radii between 4.4 cm and 10.2 cm, shown in Fig. 3.3. A silicon strip tracker with 10 layers extends to a radius of 1.1 m. In the forward endcap region, 2 discs of pixel detectors and 3 plus 9 discs of strip detectors complete the tracking system. With a total surface of about 200 m<sup>2</sup> the CMS tracker is the largest silicon detector built to date.

The transverse impact parameter, which is defined as the distance of closest approach to the beam axis and is computed from pixel hits of a track, has a resolution of down to 10  $\mu\text{m}$  for muons with a momentum of 100 GeV. For lower momenta, the resolution is decreased up to 100  $\mu\text{m}$  due to multiple scattering. The momentum resolution of muons is within the percentage regime.

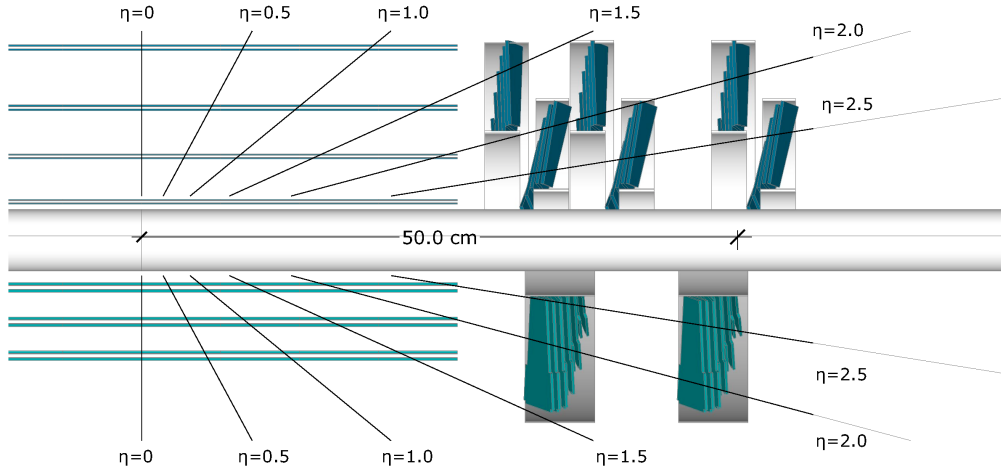


FIGURE 3.3: The CMS pixel detector, with the current structure shown in the lower half of the image. The structure in the upper half shows a design for an upgraded structure.

### 3.3 Electromagnetic calorimeter

The electromagnetic calorimeter (ECAL) is used to measure the energy of photons and electrons. It is made out of 61200 lead tungstate crystals in the barrel region and 7324 crystals in the two endcaps. Photodiodes and phototriodes are used to detect the showers produced in the crystals in the barrel and endcap, respectively. The lead tungstate scintillators allow for a compact calorimeter design, important due to space restrictions within the magnet. Crystals in the barrel region have a length of 230 mm, corresponding to 25.8 radiation lengths, with a cross-section of  $22 \times 22 \text{ mm}^2$  to  $26 \times 26 \text{ mm}^2$  due to the tapered shape. Crystals in the endcap region on the other hand have a length of 220 mm, corresponding to 24.7 radiation lengths, with a cross-section of  $28.6 \times 28.6 \text{ mm}^2$  to  $30 \times 30 \text{ mm}^2$ . In the endcap region a preshower is located in front of the ECAL to identify neutral pions, which otherwise could be misidentified as photons. The energy resolution of the ECAL was found to be

$$\left(\frac{\sigma}{E}\right)^2 = \left(\frac{2.8\%}{\sqrt{E}}\right)^2 + \left(\frac{0.12}{E}\right)^2 + (0.30\%)^2 \quad (3.1)$$

where the first term is caused by stochastic effects, the second term by noise and the third constant term is mainly due to non-uniformities, intercalibration errors and energy leakage from the back of the crystal. For a 120 GeV electron, this results in a resolution of 0.4%.



### 3.4 Hadronic calorimeter

The hadronic calorimeter (HCAL) is a sampling calorimeter, made out of brass absorbers and plastic scintillators. Wavelength shifting cables are used to extract the scintillation light, which is detected using hybrid photodiodes. The HCAL is subdivided into barrel (HB), outer (HO), endcap (HE) and forward (HF) calorimeters. The HB is restricted in size due to the solenoid magnet, which makes it possible that hadrons are not fully stopped. To catch late showering hadrons, the HO, also called tail catcher, is used outside of the magnet. It utilizes the material of the magnet as absorber, while the scintillators are attached to the iron return yoke of the magnet. With the HO included, the HCAL has a thickness of 10-15 interaction lengths, dependent on the  $\eta$  region. The HF is exposed to highest particle fluxes, making best possible radiation hardness necessary. Therefore, quartz fibres are used as active material, while steel is used as absorber material. The energy resolution of the HCAL system is

$$\frac{\sigma}{E} \sim \frac{100\%}{\sqrt{E}} + 0.05 \quad . \quad (3.2)$$

### 3.5 Muon system

Detection of muons with high accuracy is one of the main goals of the CMS detector. The muon system is not only used for identifying muons and measuring their momentum, but also for triggering events. Due to the large area that has to be covered (25 000 m<sup>2</sup>), cheap and reliable detectors are used. In the barrel region ( $|\eta| < 1.2$ ) drift tube (DT) chambers are used. Cathode strip chambers (CSC) are used in the endcap region ( $0.9 < |\eta| < 2.4$ ), where a higher muon flux is expected and the magnetic field is not uniform anymore. DTs and CSCs can both be used to trigger on the  $p_T$  of the muons with a fairly good standalone resolution, good efficiency and high background rejection. Resistive plate chambers (RPC) are used additionally to both the CSC and DT detectors in the region of  $|\eta| < 1.6$ . Due to their fast response time good time resolution is achieved, which allows for a measurement of the originating bunch crossing of a muon. RPCs are also used as additional fast and independent trigger. An overview of the positions of the different muon detectors is given in Fig. 3.4. To achieve best momentum resolution, tracker and muon system hits are used in combination.

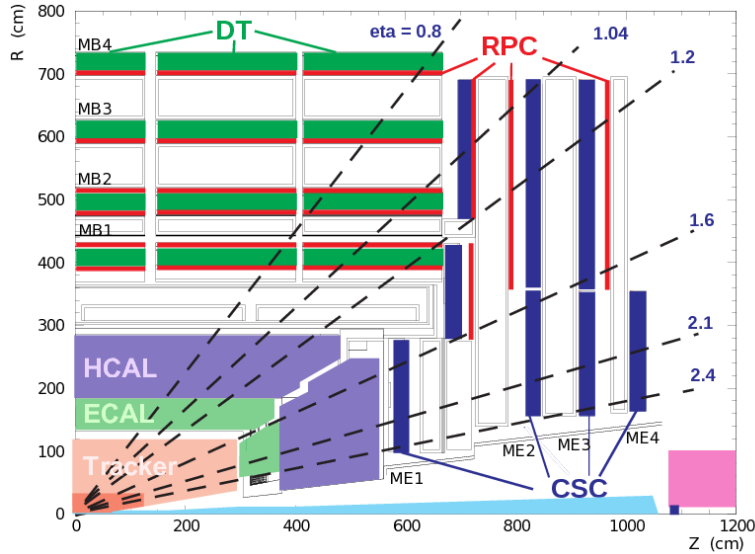


FIGURE 3.4: Sectional view of the CMS muon system [49]. Tracker, ECAL and HCAL positions within the detector are indicated as well.

### 3.6 Trigger and data acquisition system

The needed file storage for all the measured information of one event accounts for about 1-2 MB if the data is uncompressed. With a time distance of only 25 ns between two bunches, the collision rate inside the CMS experiment reaches 40 MHz. Saving all events would therefore require a bandwidth of about 60 TB/s, summing up to data of over 5 EB per day. A two stage trigger system is therefore used to reduce the number of events and preselect interesting physics events. The first trigger, or Level 1 (L1), is made out of custom-designed electronics. The second trigger, or High Level Trigger (HLT), is software based and runs on a farm of about 1000 processors. The L1 trigger has a reduced output rate of below 100 kHz, with data coming from the detector being held in a pipeline. The decisions of L1 are not based on the full detector information, but on coarse segmented data from the calorimeters and the muon system. A reduction factor of about 100 to 1000 is achieved by the L1 trigger. The HLT already uses the full data and implements a more complex event reconstruction. Therefore, the data acquisition system (DAQ) has to handle data input at a rate of maximum 100 kHz coming from the L1 trigger, with a data rate of about 100 GB/s, coming from a large number of data sources. This data is then processed by the event filter farm of the HLT and reduced by another factor of 1000. The output rate is reduced to 100 Hz.

## Chapter 4

# Event reconstruction and selection

Events and objects (e.g. leptons and jets) are reconstructed with an algorithm that uses all available subdetector information, called particle flow algorithm (PF) [50, 51]. This algorithm consists of three basic steps: First, the fundamental elements, namely the charged-particle tracks and the calorimetric clusters, are reconstructed. The tracks provide a precise measurement of the transverse momentum  $p_T$  as well as the direction of charged particles at the primary vertex. The calorimeter clustering algorithm has four major purposes. It detects and measures the energy of stable neutral particles like photons and neutral hadrons, and separates these particles from energy deposits from charged hadrons. Additionally, electrons and corresponding Bremsstrahlung photons are reconstructed and identified. Furthermore, the clustering supports the energy measurement of charged hadrons in case of inaccurate track measurements due to low quality or high  $p_T$  tracks. Next, the fundamental elements are combined to blocks by a linking algorithm to get a full reconstruction of each particle. For each block, the final particle flow algorithm reconstructs and identifies all contained particles. Tracks and clusters of already identified particles are then gradually removed from the blocks. First, muons are identified and the corresponding tracks are removed. Then, the tracks and ECAL clusters of identified electrons are discarded for further processing of the block. Remaining tracks are then linked with calorimeter clusters. Track momentum and calibrated calorimetric energy are compared and objects identified based on the result. If the calibrated calorimetric energy is smaller than the track momentum by a large amount, a relaxed search for muons or fake tracks is performed. On the other hand, if the track momentum is smaller than the calorimetric energy, a neutral hadron or photon is identified. Reasonable agreement between the two measurements is required to

identify charged hadrons. ECAL and HCAL clusters which were not successfully linked with tracks are associated with photons or neutral hadrons.

Events for this analysis are selected based on the reconstructed objects. Different criteria play a role in the selection: To be selected, objects need to fulfill certain identification criteria. Only events with exactly one charged lepton passing these IDs are selected. Events containing additional leptons with lowered thresholds and looser ID requirements are vetoed to avoid overlap with analyses looking at multileptonic events. The later described analysis strategy is optimized for leptons with a minimum transverse momentum of  $p_T > 25$  GeV. These leptons are coming from W boson decays, and therefore leptons originating from other physical objects are rejected. Isolation criteria, requiring a minimum distance of lepton tracks and jets, are defined.

## 4.1 Electrons

Electrons are reconstructed by associating tracks from the silicon detector with energy clusters in the ECAL. To maximize the performance, a combination of a stand-alone approach with the PF algorithm is used [52, 53]. In the ECAL, the energy of an electron can spread out over several crystals. However, if the loss of energy of the electron due to Bremsstrahlung is small and a central hit in a crystal is produced, the spread will be narrow. For a 120 GeV electron, about 97% of the energy will be contained in one  $5 \times 5$  crystal cluster. If Bremsstrahlung is emitted, a large fraction of the electrons energy will be radiated. Therefore, collecting the energy of the radiated photons is crucial. Photons mainly spread in the transverse plane due to the magnetic field which is bending the electron track in the transverse plane. The forward spread is mostly negligible. Dedicated algorithms are used to cluster crystals to reconstruct the initial energy of the electron.

Tracks are reconstructed using the standard Kalman filter (KF), which is used for all charged particles, is more challenging for electrons due to the change in curvature induced by Bremsstrahlung [54, 55]. Since the used algorithm for collecting tracker hits is complex and therefore time consuming, the selection of the first pair or triplet of hits which seed the reconstruction is crucial for the efficiency. A combination of two complementary algorithms is used, where the seeding either starts from the ECAL super cluster position and energy, or from tracks which were reconstructed using the general algorithm for charged particles. Additional to the KF, a second approach is used for tracks which fail the procedure described above due to a high amount of Bremsstrahlung. In this case, hits in the tracker are either not collected by the KF algorithm, or collected with

bad quality. Therefore, a Gaussian Sum Filter (GSF) is used to refit the track which better models radiative losses due to Bremsstrahlung [56].

Events with an electron in the final state can only enter the selection if exactly one electron with  $p_T > 25$  GeV passes the tight electron ID working point, defined by the  $e/\gamma$  physics object group. This working point has an average signal efficiency of 70% and background rejection of over 99%, meaning that less than 1% of the misidentified electrons will pass the ID criteria. Additionally, an isolation requirement for electrons is used. Isolation of a lepton is defined as follows: The transverse momenta of all objects around the selected lepton within a predefined cone are summed up and divided by the  $p_T$  of the lepton, which is a measure of the relative activity in the cone. For leptons coming from the decay of a boosted W boson, which will have high  $p_T$ , the isolation cone has a smaller radius than for leptons with low  $p_T$ . Therefore, a floating cone radius is defined (mini isolation):

$$R = \begin{cases} 0.2 & p_{T,lep} \leq 50 \text{ GeV} \\ \frac{10 \text{ GeV}}{p_{T,lep}} & p_{T,lep} \in (50, 200) \text{ GeV} \\ 0.05 & p_{T,lep} \geq 200 \text{ GeV} \end{cases} \quad (4.1)$$

For the selected electron, the value of mini isolation is required to be below 0.1.

Events are rejected if they contain additional electrons with  $p_T > 10$  GeV that pass the veto working point, which is tuned to an average efficiency of 95%, leading to a background rejection of 99 % for electrons in the barrel region and 97% in the endcap region of the CMS detector. The mini isolation of these veto electrons is required to be below 0.4.

## 4.2 Muons

Muon tracks are first reconstructed separately in the inner tracker, referred to as tracker tracks, and in the muon system, called standalone-muon track [57]. Two approaches for a combined reconstruction are used:

In the global muon reconstruction (outside-in) a tracker track is matched to each standalone-muon track by a parameter comparison. The Kalman filter technique is used to fit a global muon track by combining hits from the tracker and standalone muon track. This method is superior to the tracker only fit for high  $p_T$  muons above 200 GeV.

In the tracker muon reconstruction (inside-out) all tracker tracks above a threshold  $p_T$  of 0.5 GeV and  $p > 2.5$  GeV are used as possible muon candidates. The tracks are extrapolated to the muon system, considering the magnetic field and interaction with detector material. As a minimum requirement, one muon segment of DT or CSC hits has to match the track candidate. Further matching between track and segment is performed to obtain final tracker muons. For low momentum muons, tracker muon reconstruction is more efficient.

The overall efficiency of muon reconstruction reaches 99% for tracks inside the geometrical acceptance. If a muon is reconstructed by both approaches, the candidate is merged.

Single muon events require exactly one muon with  $p_T > 25$  GeV (similar to the electron requirement above). The medium muon ID defined by the muon physics object group is used as identification criteria for selected muons. Events with an additional muon with  $p_T > 10$  GeV passing the loose muon ID are rejected. The muon ID uses particle flow event reconstruction. For the selected muon, mini isolation is required to be below 0.2, while it has to be below 0.4 for the additional (veto) muons.

### 4.3 Jets

The result of the hadronization of quarks and gluons is seen as bundle-like structure in experiments, called jets, which are reconstructed from particle flow objects using the anti- $k_t$  jet clustering algorithm [58]. In the analysis described in this thesis, a distance parameter of  $R=0.4$  is used for the anti- $k_t$  algorithm.

The correct jet energy scale (JES) and good jet energy resolution (JER) are of major importance for physics analyses. Jets are calibrated using both data and simulation [59]. These jet energy corrections (JEC) are carried out in several steps to tune reconstructed jet energies close to true values: First, simulated event samples are used to correct for the energy offset induced by additional (mainly soft) proton-proton collisions from the same or neighboring bunch crossings (pile-up or PU). Then, corrections for the  $p_T$  dependence of the jet response of the detector, coming from imperfect calorimeter response, are applied, using CMS detector simulations. Corrections are derived as functions of jet  $p_T$  and  $\eta$ . Finally, residual corrections for differences between data and simulation are applied. Uncertainties on JES are below 1% for  $p_T > 10$  GeV and  $|\eta| < 5.2$  in a wide range of phase space.

Selected jets are required to pass a loose jet identification requirement, defined by the jet and missing transverse energy physics object group. In this analysis, jets are required to have a transverse momentum of at least  $p_T > 30$  GeV and a pseudorapidity  $|\eta| < 2.4$ .

## 4.4 Tagged jets

Jets originating from bottom and, to a limited extent, charm quark hadronization have a distinct signature and can therefore be identified. A variety of tagging algorithms have been implemented and tested [60]. These algorithms utilize discriminant variables such as impact parameters of charged-particle tracks, displaced and secondary vertices. The limited lifetime of hadrons containing bottom quarks leads to a decay within the detector, hence producing secondary vertices. Events containing b-tagged jets are vetoed in this thesis, therefore the identification of b-tagged jets is crucial. The medium working point of the combined secondary vertex (CSV) approach is used, which corresponds to a tagging efficiency of about 70% and a misidentification rate of about 1%, depending on the jet kinematics. Tagging efficiencies measured in simulated samples are shown in Fig. 4.1. Secondary vertices coming from decays related to hadrons containing bottom or charm quarks together with track-based lifetime information are the inputs to the CSV algorithm.

The performance of the b-tagging algorithm can differ between measured data and simulation. Therefore, scale factors are introduced which are measured in control samples in data and then applied to simulated events to reach good agreement of the b-tag multiplicity distribution.

There are two ways to obtain the distributions of b-tagged jets in simulation: The first option is to directly use the number of jets that pass the working point of the b-tagging variable in each event. In data, this is the only way to measure the b-tag multiplicity. The second option is to use a probabilistic approach, where the probability of a jet with particular kinematics to get b-tagged  $p_i$  is measured as a function of jet  $p_T$ ,  $\eta$  and true flavor in simulations. If a jet is really originating from bottom quarks, the probability  $p_i$  is equivalent to the b-tagging efficiency  $\epsilon_i$ . One can then use combinatorics to calculate the probability of an event to contain exactly  $n$  b-tagged jets, which can be used as an event weight.

This way, using a b-tag multiplicity requirement does not reduce the number of events and therefore increases the statistical power of the simulated samples. The usage of scale factors from simulation to data  $SF_i$  can be applied on top of the b-tagging probability

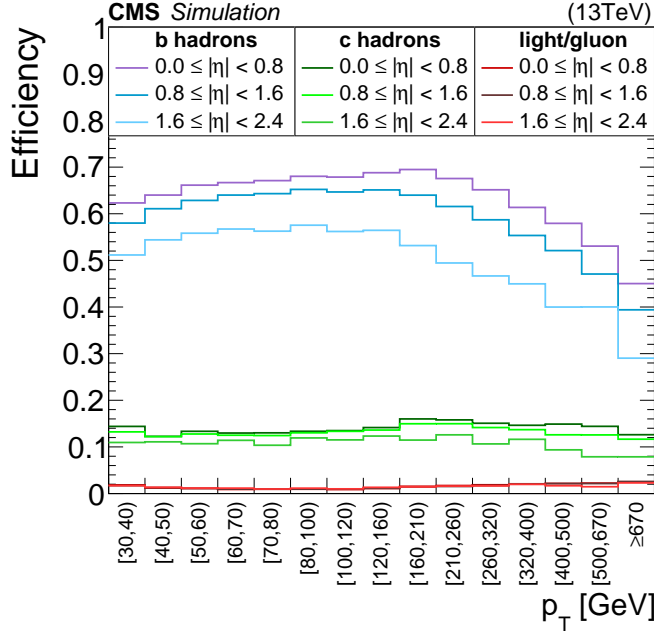


FIGURE 4.1: B-tagging efficiencies and probabilities for jets measured in a simulated  $t\bar{t}$  + jets sample after the baseline selection. Efficiencies for central jets ( $0 \leq |\eta| < 0.8$ ) arising from bottom quarks reach efficiencies of up to 70%. Jets from charm quarks get b-tagged in 8-18% of the cases, relatively independent of the jet  $p_T$ . The mistag rate of jets from light quark hadrons or gluons is in a region of 1-2%.

$p_i$ .

$$P_i = SF_i \cdot p_i \quad (4.2)$$

The probability of an event to contain  $n = 0$  b-tagged jets is then

$$w(0b) = \prod_i (1 - P_i) \quad , \quad (4.3)$$

where the product runs over all jets in the event which all have a  $P_i$  depending on  $p_T$ ,  $\eta$  and simulated true flavor. For one b-tagged jet one gets

$$w(1b) = \sum_i \left[ P_i \prod_j (1 - P_j) \right] \quad (4.4)$$

and similar for higher b-tagged jet multiplicities.

Good agreement between data and simulation is obtained, which is also shown in Fig. 5.3.

## 4.5 Missing transverse energy

Neutral stable particles which only weakly interact with matter can not be detected by the CMS detector. However, these particles can have a significant momentum and, due



to conservation laws, induce a momentum imbalance in the transverse plane, which is named missing transverse energy or  $\cancel{E}_T$ . The initial momentum of colliding particles is zero in the transverse plane. In the beam direction the initial momentum is unknown due to the parton movement within the proton. Therefore,  $\cancel{E}_T$  is defined as the negative vector sum of the transverse momentum  $p_T$  of all observed final state particles:

$$\cancel{E}_T = - \sum_i \vec{p}_{T,i} \quad (4.5)$$

Different reconstruction approaches have been introduced [61]. Similar to most of the analyses carried out within the CMS experiment, the sum uses the  $p_T$  of reconstructed particles from the particle flow algorithm. A different definition, using the energy deposits in the calorimeters, is rarely used in other analyses.

In SM processes,  $\cancel{E}_T$  is associated with neutrinos.  $\cancel{E}_T$  is of major importance for searches for physics beyond the SM, like the search described in this thesis. For R-parity conserving SUSY models, the undetectable lightest particles have masses in the 100 GeV regime and therefore lead to a high amount of  $\cancel{E}_T$ .

It can be seen from the definition that magnitude and direction in the transverse plane depend on the quality of the measurements of all the other objects. Additionally, pileup interactions can spoil the  $\cancel{E}_T$  measurement as well. Therefore, its reconstruction has to be studied in detail using data [62]. The scale and resolution are measured in events with no genuine  $\cancel{E}_T$  such as Z boson decays to two leptons.



## Chapter 5

# Searches for SUSY events in the single lepton final state

This work describes the search for SUSY in events with exactly one charged lepton (electron or muon) in the final state, accompanied by a high number of jets, out of which none has to be tagged as originating from a b hadron (b-tagged jet). A similar search in b-tagged channels has been carried out before in the CMS collaboration [63]. This search was sensitive to processes shown in the right figure of Fig. 5.1, called T1tttt. The two top-antitop quark pairs produced in the gluino decays give rise to multiple b-tagged jets and a high jet multiplicity due to hadronically decaying top quarks. No significant excess of data over the predicted SM background was observed.

To expand the discovery potential in Run 2 of the LHC at  $\sqrt{s} = 13$  TeV, channels requiring zero b-tagged jets are added to the analysis. Those are sensitive to processes shown in the left figure of Fig. 5.1, called T5qqqqWW (T5q<sup>4</sup>WW). The pair produced gluinos decay to the lightest neutralino in a one-step cascade decay. This model is well motivated in many SUSY scenarios [28, 64]. Constraints on the gluino masses from previous searches for events from T5q<sup>4</sup>WW processes are not very tight with mass limits being in the range of 900 GeV for searches in the CMS collaboration [65]. These mass limits in the  $m_{\tilde{g}} - m_{\tilde{\chi}_1^0}$  plane are shown in Fig. 5.2 together with a limit plot showcasing the high sensitivity of the analysis method to T1tttt processes.

Events from this signal model give rise to multiple jets, out of which none is originating from a b quark. The b-tagged jet distribution of simulated signal events, shown in Fig. 5.3 and indicated by the colored lines, peaks at zero as expected. The jet multiplicity distribution motivates a requirement of at least five jets.

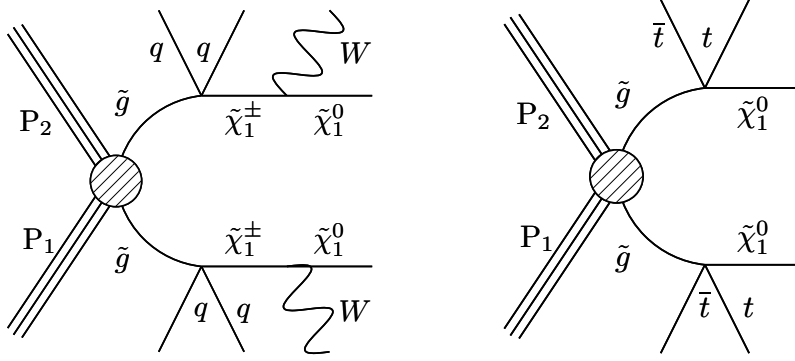


FIGURE 5.1: Gluino mediated SUSY production. The left diagram shows a  $T5q^4WW$  process: A cascade decay of the gluino  $\tilde{g}$  first produces the lightest chargino  $\tilde{\chi}_1^\pm$  in a 3-body decay which in turn will decay into the lightest neutralino  $\tilde{\chi}_1^0$  and a  $W$  boson. The lightest neutralino, which in this model is the lightest supersymmetric particle (LSP), is considered to be stable. The right diagram visualizes a  $T1tttt$  process, where the gluinos decay to top-antitop pairs and the LSP.

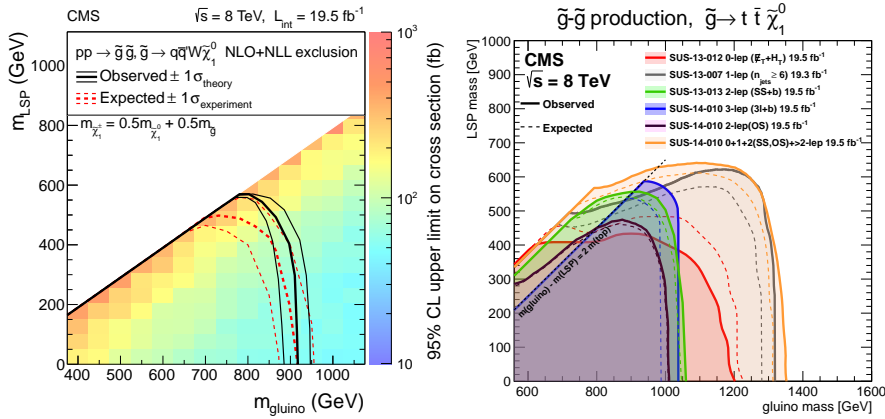


FIGURE 5.2: Limits on gluino and neutralino masses from LHC Run 1 results for the  $T5qqqWW$  model (left) [65] and the  $T1tttt$  model (right) [30].

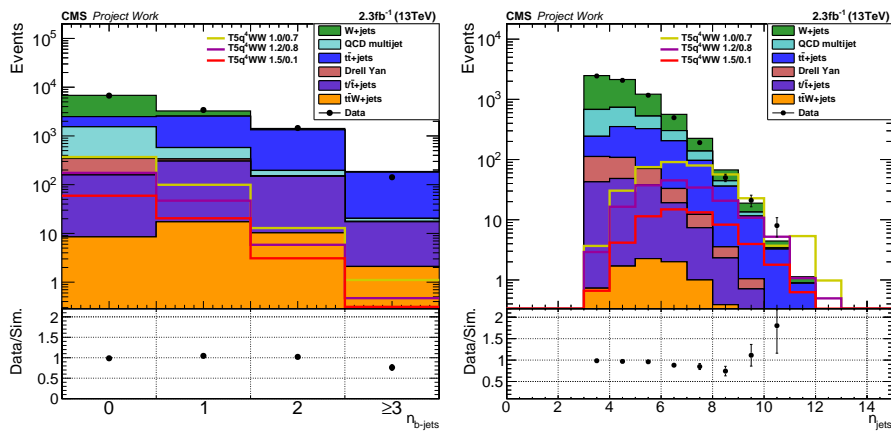


FIGURE 5.3: Left:  $b$ -tagged jet multiplicity distribution for events requiring more than 2 jets. Right: jet multiplicity distribution in the zero  $b$ -tagged jets bin. SM processes are reflected by colored histograms and are stacked on top of each other. The colored lines show three individual benchmark signal model mass points (not stacked), with  $m_{\tilde{g}}/m_{\tilde{\chi}_1^0}$  in TeV. The mass of the chargino is set to  $m_{\tilde{\chi}_1^\pm} = (m_{\tilde{g}} - m_{\tilde{\chi}_1^0})/2$ . Yields of these signals are scaled by a factor of 10 for visibility.

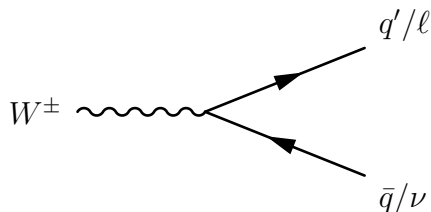


FIGURE 5.4: Diagram of a W boson decaying into a charged lepton and the corresponding antineutrino or a quark / antiquark pair.

In events with a single lepton in the final state one of the two W-bosons decays leptonically, while the other decays hadronically. Both scenarios are shown in Fig. 5.4. Requiring a single lepton in the final state is well motivated: The probability of having exactly one prompt electron or muon in the final state is about 29%, while at the same time backgrounds from QCD multijet events are suppressed compared to searches without a lepton requirement (full hadronic searches).

Signal events will have a high number of jets coming from the gluino decay as well as from the decay of the second W boson. The transverse energy of the jets coming from the gluino decay is dependent on the mass gap between the gluino and the chargino. A few benchmark mass points of gluino, chargino and neutralino are considered to establish the baseline selection criteria, which will be discussed later. The scalar sum of the jet momenta in the transverse plane ( $p_T$ ), also called  $H_T$ , is at least 500 GeV, while the scalar sum of the lepton  $p_T$  and the missing transverse energy ( $\cancel{E}_T$ ), called  $L_T$ , is above 250 GeV.

SM processes that can mimic the signature of the SUSY process lead to non-negligible background. The main background processes are found to be  $t\bar{t}$ +jets and W+jets which similarly to the signal involve a leptonically decaying W boson and multiple jets. In such events with no additional source of  $\cancel{E}_T$ ,  $L_T$  is related to the  $p_T$  and the transverse mass  $M_T$  of the W boson via  $L_T = \sqrt{p_T^2 + M_T^2}$ . Additionally, events with multiple jets and one misidentified lepton in the final state coming from strong processes, called QCD multijet events, contribute to the backgrounds. A more detailed discussion of the background processes and estimation of their yields is given in Sec. 5.3.

To distinguish signal events from the remaining background a discriminative kinematic variable is used. The distribution of the azimuthal angle between the W boson candidate and the lepton coming from its decay,  $\Delta\phi(W, \ell)$ , has a peak at zero and an endpoint related to the mass of the W boson. The W boson candidate is reconstructed using  $\vec{\cancel{E}}_T$  and the lepton  $\vec{p}_T$ . In background events involving only one leptonically decaying W boson, the  $\cancel{E}_T$  is directly associated with the neutrino, while in signal events the neutralinos introduce an additional sizable amount of  $\cancel{E}_T$ , resulting in an arbitrary  $\Delta\phi(W, \ell)$  value

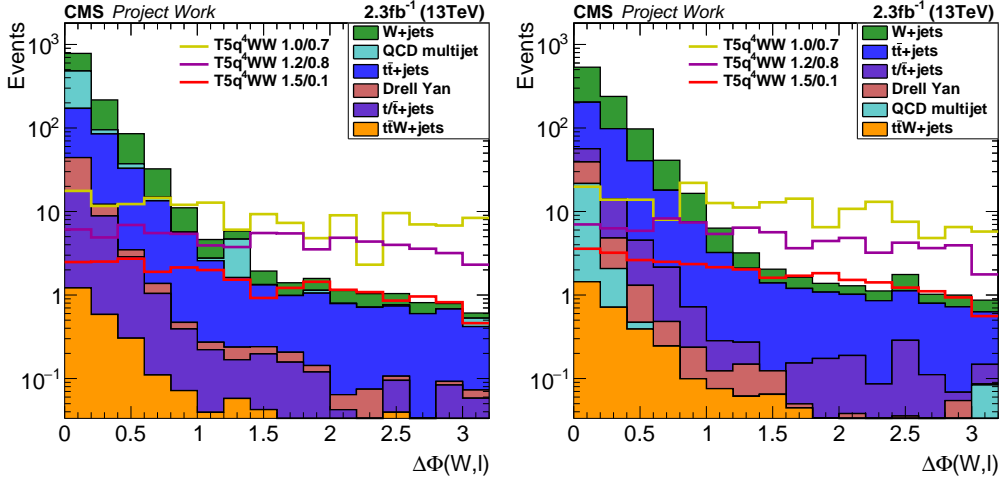


FIGURE 5.5:  $\Delta\phi(W, \ell)$  distributions of SM background processes for electrons (left) and muons (right) taken from simulation. The colored lines (yellow, magenta, red) represent SUSY benchmark model points with the gluino mass  $m_{\tilde{g}}$  and neutralino mass  $m_{\tilde{\chi}_1^0}$  shown in TeV. The distributions of these models are multiplied by a factor 10 for increased visibility.

and therefore an almost flat distribution. Hence, the signal over background ratio in the tail of the  $\Delta\phi(W, \ell)$  distribution is reasonable high for SUSY events to be visible over the SM background as shown in Fig. 5.5.

In this analysis, leptons refer to either electrons or muons. Tau leptons have a short lifetime and decay within the detector. A decay  $W \rightarrow \tau\nu$ ,  $\tau \rightarrow (\mu, e)\nu$  can enter the selection and contribute to the background in the signal regions because of the additional neutrino, which increases the  $\cancel{E}_T$ .

The baseline selection of events is determined using a benchmark point of a  $T5q^4WW$  process as shown in Fig. 5.1, containing gluinos with masses  $m_{\tilde{g}} = 1200$  GeV, charginos with  $m_{\tilde{\chi}_1^\pm} = 1000$  GeV and neutralinos with  $m_{\tilde{\chi}_1^0} = 800$  GeV.  $H_T$ ,  $L_T$  as well as jet multiplicity are used to describe this baseline selection. Considering the mass difference of the particles, quark jet pairs from the threebody decay of the gluino will have a transverse momentum in the order of 200 GeV each, while the jets coming from the W boson decay will add at least 100 GeV to  $H_T$ . To be as sensitive as possible to SUSY models with low neutralino masses, the minimum requirement on  $L_T$  is set to 250 GeV. The evolution of event counts when applying these cuts on top of each other is shown in Tab. 5.1. The region defined by the baseline selection is subdivided into bins of  $H_T$ ,  $L_T$  and jet multiplicity to obtain a superior signal over background ratio. Finally, a minimum requirement on  $\Delta\phi(W, \ell)$  is used to define the signal regions.

The distributions of the kinematic observables used in the baseline selection are shown in Fig. 5.6. Good agreement between simulation and data is observed.

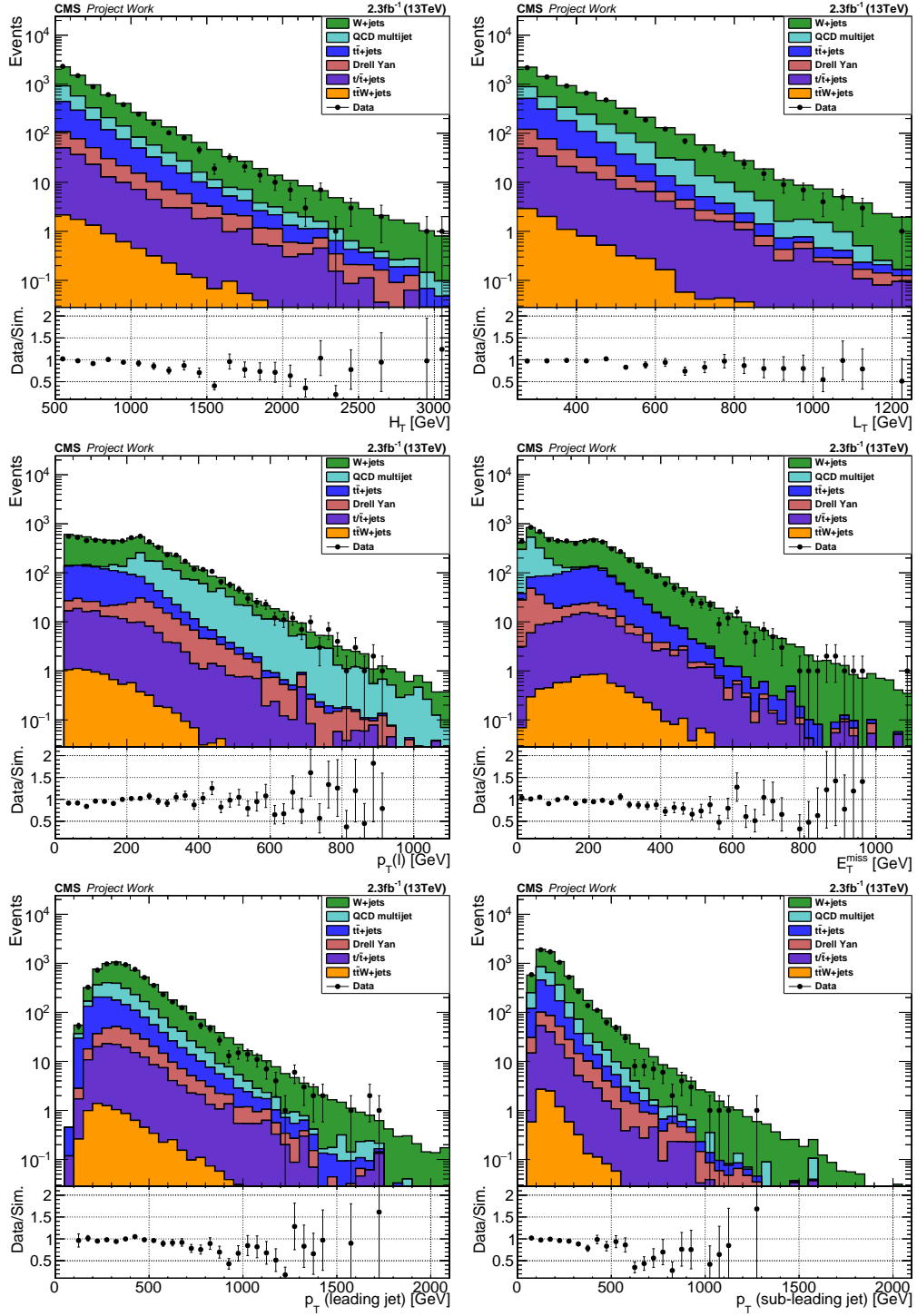


FIGURE 5.6: Distributions of kinematic observables after vetoing b-tagged jets and requiring  $L_T > 250$  GeV,  $H_T > 500$  GeV and at least 3 jets. The ratio of data to simulation is shown in the lower panel. Statistical uncertainties are reflected in the error bars. The event yields of the simulated background backgrounds are stacked on top of each other. Good agreement of simulation and data is observed.  $H_T$  and  $L_T$  distributions are shown in the top row. Lepton  $p_T$  and  $\cancel{E}_T$  are shown in the second row. The bottom row gives distributions of the leading and subleading jet  $p_T$ .

Requirement	T5q <sup>4</sup> WW	T5q <sup>4</sup> WW	$t\bar{t}$ + jets		W+jets	QCD	$t/\bar{t}$	DY	$t\bar{t}W$	All
	1.2/1.0/0.8	1.5/0.8/0.1	2 $\ell$	others						
one lepton	45.9	9.4	7757	70103	73488	28009	5284	6513	356	191513
no veto lepton	43.2	8.9	6471	68371	72986	27400	5144	5221	328	185922
$N_{jet} \geq 5$	35.8	8.2	2868	41571	11453	5838	1388	1076	245	64441
$p_T^{j2} > 80$ GeV	33.9	8.2	2477	35572	10299	5102	1229	964	218	55862
$H_T > 500$ GeV	27.4	8.2	1301	17655	6490	2377	711	575	143	29253
$L_T > 250$ GeV	21.2	7.9	323	2380	1388	250	183	70	29	4623
$n_{b-jet} = 0$ and $\Delta\phi > 0.75$	11.0	3.5	18	5.7	14	1.2	1.1	0.8	0.7	50

TABLE 5.1: Event counts from simulation for the different backgrounds after a baseline requirement of  $H_T > 350$  GeV, normalized to  $2.3\text{fb}^{-1}$ . Event counts of two signal mass points of the T5q<sup>4</sup>WW model with gluino mass  $m_{\tilde{g}}$ , chargino mass  $m_{\tilde{\chi}_1^\pm}$  and neutralino mass  $m_{\tilde{\chi}_1^0}$  in TeV are listed as well.

The analysis was first optimized with respect to an expected integrated luminosity of  $10 \text{ fb}^{-1}$  for the 2015 run of the LHC. As a result, events are subdivided into  $L_T$  bins of  $[250,350)$ ,  $[350,450)$  and  $[450,\infty)$  GeV,  $H_T$  bins of  $[500,750)$ ,  $[750,1000)$  and  $[1000,\infty)$  GeV. Additionally, three jet multiplicity bins requiring exactly 5, 6 to 7 and  $\geq 8$  jets are used. This sums up to a total number of 27 bins. For the lower integrated luminosity finally delivered in 2015,  $H_T$  bins are collapsed to increase the event counts in sideband and control regions as well as to increase sensitivity to the targeted benchmark signal model mass points. The 27 bins are therefore reduced to 13.

The  $\Delta\phi(W, \ell)$  threshold that separates signal regions from control regions is optimized for the different search bins. In events with high  $L_T$  and high jet multiplicity, the peak of the distribution of SM background is narrower, allowing for a looser  $\Delta\phi(W, \ell)$  requirement and therefore a higher signal over background ratio. This observation is shown in the two  $\Delta\phi(W, \ell)$  distributions of Fig. 5.7. Requiring low  $L_T$  (between 250 and 350 GeV) results in a slower falling distribution, while a high  $L_T$  requirement (above 450 GeV) results in a steeper descent. An inclusive  $H_T$  requirement (above 500 GeV) and a jet multiplicity requirement of 6 to 7 jets is applied in both cases.

The final collection of search bins is shown in Tab. 5.2.

In summary, the baseline requirements for events are:

- one prompt muon or electron with  $p_T > 25$  GeV and  $\eta < 2.4$ ,
- no additional veto muon or electron with  $p_T > 10$  GeV and  $\eta < 2.4$ ,
- $L_T > 250$  GeV,
- $H_T > 500$  GeV,
- $n_{jet} \geq 5$  (3 for sidebands)



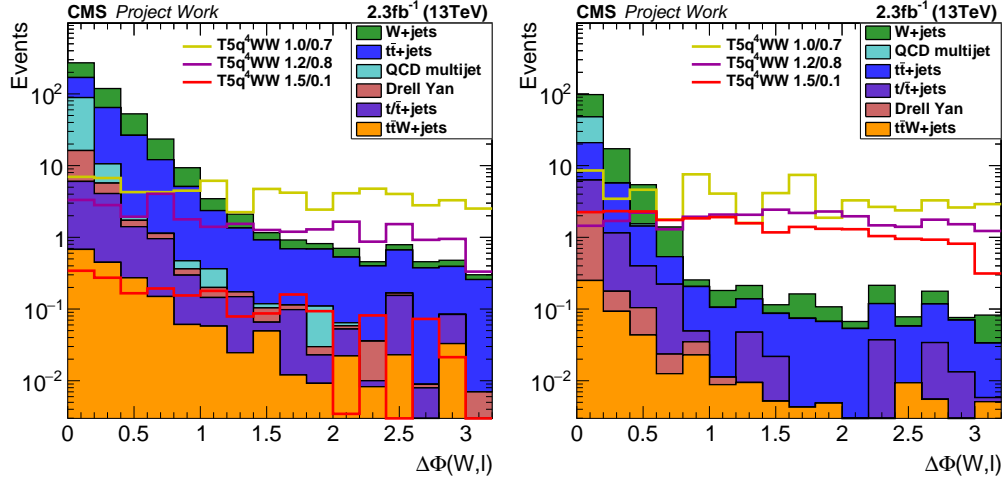


FIGURE 5.7:  $\Delta\phi(W, \ell)$  distributions with wider peak due to low  $L_T$  (between 250 and 350 GeV, left) and narrower peak ( $L_T$  above 450 GeV, right). Signal distributions are scaled up by a factor of 10 for visibility.

$n_{\text{jet}}$	$L_T$ [GeV]	$H_T$ [GeV]	Bin name	$\Delta\phi(W, \ell)$
5	[250, 350]	$\geq 500$	LT1, HTi	1.0
	[350, 450]	$\geq 500$	LT2, HTi	1.0
	$\geq 450$	$\geq 500$	LT3, HTi	1.0
[6, 7]	[250, 350]	[500, 750]	LT1, HT1	1.0
		$\geq 750$	LT1, HT23	1.0
	[350, 450]	[500, 750]	LT2, HT1	1.0
		$\geq 750$	LT2, HT23	1.0
$\geq 450$	[500, 1000]	LT3, HT12	0.75	
	$\geq 1000$	LT3, HT3	0.75	
8 ^1	[250, 350]	[500, 750]	LT1, HT1	1.0
		$\geq 750$	LT1, HT23	1.0
	[350, 450]	$\geq 500$	LT2, HTi	0.75
	$\geq 450$	$\geq 500$	LT3, HTi	0.75

TABLE 5.2: Signal regions used in this analysis, optimized for an integrated luminosity of  $3 \text{ fb}^{-1}$ .

- no b-tagged jet ( $n_{\text{b-tag}} = 1$  for  $t\bar{t}$  + jets sideband),
- leading and subleading jet  $p_T > 80$  GeV and
- for signal regions:  $\Delta\phi(W, \ell) \geq 1/0.75$ .

## 5.1 Simulated samples

Simulated samples are used to develop and validate the background estimation method. Samples for background and signal processes are generated using Monte Carlo techniques. Events are simulated in leading- or next-to-leading-order precision of perturbation theory using the MADGRAPH or POWHEG generators [66, 67]. The parton showering and hadronization is handled by PYTHIA8 [68]. To enhance the statistical power of the simulated samples, combinations of different samples are used whenever possible. For example there are full single leptonic and dileptonic  $t\bar{t}$ +jets samples, which are combined with a totally inclusive sample and ones binned in  $H_T$ .

Event weights  $w$  are used to be able to compare the simulated samples with data. They are calculated as

$$w = \frac{\sigma}{N} \int \mathcal{L} dt \quad (5.1)$$

where  $\sigma$  denotes the cross section of the event and  $N$  the number of simulated events. This fraction is multiplied with the integrated luminosity. Additional weights are applied multiplicatively to cover residual differences between simulation and data. Inefficiencies of lepton identification and triggers are covered by a constant factor. Differences in the b-tagging efficiency are applied to each event independently. The mismodeling of the number of inelastic scatterings per bunch crossing (pile-up) is corrected with a weight as well with an almost negligible effect. Additionally, a weight covering the difference of the  $p_T$  spectrum of top quarks, which is found to be softer in data than in simulation and is expected to be due to a next-to-next-to-leading-order effect, is applied [69].

## 5.2 Triggers

Two separate high level triggers (HLT) for muons and electrons are used to trigger single leptonic events. Both HLTs trigger on single electronic or muonic events with an  $H_T$  threshold of 350 GeV. Only a very loose isolation of the lepton is required, while there is no  $\cancel{E}_T$  threshold.

The total efficiency is measured against reference triggers with no threshold either on the lepton  $p_T$  to measure the efficiency in the leptonic leg, or on the hadronic activity  $H_T$  to measure the efficiency in the hadronic leg. The hadronic leg reaches an efficiency of 100% for muons and 99.8% for electrons which is shown in Fig. 5.8. The leptonic leg is about 94% efficient, which results in a total efficiency of 94% and is shown in Fig. 5.9. Full efficiency of the triggers is also reached well below the baseline requirement of 250 GeV on  $L_T$ . In case of high event rates, only a fraction of triggered events can

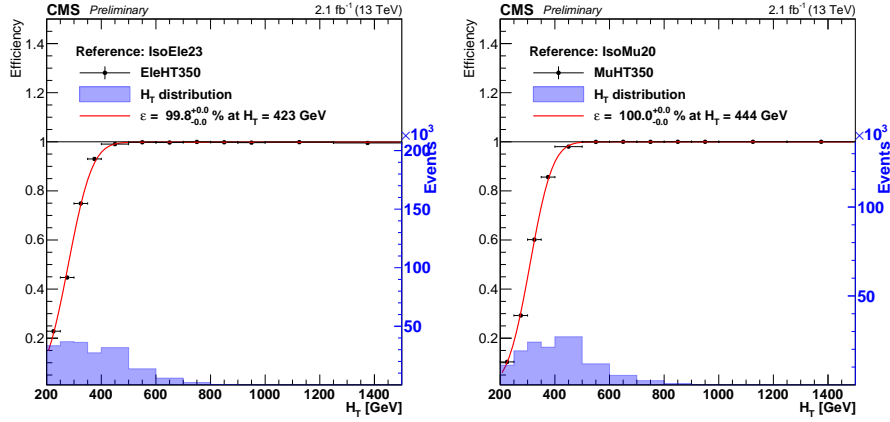


FIGURE 5.8: Measurement of the trigger efficiency in the  $H_T$  leg for events with a single electron (left) or muon (right) in the final state [70]. A trigger on lepton  $p_T$  with no threshold on  $H_T$  is used as reference. The  $H_T$  distributions of events passing the trigger are reflected in the blue histogram. The plateau is reached below the baseline requirement on  $H_T$  of 500 GeV.

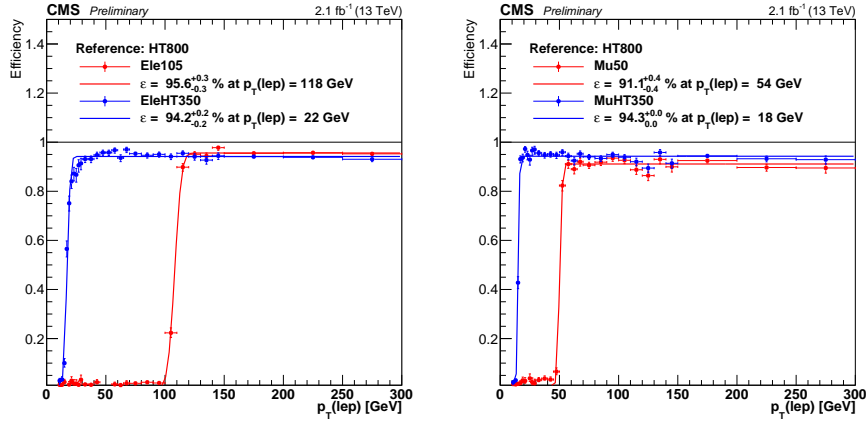


FIGURE 5.9: Measurement of the trigger efficiency in the lepton leg for events with a single electron (left) or muon (right) in the final state [70]. A trigger on  $H_T$  with no lepton  $p_T$  threshold is used as reference. As a comparison, the efficiency of triggers with higher lepton  $p_T$  threshold is shown in red. The efficiency of the trigger used in this analysis is shown in blue. The plateau is reached below the baseline requirement on lepton  $p_T$  of 25 GeV.

be saved. Triggers then do have an individual prescale which is proportional to this fraction. However, the used triggers are unprescaled, meaning that all triggered events were saved.

### 5.3 Background estimation

A robust prediction of background events coming from SM processes is essential for searches for physics beyond the SM. Besides the signal regions (SR) described in Tab. 5.2 which are directly used to look for signal events, corresponding control regions (CR)

with inverted  $\Delta\phi(W, \ell)$  requirement are defined. The combination of signal and control regions will be called mainbands (MB). A data-driven estimation of yields of the leading background processes in the signal regions is performed using the  $\Delta\phi(W, \ell)$  variable, while yields of residual other backgrounds are taken directly from simulation (MC).

The yield of background events in mainband signal regions can be written as the sum of its components:

$$N_{\text{MB}}^{\text{SR}} = N_{W+\text{jets}}^{\text{SR}} + N_{t\bar{t}}^{\text{SR}} + N_{\text{other}}^{\text{SR(MC)}} \quad (5.2)$$

The ratio between event yields in the signal and control regions is written as

$$R_{\text{CS}} = \frac{N(\Delta\phi \geq x)}{N(\Delta\phi < x)} = \frac{N_{\text{SR}}}{N_{\text{CR}}} \quad (5.3)$$

If the  $R_{\text{CS}}$  value of backgrounds is known, event yields in the SR can simply be rewritten as

$$N_{\text{SR}}^i = R_{\text{CS}}^i \cdot N_{\text{CR}}^i \quad (5.4)$$

Sideband regions (SB) with orthogonal requirements in terms of jet and b-tagged jet multiplicity are defined in order to measure independently the  $R_{\text{CS}}^i$  values of the different background processes. It is shown in Fig. 5.16 that  $R_{\text{CS}}$  can be considered as independent from jet multiplicity.  $L_{\text{T}}$  and  $H_{\text{T}}$  requirements are also applied in the sideband region to account for a non-negligible dependence on these kinematic observables. Sideband regions are chosen carefully to measure  $R_{\text{CS}}$  in bins where the desired process is enriched. To measure  $R_{\text{CS}}$  of one single process, the sideband regions need to be cleaned from other SM processes. Although QCD multijet events do not populate the signal regions of the mainbands, their contamination of sideband and control regions has to be corrected for. Again, a data driven approach to estimate QCD multijet events is chosen which is explained in detail in Sec. 5.3.2. An overview of the chosen mainband and sideband regions is given in Fig. 5.10.

The major difference between sideband and mainband regions is the different jet multiplicity.  $R_{\text{CS}}$  is measured in regions with low jet multiplicity and applied in high jet multiplicity regions. Therefore,  $R_{\text{CS}}$  has to be independent of jet multiplicity.

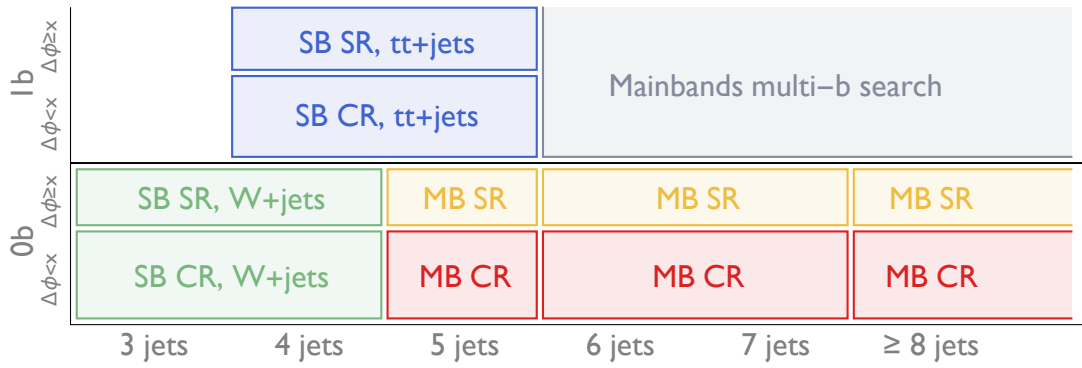


FIGURE 5.10: Visualization of the different kinematic regions in the b-tagged jet multiplicity and jet multiplicity plane. Sideband regions are colored in green (W+jets SB) and blue ( $t\bar{t}$ +jets SB). Yields measured in the control regions of the mainband (red) are multiplied by the  $R_{CS}$  value determined in the sidebands to obtain an estimate of the background yields in the mainband signal regions (yellow). The gray area is used for mainbands in a different channel of the analysis and therefore not available as sideband region.

### 5.3.1 Background composition in control regions

As mentioned previously, different  $R_{CS}$  values for the main background constituents are used. Therefore it is necessary to determine the yields of these processes in the control regions separately. Fractions of the different background processes in the control regions  $f_i$  are measured using a likelihood fit of templates to data. These templates of b-tag multiplicity distributions are extracted from simulation. Therefore, the b-tagged jet veto is abandoned for this step. Templates and yields of QCD multijet events are constructed from predicted QCD multijet event yields in the different b-tag multiplicity bins, while templates of residual other backgrounds are directly taken from simulation and scaled to the simulated yields. The charge asymmetry of W+jets events is accounted for by using separate templates for events containing a positive or negative charged lepton and fitting to data separately, but simultaneously.  $t\bar{t}$  + jets and QCD multijet processes are considered to be charge symmetric, while the other background templates are also constructed separately for positive and negative charged leptons. The charge asymmetry also manifests itself in  $R_{CS}$  values, which is shown in Tab. 5.3. Results of the b-tag multiplicity fits are shown in Fig. 5.11. Good agreement between fit and data is observed over all the different kinematic bins.

A comparison of the background composition in data and simulation for the mainband and the W+jets sideband is shown in Fig. 5.12. The b-tag template fit method is verified by comparing measured yields to true yields in simulation. Good closure between these two values is observed. The measured composition in data differs between simulation and data in regions with high jet multiplicity, but good agreement between simulation and data is observed in less extreme kinematic regions.

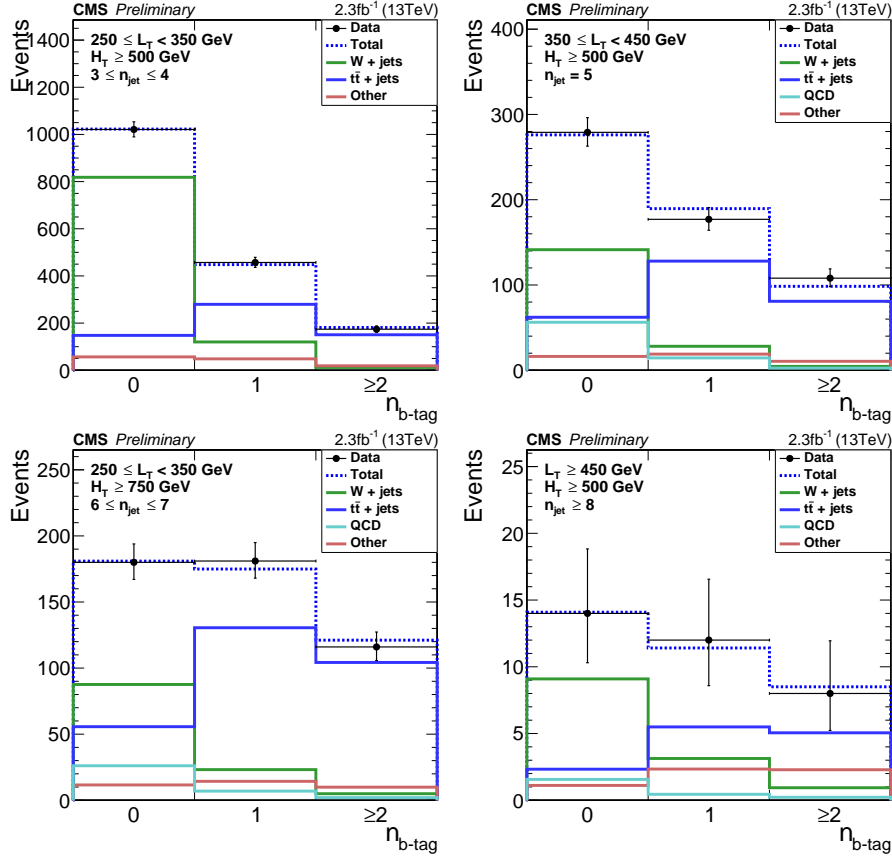


FIGURE 5.11: Results of the b-tag multiplicity fit to measure relative fractions of constituent backgrounds in the control regions ( $\Delta\phi(W, \ell) < x$ ) [71]. Fits in: 3-4 jet sideband requiring  $L_T \in [250, 350)$  GeV,  $H_T \geq 500$  GeV (top left). 5 jets mainband requiring  $L_T \in [350, 450)$  GeV,  $H_T \geq 500$  GeV (top right). 6-7 jets mainband requiring  $L_T \in [250, 350)$  GeV,  $H_T \geq 500$  GeV (bottom left).  $\geq 8$  jets mainband requiring  $L_T \geq 450$  GeV,  $H_T \geq 500$  GeV (bottom right).

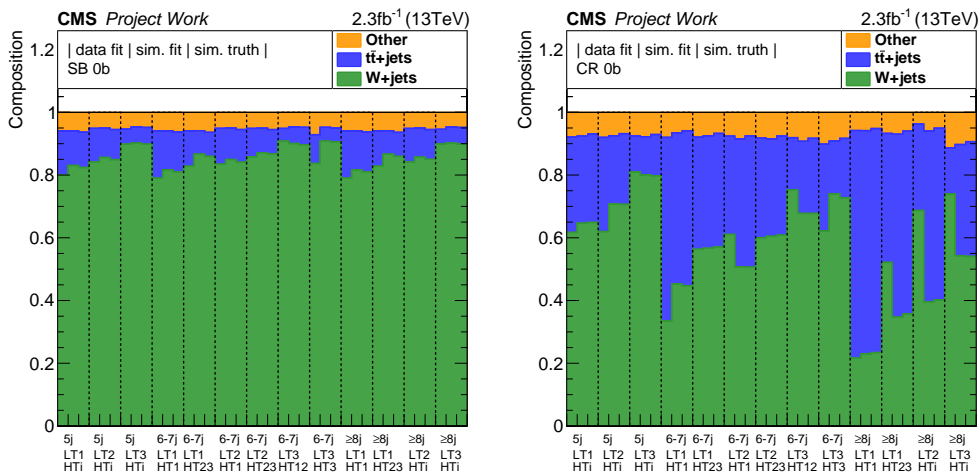


FIGURE 5.12: Relative composition of backgrounds in control regions. For each search region (introduced in Tab. 5.2) fractions measured in data, using a b-tag multiplicity fit on simulated samples and directly from simulation are shown. Left plot: CR of the sideband used to measure  $R_{CS}$  of W+jets. Right plot: CR of the mainband.

$n_{\text{jet}}$	$L_T$ [GeV]	$H_T$ [GeV]	$R_{CS}$			
			$\ell^+$		$\ell^-$	
5	[250, 350]	$\geq 500$	0.0182	$\pm$ 0.0006	0.0121	$\pm$ 0.0006
	[350, 450]	$\geq 500$	0.0081	$\pm$ 0.0006	0.0065	$\pm$ 0.0007
	$\geq 450$	$\geq 500$	0.0061	$\pm$ 0.0005	0.0045	$\pm$ 0.0006
[6, 7]	[250, 350]	[500, 750]	0.0143	$\pm$ 0.0008	0.0091	$\pm$ 0.0007
		$\geq 750$	0.0275	$\pm$ 0.0009	0.02	$\pm$ 0.001
	[350, 450]	[500, 750]	0.0065	$\pm$ 0.0008	0.0044	$\pm$ 0.0008
		$\geq 750$	0.0117	$\pm$ 0.0008	0.0113	$\pm$ 0.0013
	$\geq 450$	[500, 1000]	0.0099	$\pm$ 0.0007	0.0074	$\pm$ 0.0011
		$\geq 1000$	0.0111	$\pm$ 0.001	0.0076	$\pm$ 0.0011
$\infty$ $\wedge$	[250, 350]	[500, 750]	0.0143	$\pm$ 0.0008	0.0091	$\pm$ 0.0007
		$\geq 750$	0.0275	$\pm$ 0.0009	0.02	$\pm$ 0.001
	[350, 450]	$\geq 500$	0.0202	$\pm$ 0.001	0.0133	$\pm$ 0.001
	$\geq 450$	$\geq 500$	0.0101	$\pm$ 0.0006	0.0074	$\pm$ 0.0009

TABLE 5.3:  $R_{CS}$  values of W+jets events measured in the sidebands (3/4 jets, 0b) in simulated W+jets samples, split in positive and negative charged leptons.  $R_{CS}$  for positive charged leptons tends to larger values due to polarization effects.

Uncertainties on the templates are assigned using the bootstrapping method [72]. Therefore, random histograms with similar numbers of entries are sampled from simulated templates. With the 100 histograms generated for each template it is possible to extract distribution around the central value, and therefore also an uncertainty. The standard deviation around the mean is taken and propagated through to the fit results.

### 5.3.2 QCD multijet events

QCD multijet events contaminate sideband regions as well as control regions of the mainband. Therefore, yields have to be estimated prior to the prediction of the SM background in the mainband signal regions. Yields of events arising from QCD multijet processes are predicted using the LP variable, which is defined as

$$L_P = \frac{p_T(\ell)}{p_T(W)} \cdot \cos(\Delta\phi(W, \ell)) \quad . \quad (5.5)$$

It describes the polarization of semileptonic decays, e.g. W decays. QCD multijet events only enter the selected events through faked leptons, meaning a jet that is misidentified as lepton. This leads to a  $L_P$  distribution which is different compared to electroweak processes containing real leptons. The number of faked leptons is kept small by tight lepton identification criteria. However, for estimating the number of events coming from these processes, a higher number of events is necessary. To overcome the issue of the rather small amount of these events, the cuts on lepton identification variables are

loosened to enrich the sample with events containing lepton fakes. Templates of the  $L_P$  distribution from simulation are then used to fit events with fake leptons. The yield obtained by this method is then scaled using the ratio between events with looser and tighter lepton identification criteria. A more detailed description of the method can be found in [73].

The robustness of this method is checked both in simulation which is shown in Fig. 5.13 and, using a second discriminating variable, in data. Sizable amount of  $\cancel{E}_T$  in QCD multijet events only arises from under- or overmeasured jet  $p_T$ . Therefore, the angle between the leading jet and  $\cancel{E}_T$  in the transverse plane,  $\Delta\phi(j, \cancel{E}_T)$ , has a distinct distribution.  $\cancel{E}_T$  is either parallel or anti-parallel to the leading jet. This feature can be used to fit a template of QCD multijet events to data. The templates are extracted from simulation, only using the baseline requirements to obtain a smooth distribution albeit the low statistics available. Templates of other background processes are measured in simulation applying the same  $H_T$ ,  $L_T$  and  $n_{\text{jet}}$  requirements as for data. A likelihood fit is then used to fit these templates to data. The result in Fig. 5.13 shows good agreement between fit and data, as well as a ratio close to unity between the two methods as long as statistics are sufficient.

### 5.3.3 $t\bar{t}$ + jets events

Top quarks are mainly produced in pairs in quark-quark annihilation or gluon fusion processes. A diagram of a typical process is shown in Fig. 5.14. Top quarks have a short lifetime and predominantly decay into bottom quarks and W bosons. Although the process involves two jets from bottom quarks, these events can pass the b-tagged jet veto as a result of the limited efficiency of the b-tagging algorithms. Apart from the b-tagged jets, this process has a signature that is close to the targeted signal events. Therefore,  $t\bar{t}$  + jets events are one of the two leading backgrounds, either through events coming from semileptonic decays where one of the two W bosons decays to leptons, while the other decays to hadrons, or dileptonic decays where one of the charged leptons is either misidentified or out of the acceptance of the detector. The majority of  $t\bar{t}$  + jets events contributing to the backgrounds in this analysis only has one charged lepton in the final state. The two different types of  $t\bar{t}$  + jets events have different  $R_{\text{CS}}$  values, shown in Fig. 5.16. In events with two generated leptons, the reconstruction of the W boson fails due to the additionally introduced  $\cancel{E}_T$  from the second neutrino, which leads to larger  $R_{\text{CS}}$  values. Nevertheless, the total  $R_{\text{CS}}$  values of  $t\bar{t}$  + jets can be considered as independent from the jet multiplicity. Still, uncertainties for potential dependencies are assigned, which are described in Sec. 6.3.1.



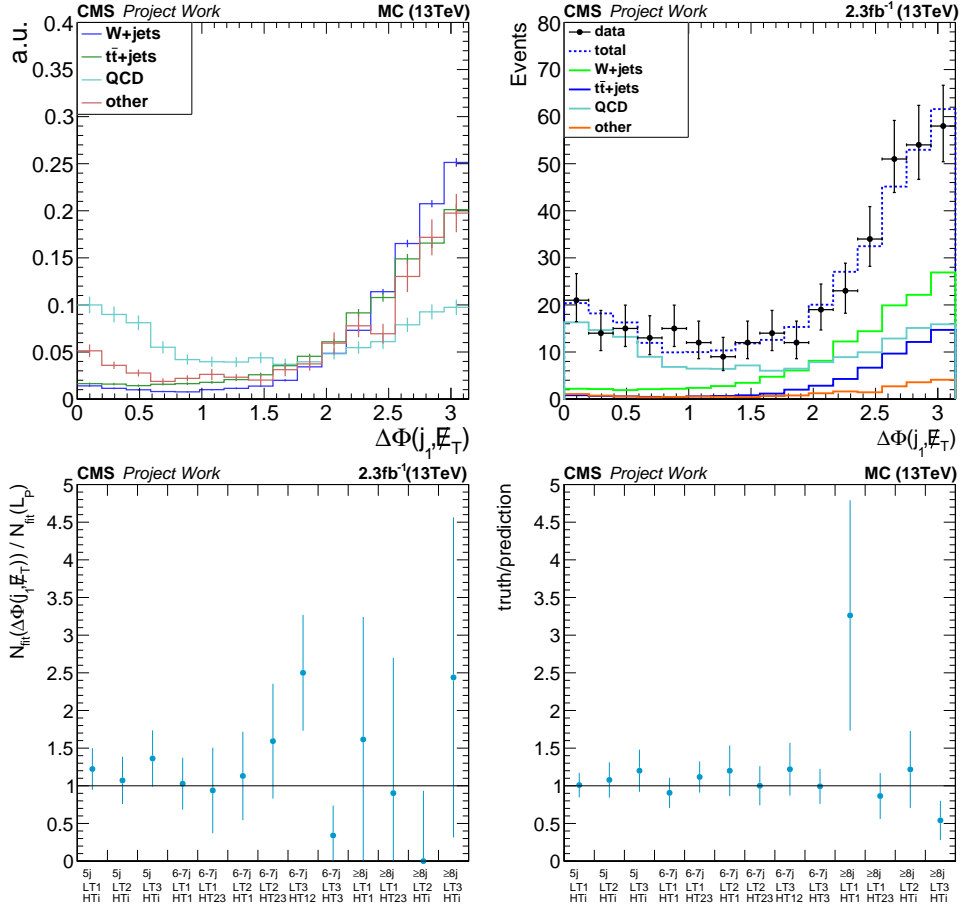


FIGURE 5.13: The upper left plot shows templates of four different background processes. The result of fitting these templates to data is shown in the upper right figure. The ratio between the yields obtained in data with this method and the more sophisticated  $L_P$  method is shown in the lower left plot. A closure test for the QCD multijet events prediction in simulation is shown in the lower right figure.

The  $\Delta\phi(W, \ell)$  distribution of  $t\bar{t} + \text{jets}$  events with different decays of the W bosons is shown in Fig. 5.15. The distribution of events with two generated (two leptonically decaying W bosons) and one reconstructed lepton (medium blue) is more uniform than the distribution of events with only one generated lepton (one leptonically decaying W boson, light blue), resulting in a larger  $R_{CS}$  value for these events. Events with no generated lepton do not play an important role (dark blue).

$R_{CS}$  values of  $t\bar{t} + \text{jets}$  events are measured in sideband regions requiring four to five jets. To keep contamination from W+jets events low and increase the purity of  $t\bar{t} + \text{jets}$  events, one of the jets is required to be b-tagged. Additionally, the expected yield of QCD multijets events is subtracted, resulting in

$$R_{CS}^{\text{data}}(1b, n_{jet} \in [4, 5]) = \frac{N_{\text{data}}^{SR} - N_{\text{QCD}}^{\text{pred}(SR)}}{N_{\text{data}}^{CR} - N_{\text{QCD}}^{\text{pred}(CR)}} \quad (5.6)$$

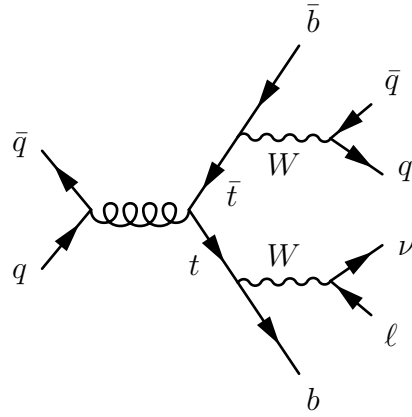


FIGURE 5.14: Diagram of a semi-leptonic  $t\bar{t}$  + jets event. The first  $W$  boson decays to a quark jet pair, while the second one decays to a lepton (electron or muon) and the corresponding neutrino.

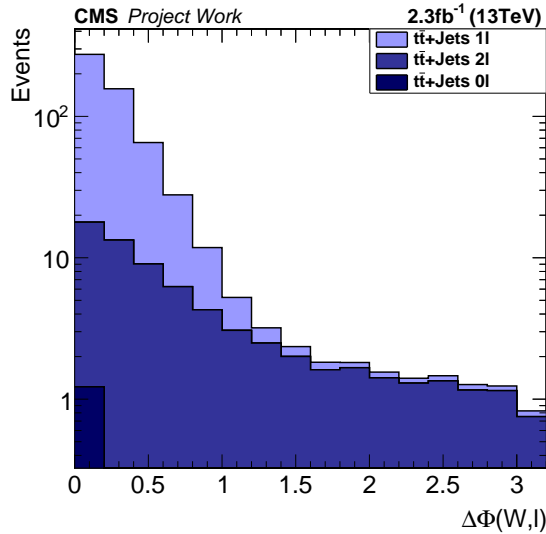


FIGURE 5.15:  $\Delta\phi(W, \ell)$  distribution of  $t\bar{t}$  + jets events from simulation after baseline selection. The events are categorized into three different decay modes, involving zero (dark blue), one (light blue) or two (medium blue) generated leptons.

Two correction factors are defined to account for residual differences between  $R_{CS}$  from the sideband and the mainband regions. First, the potential difference between  $R_{CS}$  determined in a bin requiring one b-tagged jet and the true  $R_{CS}$  with no b-tagged jet is calculated in simulation, called  $\kappa_b$ :

$$\kappa_b = \frac{R_{CS}^{MC}(0b, n_{jet} \in [4, 5], t\bar{t})}{R_{CS}^{MC}(1b, n_{jet} \in [4, 5], EWK)} \quad (5.7)$$

$\kappa_b$  also covers for small contributions from events other than  $t\bar{t}$  + jets and QCD multijets.

$n_{\text{jet}}$	$L_T$ [GeV]	$H_T$ [GeV]	$R_{CS}(4\text{-}5j, 1b) \cdot \kappa_b^{MC}$	$R_{CS}(\text{SR}, 0b)$	$\kappa_{t\bar{t}}$ SR/SB	$\kappa_b$ 0b/1b
5	[250, 350]	$\geq 500$	0.0509 $\pm$ 0.0011	0.0475 $\pm$ 0.0007	0.93 $\pm$ 0.02	1.08 $\pm$ 0.02
	[350, 450]	$\geq 500$	0.0396 $\pm$ 0.0018	0.0369 $\pm$ 0.001	0.93 $\pm$ 0.05	1.11 $\pm$ 0.04
	$\geq 450$	$\geq 500$	0.0385 $\pm$ 0.0027	0.0397 $\pm$ 0.0016	1.03 $\pm$ 0.08	1.36 $\pm$ 0.08
[6, 7]	[250, 350]	[500, 750]	0.0503 $\pm$ 0.0012	0.042 $\pm$ 0.0008	0.83 $\pm$ 0.03	1.09 $\pm$ 0.02
		$\geq 750$	0.053 $\pm$ 0.0022	0.0443 $\pm$ 0.0009	0.84 $\pm$ 0.04	1.08 $\pm$ 0.04
	[350, 450]	[500, 750]	0.0408 $\pm$ 0.0022	0.038 $\pm$ 0.0015	0.93 $\pm$ 0.06	1.14 $\pm$ 0.05
		$\geq 750$	0.0372 $\pm$ 0.0032	0.0339 $\pm$ 0.0013	0.91 $\pm$ 0.09	1.03 $\pm$ 0.07
	$\geq 450$	[500, 1000]	0.0509 $\pm$ 0.0034	0.0524 $\pm$ 0.0025	1.03 $\pm$ 0.08	1.44 $\pm$ 0.08
		$\geq 1000$	0.0441 $\pm$ 0.0069	0.0401 $\pm$ 0.0022	0.91 $\pm$ 0.15	1.17 $\pm$ 0.15
$\geq 8$	[250, 350]	[500, 750]	0.0503 $\pm$ 0.0012	0.0385 $\pm$ 0.0022	0.76 $\pm$ 0.05	1.09 $\pm$ 0.02
		$\geq 750$	0.053 $\pm$ 0.0022	0.0428 $\pm$ 0.0015	0.81 $\pm$ 0.04	1.08 $\pm$ 0.04
	[350, 450]	$\geq 500$	0.0583 $\pm$ 0.0023	0.0528 $\pm$ 0.0026	0.91 $\pm$ 0.06	1.09 $\pm$ 0.04
	$\geq 450$	$\geq 500$	0.0495 $\pm$ 0.0032	0.0371 $\pm$ 0.0028	0.75 $\pm$ 0.07	1.38 $\pm$ 0.07

TABLE 5.4: Summary of  $R_{CS}$  values of  $t\bar{t}$  + jets events measured in simulation and the corresponding  $\kappa_{t\bar{t}}$  and  $\kappa_b$  values.

Next, a residual dependency of  $R_{CS}$  on jet multiplicity, and therefore a difference between  $R_{CS}$  in the sideband and the mainband, is covered by a second correction factor:

$$\kappa_{t\bar{t}} = \frac{R_{CS}^{MC}(0b, n_{\text{jet}}^{\text{SR}}, t\bar{t})}{R_{CS}^{MC}(0b, n_{\text{jet}} \in [4, 5], t\bar{t})} . \quad (5.8)$$

The final  $R_{CS}$  value of  $t\bar{t}$  + jets events is then written as

$$R_{CS}^{t\bar{t}}(0b, n_{\text{jet}}^{\text{SR}}) = \kappa_b \cdot \kappa_{t\bar{t}} \cdot R_{CS}^{\text{data}}(1b, n_{\text{jet}} \in [4, 5]) . \quad (5.9)$$

Both correction values are close to unity. The statistical uncertainties from simulation are propagated to the final results as a systematic uncertainty.  $\kappa_b$  and  $\kappa_{t\bar{t}}$  values are shown in Tab. 5.4.

### 5.3.4 W+jets events

$R_{CS}$  values of W+jets events are measured in sideband regions with three to four jets which are enriched by W+jets events. The purity of W+jets events can be seen from Fig. 5.12. The stability of  $R_{CS}$  over different jet multiplicities is shown in Fig. 5.16. The charge asymmetry of W+jets events is exploited by determining  $R_{CS}$  separately for positive and negative charged leptons. To suppress QCD multijet events, only events with a muon in the final state are used due to the lower misidentification rate for muons. Therefore, no predicted yield of QCD multijet events has to be subtracted. However, contamination coming from  $t\bar{t}$  + jets events is subtracted.  $R_{CS}$  for  $t\bar{t}$  + jets in the sideband region is taken from simulation, while its fractions  $f_{t\bar{t}}$  in the sideband control region are determined using a b-tag multiplicity fit.

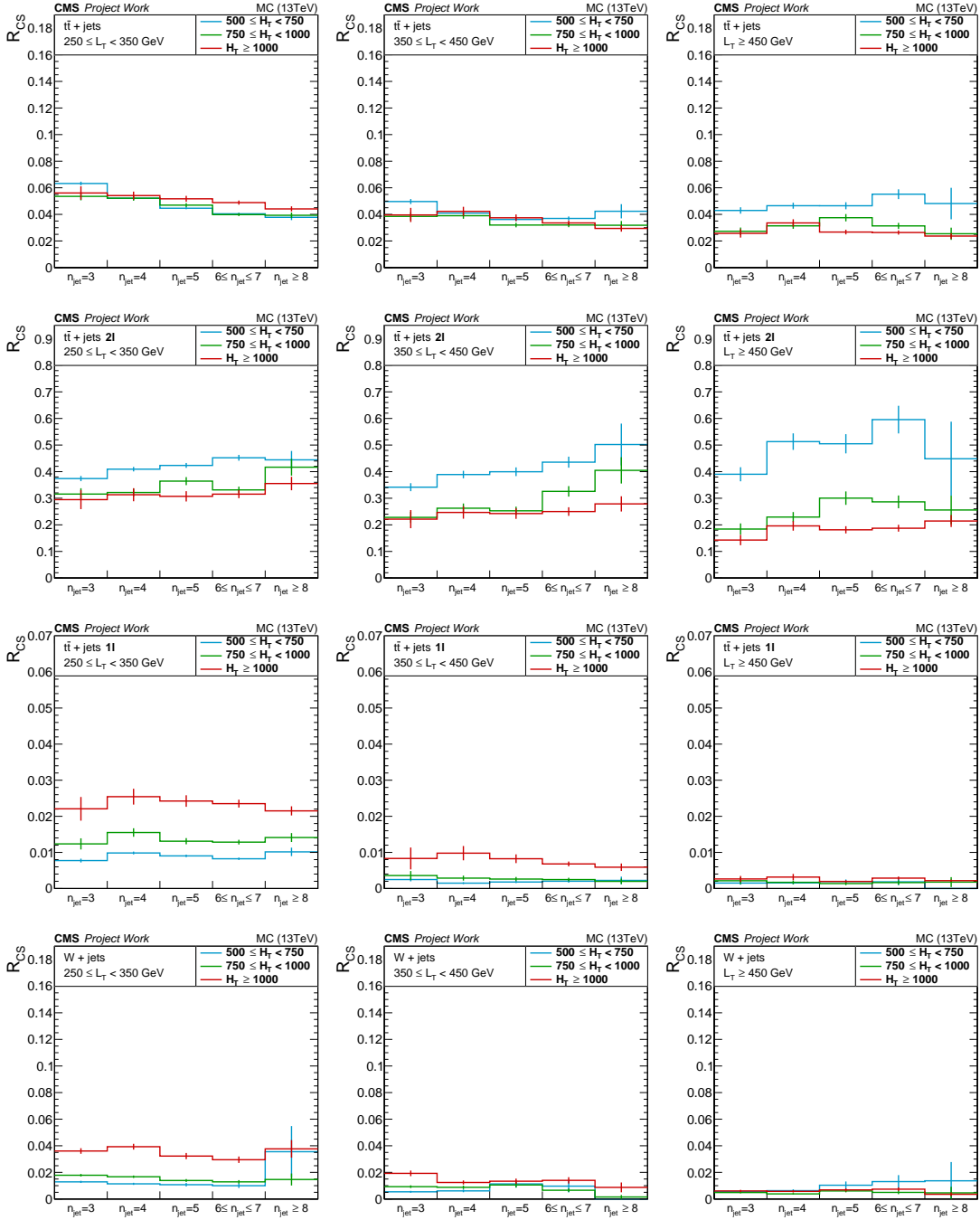


FIGURE 5.16:  $R_{CS}$  values for  $t\bar{t}$  + jets and  $W$ +jets events in simulated samples for different jet multiplicities in all  $H_T$  and  $L_T$  bins. The first row shows the total  $R_{CS}$  of  $t\bar{t}$  + jets. It can be seen that  $R_{CS}$  is relatively independent of the jet multiplicity. In the second row  $R_{CS}$  of  $t\bar{t}$  + jets with two generated but only one reconstructed charged lepton is shown.  $R_{CS}$  takes on high values due to the additional  $\cancel{E}_T$  introduced by the second neutrino. The third row shows the low  $R_{CS}$  values of events with only one generated charged lepton as comparison. In the last row,  $R_{CS}$  for  $W$ +jets events is shown.

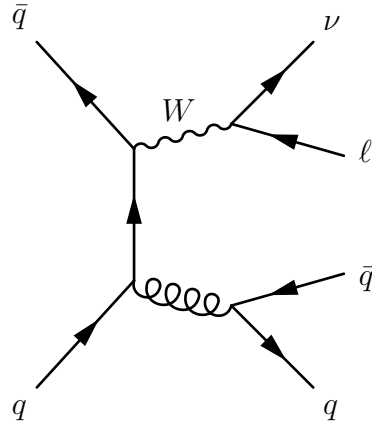


FIGURE 5.17: Diagram of a W+jets event where the W boson decays to a lepton and the corresponding neutrino. The gluon is resulting in jets, either arising from quarks or gluons.

$$R_{\text{CS}}^{\text{corr,data}}(0b, n_{\text{jet}} \in [3, 4]) = \frac{N_{\text{data}}^{\text{SR}} - R_{\text{CS}}^{t\bar{t},\text{MC}} \cdot f_{t\bar{t}} \cdot N_{\text{data}}^{\text{CR}}}{(1 - f_{t\bar{t}}) \cdot N_{\text{data}}^{\text{CR}}} . \quad (5.10)$$

Again, a correction factor extracted from simulation is used to account for residual dependence of  $R_{\text{CS}}$  on the jet multiplicity, which also covers differences between  $R_{\text{CS}}$  in muon only final states to muon or electron final states.

$$\kappa_W = \frac{R_{\text{CS}}^{\text{MC}}(0b, n_{\text{jet}}^{\text{SR}}, \text{W+jets})}{R_{\text{CS}}^{\text{corr,MC}}(0b, n_{\text{jet}} \in [3, 4], \mu)} . \quad (5.11)$$

The final  $R_{\text{CS}}$  value of W+jets events is then written as

$$R_{\text{CS}}^{\text{W}}(0b, n_{\text{jet}}^{\text{SR}}) = \kappa_W \cdot R_{\text{CS}}^{\text{corr}}(n_{\text{jet}} \in [3, 4]) . \quad (5.12)$$

$\kappa_W$  is again close to unity and values for all signal regions are shown in Tab. 5.5.

### 5.3.5 Other backgrounds

Other electroweak processes including single top quark production, Drell-Yan processes and top quark pair production in association with a vector boson can also mimic the signal, but their contribution is expected to be low. This is due to the either small production cross section or the small fraction of events in the single lepton final state. Top quark pair production with an associated W or Z boson has a small production cross section compared to the leading backgrounds. Drell Yan processes on the other

$n_{\text{jet}}$	$L_T$ [GeV]	$H_T$ [GeV]	$R_{\text{CS}}^{\text{corr.}}(3\text{-}4j, 0b, \mu)$	$R_{\text{CS}}(\text{SR}, 0b)$	$\kappa_W$ SR/SB
5	[250, 350]	$\geq 500$	0.0169 $\pm$ 0.0031	0.0146 $\pm$ 0.0009	0.86 $\pm$ 0.17
	[350, 450]	$\geq 500$	0.0084 $\pm$ 0.0036	0.0115 $\pm$ 0.0017	1.37 $\pm$ 0.63
	$\geq 450$	$\geq 500$	0.0059 $\pm$ 0.0025	0.0078 $\pm$ 0.0011	1.33 $\pm$ 0.6
[6, 7]	[250, 350]	[500, 750]	0.0133 $\pm$ 0.004	0.01 $\pm$ 0.0017	0.75 $\pm$ 0.26
		$\geq 750$	0.0259 $\pm$ 0.0046	0.0203 $\pm$ 0.0013	0.78 $\pm$ 0.15
	[350, 450]	[500, 750]	0.0061 $\pm$ 0.0046	0.0096 $\pm$ 0.0047	1.56 $\pm$ 1.4
		$\geq 750$	0.0133 $\pm$ 0.0056	0.0102 $\pm$ 0.0013	0.76 $\pm$ 0.33
	$\geq 450$	[500, 1000]	0.0094 $\pm$ 0.0033	0.0105 $\pm$ 0.0022	1.12 $\pm$ 0.46
		$\geq 1000$	0.0116 $\pm$ 0.0058	0.0112 $\pm$ 0.0017	0.96 $\pm$ 0.5
8 $\wedge$	[250, 350]	[500, 750]	0.0133 $\pm$ 0.004	0.0355 $\pm$ 0.0193	2.68 $\pm$ 1.66
		$\geq 750$	0.0259 $\pm$ 0.0046	0.029 $\pm$ 0.0044	1.12 $\pm$ 0.26
	[350, 450]	$\geq 500$	0.019 $\pm$ 0.0045	0.0189 $\pm$ 0.0044	0.99 $\pm$ 0.33
	$\geq 450$	$\geq 500$	0.0098 $\pm$ 0.0029	0.009 $\pm$ 0.003	0.92 $\pm$ 0.41

TABLE 5.5: Summary of  $R_{\text{CS}}$  values of W+jets events measured in simulation and the corresponding  $\kappa_W$  values.

hand have larger cross sections, but the final state either contains zero or two leptons. Due to the high acceptance of the detector and the high reconstruction efficiency of leptons, the fraction of events containing one lepton in the final state is small. Diagrams of these processes are shown in Fig. 5.18. The small estimated amount of these processes compared to the total background in the signal regions can be seen in Fig. 5.5. Therefore, yields of these processes in the signal regions are directly taken from simulations.

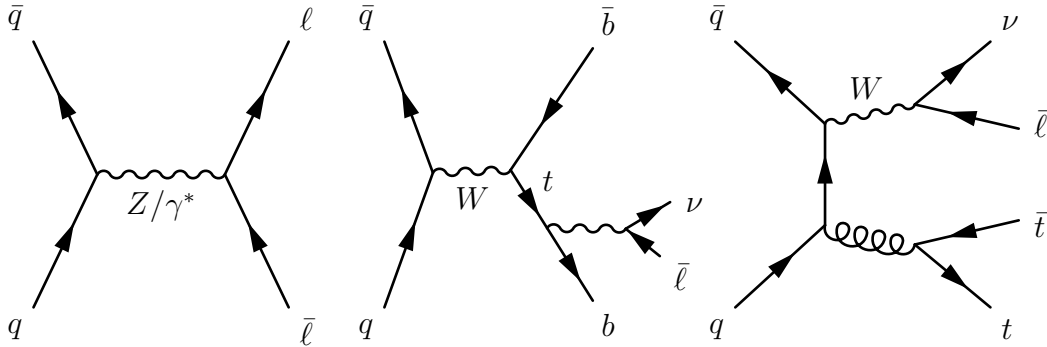


FIGURE 5.18: Diagrams of Drell-Yan process (left), single top quark production (center) and top quark pair production with associated vector boson (right).

## Chapter 6

# Systematic uncertainties and validation

### 6.1 $R_{CS}$ stability dependence on $\cancel{E}_T$ measurements

The data-driven background estimation of the W+jets background as described in Sec. 5.3.4 exploits the relative small dependence of  $R_{CS}$  on jet multiplicity. This independence can be spoiled if events with low generated  $L_T$  (those have large  $\Delta\phi(W, \ell)$ ) are promoted to high reconstructed  $L_T$  by large contributions of mismeasured  $\cancel{E}_T$ . The  $L_T$  dependence of  $\Delta\phi(W, \ell)$  is shown in Fig. 6.1. These effects can be studied in simulation, where it is possible to define a measure for so called fake  $\cancel{E}_T$ :

$$\cancel{E}_T^{fake} = | \vec{\cancel{E}}_T^{reco} - \vec{\cancel{E}}_T^{gen} | \quad (6.1)$$

which is the magnitude of the vectorial difference between the reconstructed and generated  $\cancel{E}_T$ . The generated  $\cancel{E}_T$  reflects the  $\cancel{E}_T$  coming from physical processes which ideally would equal the reconstructed one. Moreover,  $L_T^{\text{true}}$  is defined as the scalar sum of lepton  $p_T$  and generated  $\cancel{E}_T$  while  $L_T$  is the scalar sum of lepton  $p_T$  and reconstructed  $\cancel{E}_T$ . Results of this study performed in early simulated samples are shown in the following section.

The low jet multiplicity in the W+jets sideband regions together with the eventually tight  $H_T$  requirement selects events with pronounced jet  $p_T$  hierarchies since additional jets are counted starting at a low threshold of 30 GeV. These control samples are therefore easily biased by events with one (or two) more generated jets that either failed the reconstruction threshold completely or suffered from drastic  $p_T$  mismeasurement. These

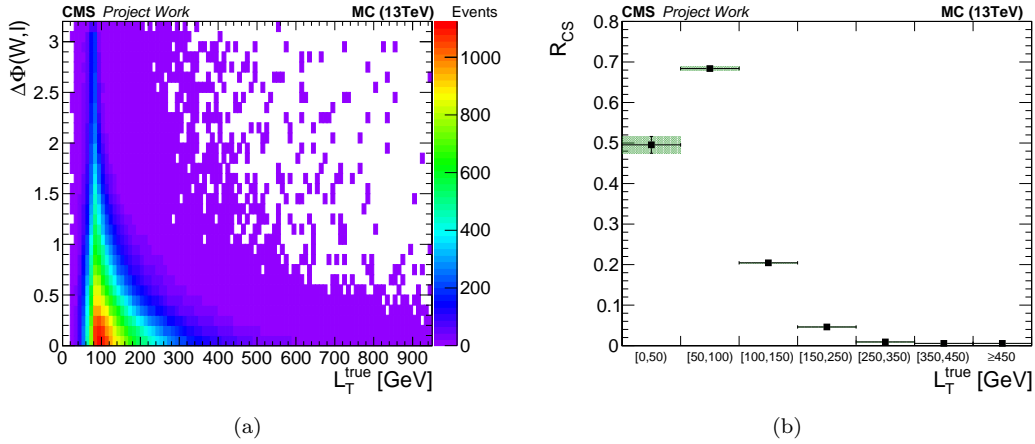


FIGURE 6.1: Left: Correlation between  $L_T$  and  $\Delta\phi(W, \ell)$ . Right:  $R_{CS}$  for increasing  $L_T^{\text{true}}$  values. Events with low  $L_T^{\text{true}}$  (below the baseline requirement of 250 GeV) tend to high  $\Delta\phi(W, \ell)$  values. Events originating from low  $L_T^{\text{true}}$  bins promoted to higher  $L_T$  bins therefore bias the  $R_{CS}$  measurement to higher values.

mismeasurements have several origins, e.g. fluctuations in the shower development, detector noise or pile-up. In more drastic cases, mismeasurements can be induced by dead cells of the electromagnetic calorimeters.

As a first check, Fig. 6.2a shows trends of  $R_{CS}$  values which are pronounced in the highest  $H_T$  bin where the effect described above is strongest. Figure 6.2b,c subdivide the event sample into two sub-sets according to a  $\cancel{E}_T^{\text{gen}}$  threshold of 100 GeV. It is readily seen, that the trend is induced by events with relatively low  $\cancel{E}_T^{\text{gen}}$ .

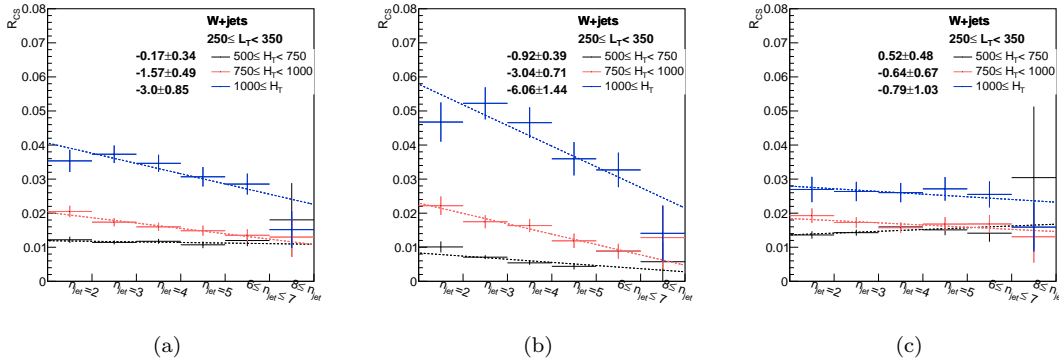


FIGURE 6.2:  $R_{CS}$  plots of  $250 < L_T < 350$  GeV bins. Left: Total bin without additional requirements. Middle: requiring  $\cancel{E}_T^{\text{gen}} < 100$  GeV. Right: requiring  $\cancel{E}_T^{\text{gen}} > 100$  GeV.

Next, it can be verified that large  $\cancel{E}_T^{\text{fake}}$  correlates with  $R_{CS}$  mismeasurement. Figure 6.3a shows a control region scatter plot that is colored according to  $\Delta\phi(W, \ell)$ . A large population of events with low  $L_T^{\text{true}}$  and high  $\Delta\phi(W, \ell)$  is visible in the bottom right area. Fig. 6.3b shows the events which pass the  $\Delta\phi(W, \ell) > 1$  requirement. Most



of these events would fail the baseline selection if  $L_T^{\text{true}}$  would be used, however, the large  $\cancel{E}_T^{\text{fake}}$  promotes them to relatively high  $L_T$ . In numbers, only 20% of events in the bin with  $250 < L_T < 350$  GeV,  $H_T > 1000$  GeV and 3 jets which have  $\Delta\phi(W, \ell) > 1$  originate from a  $L_T^{\text{true}}$  event satisfying the requirement, while 78% have  $L_T^{\text{true}} < 250$  GeV. Bins with higher jet multiplicity allow a more relaxed jet hierarchy and are therefore less exposed to feed-down from even higher jet multiplicities. This is the case for the bin requiring  $350 < L_T < 450$  GeV,  $750 < H_T < 1000$  GeV and 5 jets, which is shown in Fig. 6.3c,d.

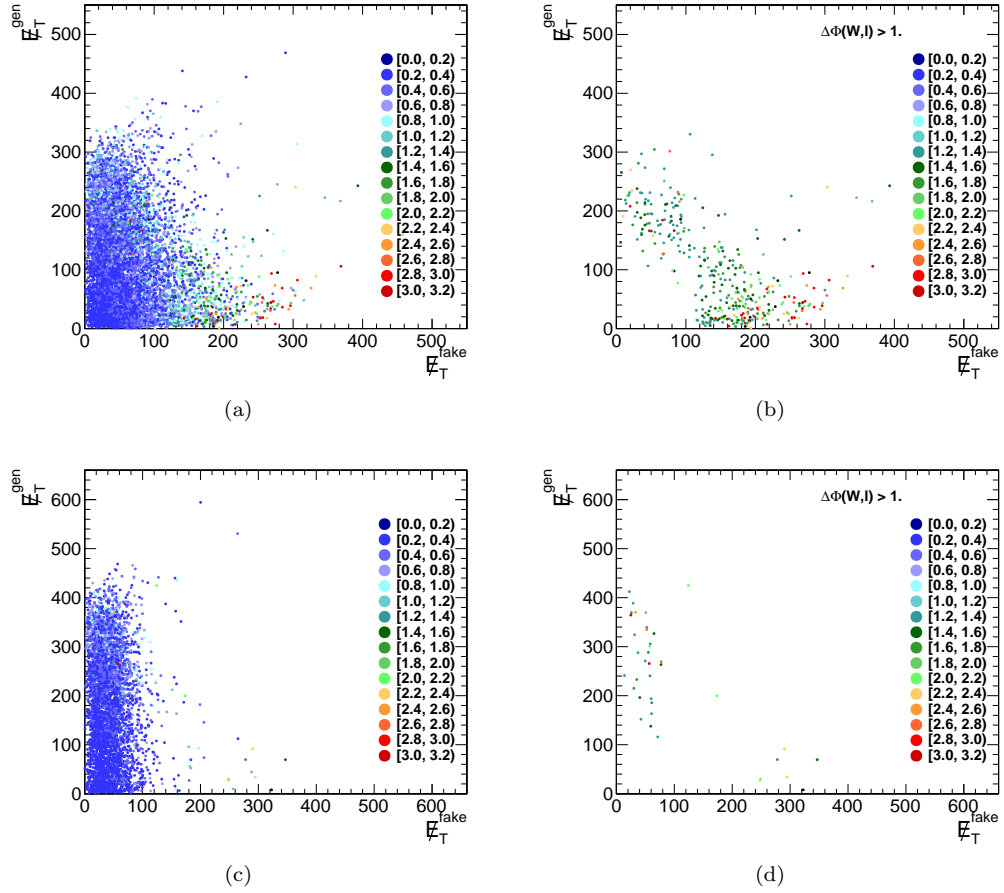


FIGURE 6.3: Scatter plots of W+jets events colored with respect to  $\Delta\phi(W, \ell)$ , plots on the right require  $\Delta\phi(W, \ell) > 1$ . Top:  $250 < L_T < 350$  GeV,  $H_T > 1000$  GeV and 3 jets. Bottom:  $350 < L_T < 450$  GeV,  $750 < H_T < 1000$  GeV and 5 jets.

In summary, the low jet multiplicity control region is prone to large  $\cancel{E}_T^{\text{fake}}$  from drastic jet mismeasurements, because a low jet multiplicity and high  $H_T$  imply a pronounced jet  $p_T$  hierarchy that can be satisfied by events where one or two jets are drastically mismeasured. Therefore, filters which remove events where jets overlay with a known dead cell of the ECAL are used. Enhanced jet energy calibrations and corrections also results in a reduction of events with such drastic jet  $p_T$  mismeasurements. To finally

confirm the hypothesis that events with low  $L_T^{\text{true}}$  (and therefore high  $\Delta\phi$ ) are promoted, four cases are compared. Figure 6.4(a) shows  $R_{CS}$  using  $\Delta\phi(W, \ell)$  calculated with reconstructed  $\cancel{E}_T$  and reconstructed  $\phi(\cancel{E}_T)$ , (b) with generated  $\cancel{E}_T$  and reconstructed  $\phi(\cancel{E}_T)$ , (c) with reconstructed  $\cancel{E}_T$  and generated  $\phi(\cancel{E}_T)$  and (d) with generated  $\cancel{E}_T$  and generated  $\phi(\cancel{E}_T)$ . These plots show that the largest effect indeed comes from the  $\cancel{E}_T$  mismeasurement.

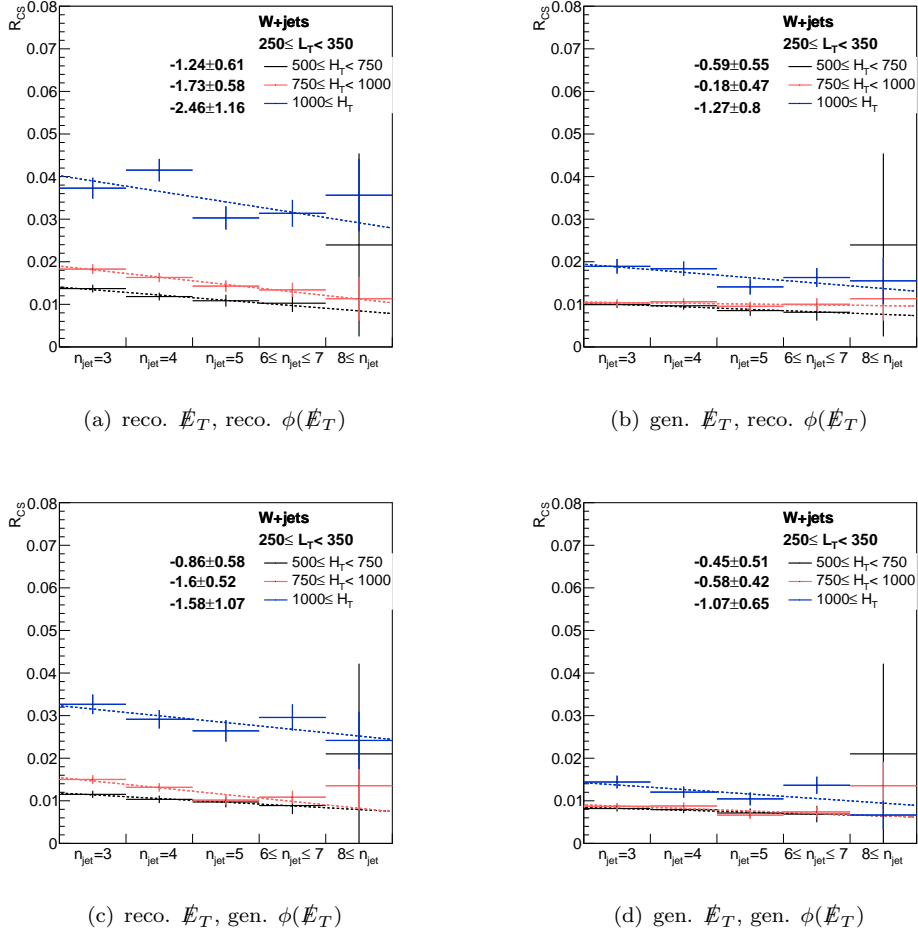


FIGURE 6.4:  $R_{CS}$  plots comparing reconstruction of W using the magnitude of  $\cancel{E}_T$  and  $\phi(\cancel{E}_T)$  on generator and reconstruction level.

To reduce the jet multiplicity dependence of  $R_{CS}$ , a standard requirement on the minimum angular separation of the leading  $n$  jets and  $\cancel{E}_T$ ,  $\min\Delta\phi(j_{1\dots n}, \cancel{E}_T)$  was studied. Such a cut traditionally vetoes QCD multijet events in hadronic SUSY searches. In the case at hand, it protects from drastic jet mismeasurements. Figure 6.5 shows  $\min\Delta\phi(j_{1\dots n}, \cancel{E}_T)$  for a different  $n$  considered. A cut on  $\min\Delta\phi(j_{1,2}, \cancel{E}_T) > 0.45$  is chosen.

The results of this study are shown in Fig. 6.6.  $R_{CS}$  values without corrections are shown in the first column. The plots in the center column use binning in  $L_T^{\text{true}}$  which

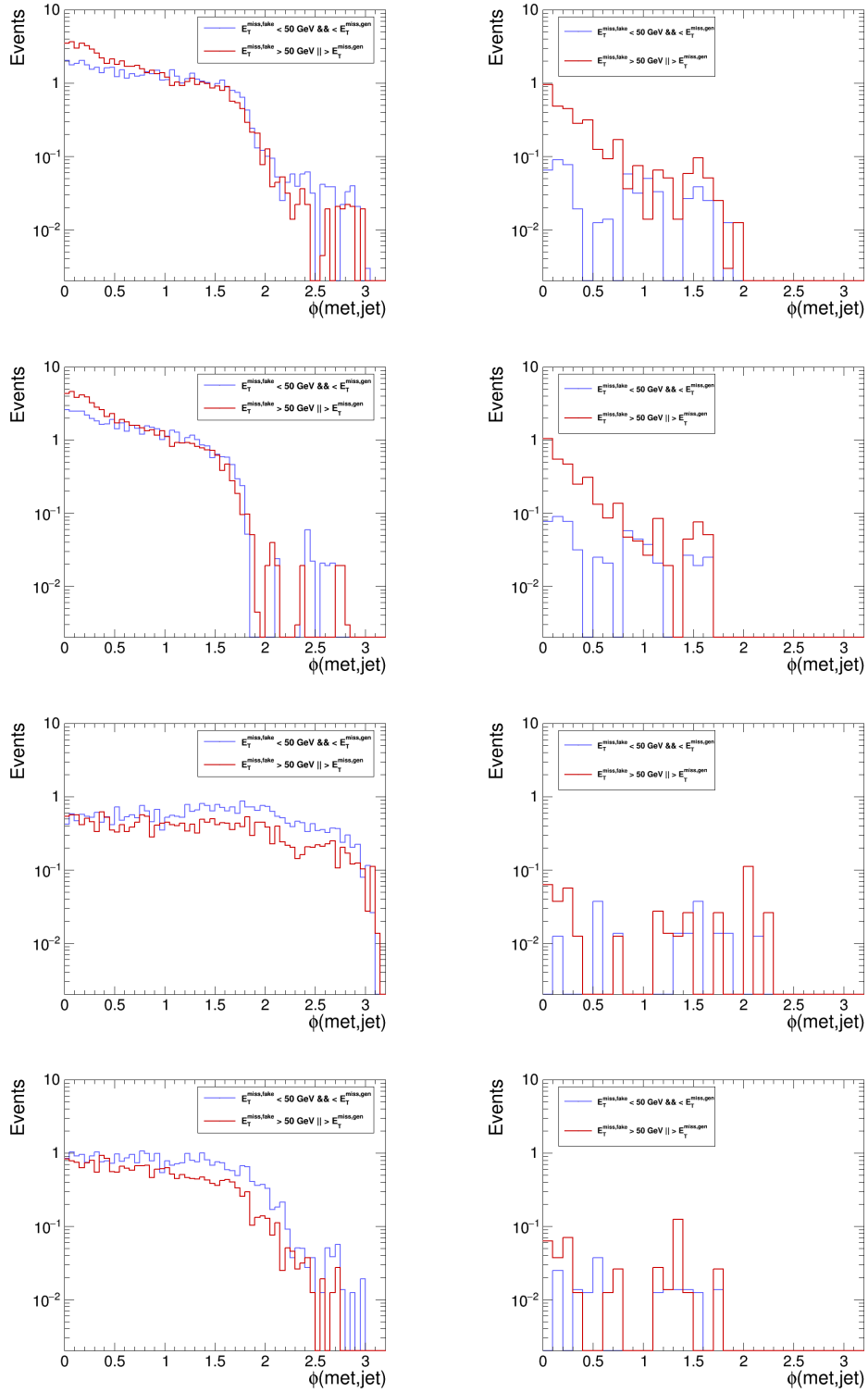


FIGURE 6.5: Minimum angular separation of jets and  $\cancel{E}_T$  for the  $n$  leading jets. Left: inclusive in  $\Delta\phi$  (W,l). Right:  $\Delta\phi$  (W,l) $>1$ . Top row:  $250 \text{ GeV} < L_T < 350 \text{ GeV}$ ,  $H_T > 1000 \text{ GeV}$ , 3 jets,  $\min\Delta\phi(j_{1,2,3}, \cancel{E}_T)$ . Second row: same bin,  $\min\Delta\phi(j_{1,2,3}, \cancel{E}_T)$ . Third row:  $350 \text{ GeV} < L_T < 450 \text{ GeV}$ ,  $750 < H_T < 1000 \text{ GeV}$ , 5 jets,  $\min\Delta\phi(j_{1,2}, \cancel{E}_T)$ . Last row: same bin,  $\min\Delta\phi(j_{1,2,3}, \cancel{E}_T)$ .

removes events with large  $\cancel{E}_T^{\text{fake}}$  and restores stability of  $R_{\text{CS}}$  for different jet multiplicities. Almost the same characteristics of  $R_{\text{CS}}$  are achieved when applying a  $\min\Delta\phi(j_{1,2},\cancel{E}_T) > 0.45$  cut which is shown in the right column. Including the third leading jet into the  $\min\Delta\phi(j_{1\dots n},\cancel{E}_T)$  requirement does not result in a significant improvement.

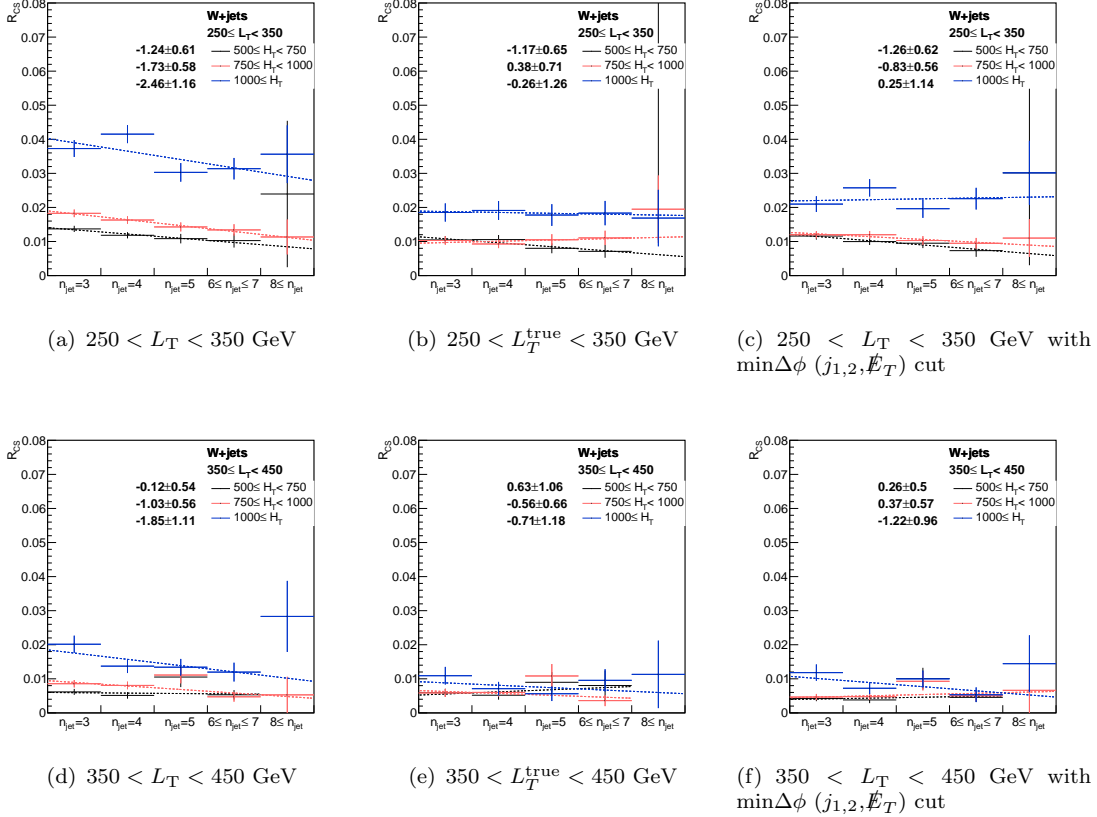


FIGURE 6.6:  $R_{\text{CS}}$  without corrections (left column), corrected at generator level by binning in  $L_T^{\text{true}}$  (middle column) and corrected at reconstruction level by applying the  $\min\Delta\phi(j_{1,2},\cancel{E}_T)$  cut (right column).

As a result of this study, the sideband region for measuring W+jets  $R_{\text{CS}}$  was moved from requiring 2-3 jets to 3-4 jets. This already relaxes the jet  $p_T$  hierarchy and therefore increases stability of  $R_{\text{CS}}$ . Additionally, events with suspicious  $\cancel{E}_T$  contributions are vetoed using filter algorithms. The steadily improved jet energy corrections further improved the stability, which makes the minimum requirement on  $\min\Delta\phi(j_{1,2},\cancel{E}_T)$  redundant.

## 6.2 QCD multijet events contamination in signal regions

The assumption of the negligible QCD multijets contribution in signal regions is built on the fact that these events have a narrow peak at zero in the  $\Delta\phi(W, \ell)$  distribution.

The rather weak statistical power of the simulated QCD multijet samples does not allow for significant statements. Single events at rather high  $\Delta\phi(W, \ell)$  values with relatively high event weights and 100% uncertainty eventually spoil the distribution. Therefore, a validation of the argument in a largely data driven way is developed.

$R_{CS}$  of QCD multijet events is measured in simulated samples. To obtain results with reasonable statistical uncertainties, measuring  $R_{CS}$  in all 13 signal regions with tight kinematic requirements is not applicable. Inclusive measurements in jet multiplicity,  $L_T$  and  $H_T$  are analyzed, which is shown in Fig. 6.7. First,  $L_T$  and  $H_T$  requirements are relaxed to the baseline requirements.  $R_{CS}$  values are then measured in jet multiplicity bins and a linear function is fitted. The fit result is compatible with a constant within one standard deviation (green band).  $R_{CS}$  values for high jet multiplicity nicely show the problem of lack of statistics of the QCD multijet samples in the tails of the kinematic distributions. Next,  $R_{CS}$  is measured in  $H_T$  bins while the jet multiplicity and  $L_T$  requirements are relaxed. Again, a fit is performed and the result again is compatible with constant within one standard deviation. Finally,  $R_{CS}$  is measured in  $L_T$  bins. Here a significant trend is observed, therefore it is not possible to determine one inclusive  $R_{CS}$  value for QCD multijet events for all signal regions. Three  $R_{CS}$  values in the  $L_T$  bins are measured.

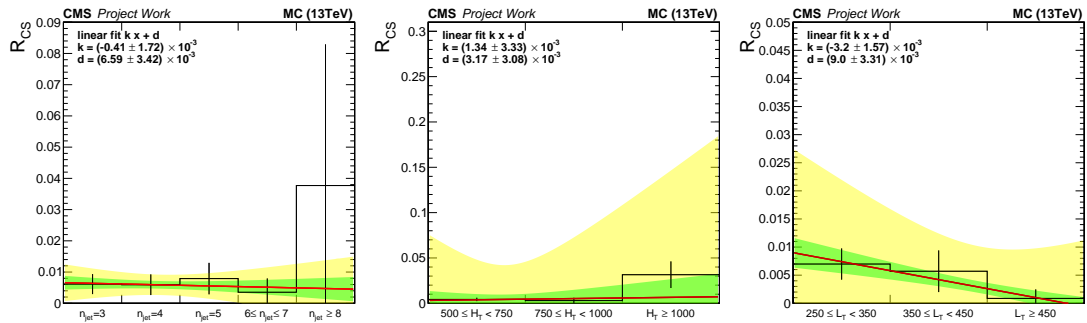


FIGURE 6.7:  $R_{CS}$  values for QCD multijet events after baseline requirements, binned in jet multiplicity (left),  $H_T$  (center) and  $L_T$  (right). The linear fit (red line) indicates that  $R_{CS}$  measurements for QCD multijet events can be made inclusively in jet multiplicity and  $H_T$ . The green and yellow band reflect one and two standard deviations around the fit result.

These  $R_{CS}$  values are then multiplied with the expected QCD multijet event yield obtained with the  $L_P$  method described in Sec. 5.3.2. An upper bound on the QCD multijet event yield in all signal regions is set which lies well below the 10% mark. Results for all 13 signal regions are shown in Tab. 6.1.

$n_{\text{jet}}$	$L_T$ [GeV]	$H_T$ [GeV]	Predicted background	yield	QCD multijets yield/pred.	$R_{CS}$
5	[250, 350]	$\geq 500$	12.8 $\pm$ 2.91	0.924 $\pm$ 0.347	0.07 $\pm$ 0.03	0.007 $\pm$ 0.0025
	[350, 450]	$\geq 500$	4.45 $\pm$ 2.15	0.32 $\pm$ 0.203	0.07 $\pm$ 0.05	0.0057 $\pm$ 0.0035
	$\geq 450$	$\geq 500$	3.89 $\pm$ 2.03	0.033 $\pm$ 0.016	0.01 $\pm$ 0.01	0.0009 $\pm$ 0.0004
[6, 7]	[250, 350]	[500, 750]	4.24 $\pm$ 1.37	0.318 $\pm$ 0.12	0.07 $\pm$ 0.03	0.007 $\pm$ 0.0025
		$\geq 750$	4.79 $\pm$ 1.6	0.187 $\pm$ 0.071	0.04 $\pm$ 0.02	0.007 $\pm$ 0.0025
	[350, 450]	[500, 750]	1.37 $\pm$ 1.12	0.073 $\pm$ 0.047	0.05 $\pm$ 0.04	0.0057 $\pm$ 0.0035
		$\geq 750$	1.29 $\pm$ 0.74	0.079 $\pm$ 0.05	0.06 $\pm$ 0.05	0.0057 $\pm$ 0.0035
	$\geq 450$	[500, 1000]	2.25 $\pm$ 0.93	0.013 $\pm$ 0.006	0.01 $\pm$ 0.0	0.0009 $\pm$ 0.0004
		$\geq 1000$	1.47 $\pm$ 1.04	0.005 $\pm$ 0.003	0.0 $\pm$ 0.0	0.0009 $\pm$ 0.0004
$\delta \wedge 1$	[250, 350]	[500, 750]	0.34 $\pm$ 0.22	0.013 $\pm$ 0.006	0.04 $\pm$ 0.02	0.007 $\pm$ 0.0025
		$\geq 750$	1.1 $\pm$ 0.61	0.031 $\pm$ 0.013	0.03 $\pm$ 0.01	0.007 $\pm$ 0.0025
	[350, 450]	$\geq 500$	0.45 $\pm$ 0.28	0.015 $\pm$ 0.01	0.03 $\pm$ 0.03	0.0059 $\pm$ 0.0035
	$\geq 450$	$\geq 500$	0.39 $\pm$ 0.26	0.001 $\pm$ 0.001	0.0 $\pm$ 0.0	0.0009 $\pm$ 0.0004

TABLE 6.1: Estimated upper limit of QCD multijets contamination in the signal regions,  $2.3\text{fb}^{-1}$ . The total predicted background, the estimated yield of QCD multijet events in signal regions and the ratio between them, as well as  $R_{CS}$  values are shown.

### 6.3 Systematic uncertainties

The data driven approach for predicting background event yields already covers for the potential mismodeling of the tails of kinematic distributions like  $L_T$ ,  $H_T$ ,  $\cancel{E}_T$  and  $\Delta\phi(W, \ell)$ . Still, several sources of discrepancies between simulated events and data that possibly influence the background prediction are probed. Additionally, systematic uncertainties of simulated signal events are studied.

#### 6.3.1 Background uncertainties

Systematic uncertainties of the predicted background in the signal regions are measured in simulated samples by varying existing or introducing new event weights. The change in closure is then measured as

$$\delta = \left( \frac{N'_{pred}}{N'_{sim}} \right) / \left( \frac{N_{pred}}{N_{sim}} \right) - 1 \quad (6.2)$$

where primed  $N$ s reflect the yields of predicted and simulated background events using varied weights, and unprimed  $N$ s the central values. In cases where the the simulated yield remains unchanged, this formula is reduced to

$$\delta = \frac{N'_{pred}}{N_{pred}} - 1 \quad (6.3)$$

### Cross sections

Cross sections of W+jets and  $t\bar{t}$  + jets events are varied by 30% independently. The impact of this variation is propagated through the background prediction, which leads to a total uncertainty in the range of 1 to 3%. For other background processes which are taken directly from simulation, a conservative 50% cross section uncertainty is used.

### W polarization

W polarization has a direct effect on the angular distributions and momentum spectra. Dependence of the background prediction on the polarization of W bosons in W+jets and  $t\bar{t}$  + jets events is covered by reweighing these events by

$$w = (1 \pm a \cdot (1 - \cos(\theta^*))) \cdot C \quad (6.4)$$

where  $a$  is either 5 or 10% for  $t\bar{t}$  + jets and W+jets events respectively,  $C$  is a factor to keep the overall normalization constant and  $\theta^*$  the angle between the charged lepton and the W boson in the W rest frame. This leads to a total uncertainty of below 3% in all the signal regions.

### Pile-up

The distribution of number of primary vertices differs between simulation and data. A weight can be calculated to match the two distributions. These weights have only a negligible effect on physical observables like  $L_T$ ,  $H_T$  and  $\Delta\phi(W, \ell)$  other than the number of primary vertices. Therefore, instead of using these calculated weights and therefore suffer from higher statistical uncertainties on simulated events, an uncertainty obtained from varying the inelastic cross section corresponding to 5% is assigned to cover for residual dependencies. The resulting uncertainty on the background prediction is below 10%.

### Jet energy corrections

Variations of jet energy corrections within the uncertainties, which impact the jet energy spectrum as well as  $\cancel{E}_T$ , are applied and propagated to the dependent variables. An uncertainty in the range of 1 to 8% is assigned.

### b-tag scale factors

The efficiency of the b-tagging algorithm differs between simulated samples and data. Scale factors are measured to correct for these differences. Uncertainties and variations of these scale factors impact the b-tag multiplicity distribution. These uncertainties cover for residual differences between the tagging efficiencies in simulation and data. The

b-tag multiplicity fit used to measure the background composition in control regions is sensitive to changes of the distribution of b-tagged jet multiplicity. Possible effects of variations on the background prediction are therefore examined by varying the scale factors within the uncertainties and calculating the change in closure. Changing the scale factors has a similar impact as changing the tagging efficiency

$$P_i = (SF_i \pm \sigma_{SF_i}) \cdot \epsilon_i \quad . \quad (6.5)$$

In a rough estimation, the efficiency of tagging jets from b- and c-hadrons is assumed to be fully correlated, while the mistag efficiency is assumed to be uncorrelated. Therefore, scale factors for these are varied simultaneously within the provided uncertainties, while the mistag scale factors are kept fixed. In Fig. 6.8 this is called *b/c tag efficiency*. The rate of light quark and gluon jets which get b-tagged is called *mistag efficiency*. These mistag efficiencies are then varied while keeping the b- and c-tag scale factors fixed.

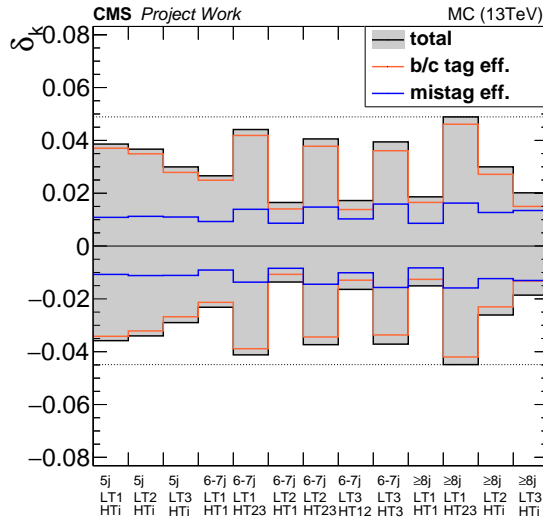


FIGURE 6.8: Change of the closure of the background prediction with varied b-tag scale factors.

The two variations are then combined. The total uncertainty accounts for about 2 to 5%.

### Reweighting of the top quark $p_T$

The  $p_T$  spectrum of top quarks is found to be softer in data than predicted by various simulations using leading-order (LO) or next-to-leading-order (NLO) event generators [74, 75]. Perturbative calculations at next-to-next-to-leading-order (NNLO) precision provide a good description of the top quark  $p_T$  spectrum [69]. To account for the



difference between the used LO  $t\bar{t}$  + jets events samples, a weight is applied:

$$w = \sqrt{SF(t) \cdot SF(\bar{t})} \quad \text{with} \quad (6.6)$$

$$SF(t) = e^{a+b \cdot p_T(t)} \quad (6.7)$$

The values for  $a$  and  $b$  are provided by the top quark physics group, with  $a = 0.156$  and  $b = -0.00137$ . The change in closure of the background prediction between applying and not applying the weight is assigned as uncertainty, which results in values below 7%.

### Dileptonic $t\bar{t}$ + jets events

The  $R_{CS}$  value of  $t\bar{t}$  + jets events is highly dependent on the fraction of events where both W bosons decay leptonically and one lepton is lost. This loss can be due to the lepton being out of acceptance, failing reconstruction or not passing the isolation requirements. A control sample with two leptons, where one of the leptons is removed and added as a jet instead, is used to measure  $n_{jet}$  distributions. Then, the ratio of data to simulation of both the single leptonic and dileptonic events is compared. A linear fit of the double ratio is then used to assign a systematic uncertainty of the potential mismodeling of the  $n_{jet}$  distribution in simulated samples. This is one of the main uncertainties, with values between 8 and 40%.

### $R_{CS}$ $n_{jet}$ dependence

$R_{CS}$  is measured in a low  $n_{jet}$  sideband and applied in regions with higher jet multiplicities. A linear fit is performed over the  $n_{jet}$  range to account for the possible residual dependence or minor other effects. The relative difference between the  $R_{CS}$  value measured in the sideband in simulated samples and the value extracted from the fit is taken as a systematic uncertainty. This procedure is applied for both  $t\bar{t}$  + jets and W+jets backgrounds independently. Fit results and  $R_{CS}$  values from simulation are shown in Fig. 6.9.

For  $t\bar{t}$  + jets, the uncertainty is in a range of 3 to 43%, while for W+jets it spans from 1 to 49%. If the two uncertainties are combined, the uncertainties account for 3 to 34%.

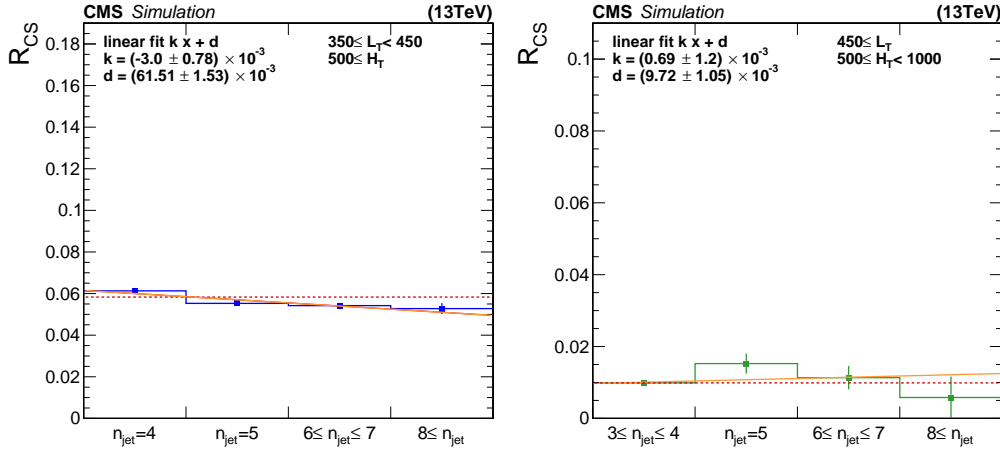


FIGURE 6.9:  $R_{CS}$  values obtained from simulation for  $t\bar{t} + \text{jets}$  (left) and  $W + \text{jets}$  (right). The orange line indicates the fitted first order polynomial, the dashed red line marks the  $R_{CS}$  value measured in the sideband in simulation. The difference between the linear fit and the constant in each bin is used as systematic uncertainty.

### $R_{CS}$ difference muon/(electron or muon)

Only events with a muon in the final state are used to determine  $R_{CS}$  for  $W + \text{jets}$ . To cover a possible inconsistency between this value and the true  $R_{CS}$  value the ratio between these two values measured in simulation is assigned as systematic uncertainty. If the statistical uncertainty of the true  $R_{CS}$  value is larger than the difference, that value is taken instead.

### QCD multijet prediction

QCD multijet predictions are used as input for determining  $R_{CS}$  of  $t\bar{t} + \text{jets}$  events and for measuring the background composition in control regions using a b-tag multiplicity fit. Therefore, the total background prediction is highly dependent on the magnitude of expected QCD multijet events. To cover for this dependency, QCD prediction yields are varied within the uncertainties and then used as inputs for the background prediction. The resulting change in closure of the total prediction is calculated and the resulting 1 to 3% are assigned as uncertainty.

### Lepton scale factors

Lepton identification algorithms have different efficiencies in simulated samples and observed data. The efficiencies are varied within the uncertainties and the 1% effect on the total background prediction is used as systematic uncertainty.

## Simulation statistics

Due to the limited number of simulated events, previously described  $\kappa$  correction factors have non-negligible statistical uncertainties, reflected in Tab. 5.4 and 5.5. These statistical uncertainties from simulation are treated as systematic uncertainties. These are propagated to the estimated values for  $W$ +jets and  $t\bar{t}$  + jets events independently.

## Luminosity

For backgrounds that are predicted in a data driven way, uncertainties on the luminosity cancel out. Therefore, no luminosity uncertainty has to be considered. For the event yields taken directly from simulation a flat 2.7% uncertainty over all signal regions is assigned [76].

The different systematic uncertainties on the background prediction in all 13 signal regions are shown in Fig. 6.10. The total systematic uncertainty is calculated as the squared sum of all the different sources. The total uncertainty on the background prediction shown in the lower band of the figure includes the systematic uncertainties described above as well as statistical uncertainties from data.

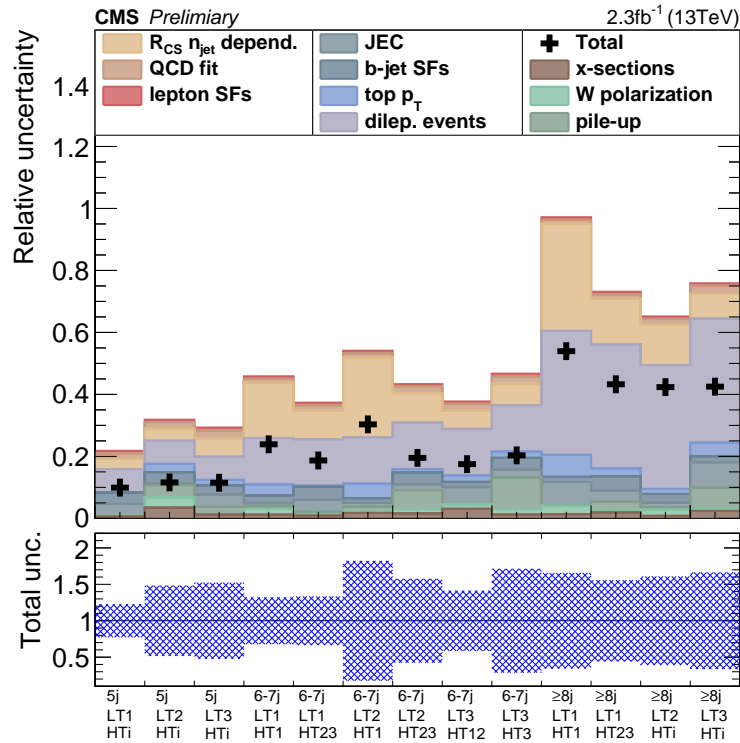


FIGURE 6.10: Visualization of all the systematic uncertainties in the signal regions introduced in Tab. 5.2 [71]. The various uncertainties are stacked linearly on top of each other, while the black crosses represent the square root of the square sum. The band on the bottom shows the total relative uncertainty, including statistical uncertainties.

### 6.3.2 Signal uncertainties

Contrary to simulated samples for background processes, a large variety of different signal samples is used because a scan over the unknown mass parameters of  $m_{\tilde{g}}$ ,  $m_{\tilde{\chi}_1^\pm}$  and  $m_{\tilde{\chi}_1^0}$  has to be performed. In this analysis, the value of  $m_{\tilde{\chi}_1^\pm}$  is set to the mid-point of  $m_{\tilde{g}}$  and  $m_{\tilde{\chi}_1^0}$ , which simplifies the scan to the  $m_{\tilde{g}} - m_{\tilde{\chi}_1^0}$  plane. To reduce the computational effort of the generation of multiple different samples, a faster simulation technique is used. While background samples are generated with a full simulation of the CMS detector using Geant4 [77], which implements several physics processes and is therefore computational expensive, signal samples are generated with FastSim, which parametrizes energy deposits and allows for faster calculations [78]. Computation time is reduced by a factor of 20, while the agreement between the two methods is in the percent level in the relevant observables used in this work. An exception are the efficiencies of the b-tagging and lepton identification algorithms, which differ between samples generated using the full simulation and FastSim. Scale factors are measured in control samples to correct for these differences, which are then applied on top of simulation to data scale factors. Variations within the provided uncertainties are used to determine systematic uncertainties on yields of signal events in the signal regions. A full list of used systematic uncertainties is given below.

#### Lepton scale factors

The lepton reconstruction efficiency differs between FastSim simulations and full detector simulations. The uncertainties on the measured scale factor are used to vary the event weight. Uncertainties are assigned corresponding to the relative change of the event yield in the signal regions.

#### Luminosity

A 2.7% uncertainty coming from the luminosity measurement is assigned for simulated signal samples [76].

#### Trigger

A flat 1% uncertainty is assigned due to possible trigger inefficiencies.

#### Scale uncertainty $Q^2$

Event per event weights are applied that vary the renormalization scale, the factorization scale and a correlated variation. The scale uncertainty is applied as a shape uncertainty. Therefore, the total normalization after the baseline selection has to be kept. Then, the variation of the yields in the signal regions is measured. The mean value of the maximum upwards and downwards variation of six different weights is used as uncertainty.

### Pile-up

The potential difference of pile-up between simulation and data is covered by a variation of the inelastic cross section. For signals, an average of 5% is assigned as uncertainty to all mass points and signal regions.

### b-tag scale factors

B-tag scale factors to correct simulation to data (similar to the scale factors used for background systematic uncertainties) and scale factors to account for differences in the detector simulation technique are applied on top of the b-tagging probability. Varied scale factors are used and the change of the yield in the signal region is measured. This change is then applied as systematic uncertainty.

### Initial/final state radiation

Initial and final state radiation (ISR/FSR) uncertainties account for a possible difference of the  $p_T$  spectrum in simulation and data. The  $p_T$  spectrum of the di-gluino system is reweighed and the change of the yield in the signal region is used as uncertainty. There is a small overlap with top  $p_T$  reweighing where the jet  $p_T$ s are treated individually.

### Jet energy corrections

Jet energy corrections are applied and varied for signal samples in a similar way as for background events.

Figure 6.11 shows all applied systematic uncertainties for one specific mass point of the T5q<sup>4</sup>WW model. Individual uncertainties for each mass point in the scanned  $m_{\tilde{g}} - m_{\tilde{\chi}_1^0}$  plane are assigned, which leads to sets of 576 uncertainties.

## 6.4 Validation of the background estimation

As a first check the closure of the prediction in pseudo-data to the simulated truth values is checked. Due to the implementation of  $\kappa$  correction factors perfect closure is reached by construction, which is shown in Fig. 6.12. The values of the correction factors are shown as well, together with a constructed  $\kappa$  factor for the total prediction. Although this factor is not used in the prediction method, it is a measure of the closure of the background prediction prior to the application of the residual corrections.

The background prediction method is validated with data in a four jet validation region where background events should be dominating due to low signal yields. The sideband for determining W+jets  $R_{CS}$  is restricted to contain events with exactly three jets to

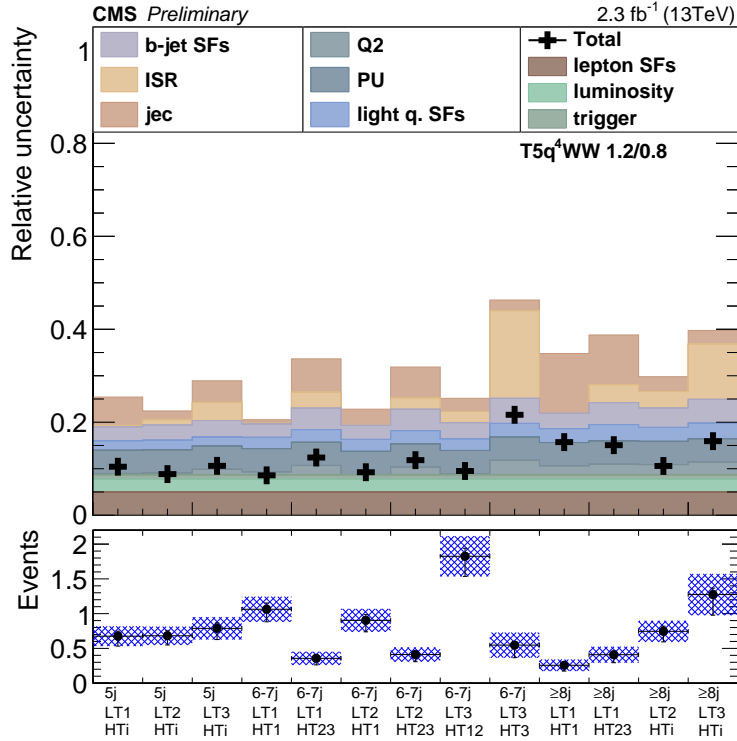


FIGURE 6.11: Visualization of all the systematic uncertainties in all 13 signal regions introduced in Tab. 5.2, for a signal mass point of  $m_{\tilde{g}} = 1200$  GeV,  $m_{\tilde{\chi}_1^\pm} = 1000$  GeV and  $m_{\tilde{\chi}_1^0} = 800$  GeV [71]. The various uncertainties are stacked linearly on top of each other, while the black crosses represent the square root of the square sum. The band on the bottom shows the expected yields for each signal region with the statistical uncertainty represented by the black line. The sum of statistical and systematic uncertainty are reflected by the blue dotted area.

avoid overlap with the validation region. The  $t\bar{t} + \text{jets}$  sideband can remain unchanged. The background yields for signal regions with four jets, zero b-tagged jets and different  $L_T$  and  $H_T$  requirements are then predicted using the method described above. The reduced event count in the W+jets sideband caused by the tight jet multiplicity requirement decreases the precision of the method. Therefore, statistical uncertainties are increased. Systematic uncertainties for the validation regions have not been calculated exactly, instead, rough estimates are used. Closure between predicted and observed yields is achieved as shown in Fig. 6.13.

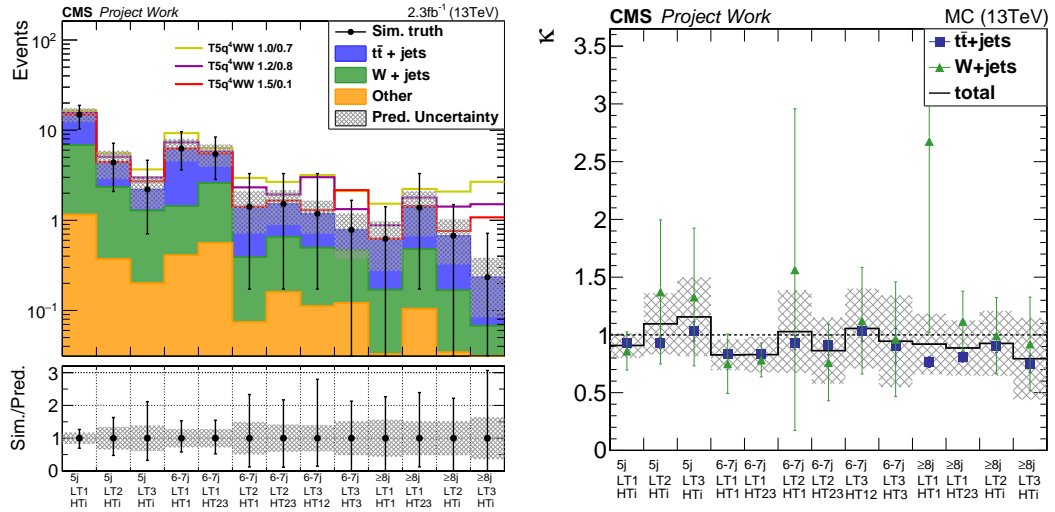


FIGURE 6.12: Closure of the background prediction in simulation (left). The black dots represent pseudo-data from simulation. The prediction perfectly agrees with the simulated truth by construction, which is shown in the lower band.  $\kappa$  correction factors for W+jets and  $t\bar{t}$  + jets events as well as for the total background are shown to the right. The total  $\kappa$  shows the closure prior the residual corrections. The shaded error reflects the uncertainty coming from limited simulation statistics.

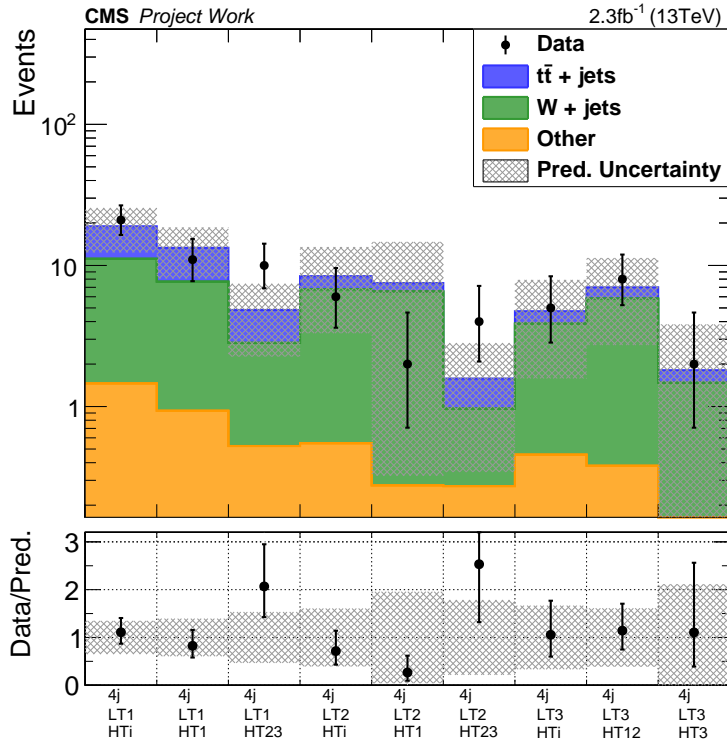


FIGURE 6.13: Predicted background against observed data in validation regions. Separate predictions for W+jets (green) and  $t\bar{t}$  + jets (blue) as well as residual other backgrounds (orange) are stacked on top of each other. Observed yields are shown in black, the shaded area reflects the combined statistical and systematic uncertainties. The lower panel shows the ratio of data to predicted background.





## Chapter 7

# Results with first data of Run 2

The number of observed events in the 13 signal regions is compared to the predicted number of SM background events. These expected numbers are shown with all statistical and systematic uncertainties listed in Sec. 6.3 in Fig. 7.1 and Tab. 7.1. Expected numbers of signal events from simulation for three benchmark mass points are given with uncertainties. The actual observation is shown in the rightmost column. No significant excess over the SM prediction is observed, with the largest deviation being close to one standard deviation. Therefore, the expectations from the SM very well describe the observed data. In general, more downwards than upwards fluctuations are observed, meaning that less events have been observed than were predicted. If all signal regions are combined,  $38.8 \pm 15.0$  events are predicted while  $35.0 \pm 5.9$  events observed, hence measured data is in good agreement with expectations from the SM.

$n_{\text{jet}}$	$L_T$ [GeV]	$H_T$ [GeV]	Bin name	Expected signal T5q <sup>4</sup> WW $m_{gl}/m_{\tilde{\chi}^0}$ [TeV]			Predicted background	Observed
				1.0/0.7	1.2/0.8	1.5/0.1		
5	[250, 350]	$\geq 500$	LT1, HTi	1.67 $\pm$ 0.27	0.68 $\pm$ 0.07	0.03 $\pm$ 0.01	12.8 $\pm$ 2.91	13
	[350, 450]	$\geq 500$	LT2, HTi	1.13 $\pm$ 0.22	0.68 $\pm$ 0.07	0.04 $\pm$ 0.01	4.45 $\pm$ 2.15	4
	$\geq 450$	$\geq 500$	LT3, HTi	1.48 $\pm$ 0.26	0.79 $\pm$ 0.08	0.51 $\pm$ 0.02	3.89 $\pm$ 2.03	1
6, 7	[250, 350]	[500, 750]	LT1, HT1	3.03 $\pm$ 0.36	1.06 $\pm$ 0.09	0.0 $\pm$ 0.0	4.24 $\pm$ 1.37	8
		$\geq 750$	LT1, HT23	0.92 $\pm$ 0.2	0.36 $\pm$ 0.05	0.08 $\pm$ 0.01	4.79 $\pm$ 1.6	4
	[350, 450]	[500, 750]	LT2, HT1	1.54 $\pm$ 0.26	0.9 $\pm$ 0.08	0.0 $\pm$ 0.0	1.37 $\pm$ 1.12	0
		$\geq 750$	LT2, HT23	1.15 $\pm$ 0.21	0.41 $\pm$ 0.05	0.13 $\pm$ 0.01	1.29 $\pm$ 0.74	2
	$\geq 450$	[500, 1000]	LT3, HT12	1.99 $\pm$ 0.29	1.83 $\pm$ 0.12	0.11 $\pm$ 0.01	2.25 $\pm$ 0.93	0
		$\geq 1000$	LT3, HT3	1.33 $\pm$ 0.23	0.55 $\pm$ 0.06	1.38 $\pm$ 0.04	1.47 $\pm$ 1.04	2
$\geq 8$	[250, 350]	[500, 750]	LT1, HT1	0.9 $\pm$ 0.2	0.26 $\pm$ 0.04	0.0 $\pm$ 0.0	0.34 $\pm$ 0.22	0
		$\geq 750$	LT1, HT23	0.85 $\pm$ 0.19	0.41 $\pm$ 0.05	0.06 $\pm$ 0.01	1.1 $\pm$ 0.61	1
	[350, 450]	$\geq 500$	LT2, HTi	1.41 $\pm$ 0.23	0.75 $\pm$ 0.07	0.09 $\pm$ 0.01	0.45 $\pm$ 0.28	0
	$\geq 450$	$\geq 500$	LT3, HTi	2.44 $\pm$ 0.31	1.27 $\pm$ 0.09	0.84 $\pm$ 0.03	0.39 $\pm$ 0.26	0

TABLE 7.1: Predicted background, expected signal and observed event yields in the 13 signal regions, corresponding to  $2.3\text{fb}^{-1}$ . All statistic and systematic uncertainties are reflected in the numbers shown.

A direct comparison of data with simulation using the  $\Delta\phi(W, \ell)$  variable is shown in Fig. 7.2. The baseline selection of  $L_T$  above 250 GeV,  $H_T$  above 500 GeV and at least

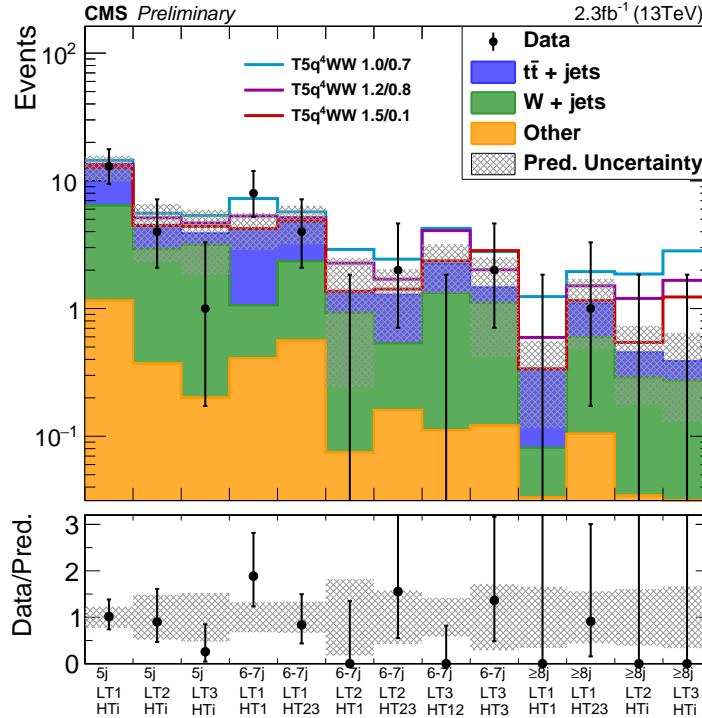


FIGURE 7.1: Measured data and predicted SM background in the 13 search bins introduced in Tab. 5.2 [71]. Separate predictions for W+jets (green) and  $t\bar{t}$  + jets (blue) as well as residual other backgrounds (orange) are stacked on top of each other. Data yields are shown in black, the shaded area reflects the combined statistical and systematic uncertainties. The lower panel shows the ratio of data to predicted background. Predicted yields of three benchmark SUSY models with different  $m_{\tilde{g}}$  and  $m_{\tilde{\chi}_1^0}$  in TeV are shown in cyan, magenta and red.

5 jets are required. In this comparison, no systematic uncertainties are shown. Again, good agreement is observed, whereas a higher event count in the tail of the distribution should be observed if one of the signal hypotheses was true.

A potential SUSY event using the CMS event display software [79] is shown in Fig. 7.3. It shows an event with one muon passing the selection criteria and six jets with  $p_T$  above 30 GeV.

## 7.1 Limits

The good agreement between SM prediction and observation allows to set limits on the T5q<sup>4</sup>WW model. The limits are calculated for chargino masses half way between the gluino and neutralino masses,  $m_{\tilde{\chi}_1^\pm} = (m_{\tilde{g}} - m_{\tilde{\chi}_1^0})/2$ . The two separate  $R_{CS}$  methods for the two leading backgrounds described in Sec. 5 can be treated individually as so called ABCD methods. An ABCD method consists of four exclusive regions, and the following notation is used: The signal region in the mainband is denoted as A. Region

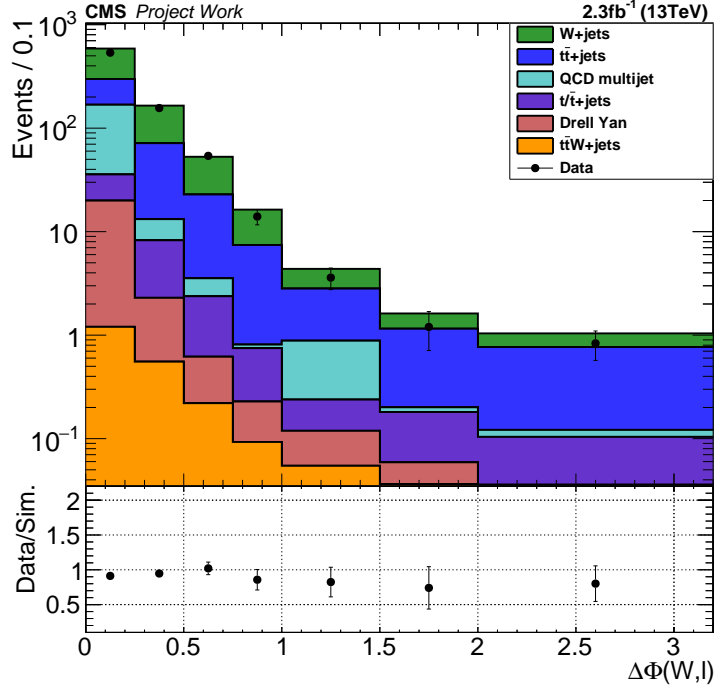


FIGURE 7.2: Comparison of observed data with SM simulation. Simulation distributions are scaled to  $2.3\text{fb}^{-1}$ . The lower panel shows the ratio of data to simulated background. Good agreement is observed.

B is equivalent to the control region in the mainband, fractions  $f_W$  and  $f_{t\bar{t}}$  are obtained from the b-tag multiplicity fit. C and D as well as E and F describe the sideband regions for W+jets and  $t\bar{t}$ +jets, respectively. This leads to a formulation of the total expectation in region A as:

$$A = \kappa_W \times R_{CS}^W \times N_{CR}^W + \kappa_{t\bar{t}} \times \kappa_W \times R_{CS}^{t\bar{t}} \times N_{CR}^{t\bar{t}} + N_{SR,MC}^{\text{other}} \quad (7.1)$$

$$= \kappa_W \times \frac{C - C_{t\bar{t}}}{D - D_{t\bar{t}}} \times f_W \times B + \kappa_{t\bar{t}} \times \kappa_W \times \frac{E - E_{QCD}}{F - F_{QCD}} \times f_{t\bar{t}} \times B + N_{SR,MC}^{\text{other}} \quad (7.2)$$

The procedure for calculating exclusion limits in the gluino - neutralino mass plane is based on the modified frequentistic method [80]. The likelihood function is using observed yields in the different regions with expected yields and  $\kappa$  factors serving as nuisance parameters.

$$\mathcal{L}(\text{data}|\mu, \theta) = \prod_i^{ABCDEF} \text{Poisson}(\text{data}|b_i(\theta) + \mu \cdot s_i(\theta)) \times \prod_j^{\text{nuisances}} \text{Constraints}(\tilde{\theta}_j|\theta_j) \quad (7.3)$$

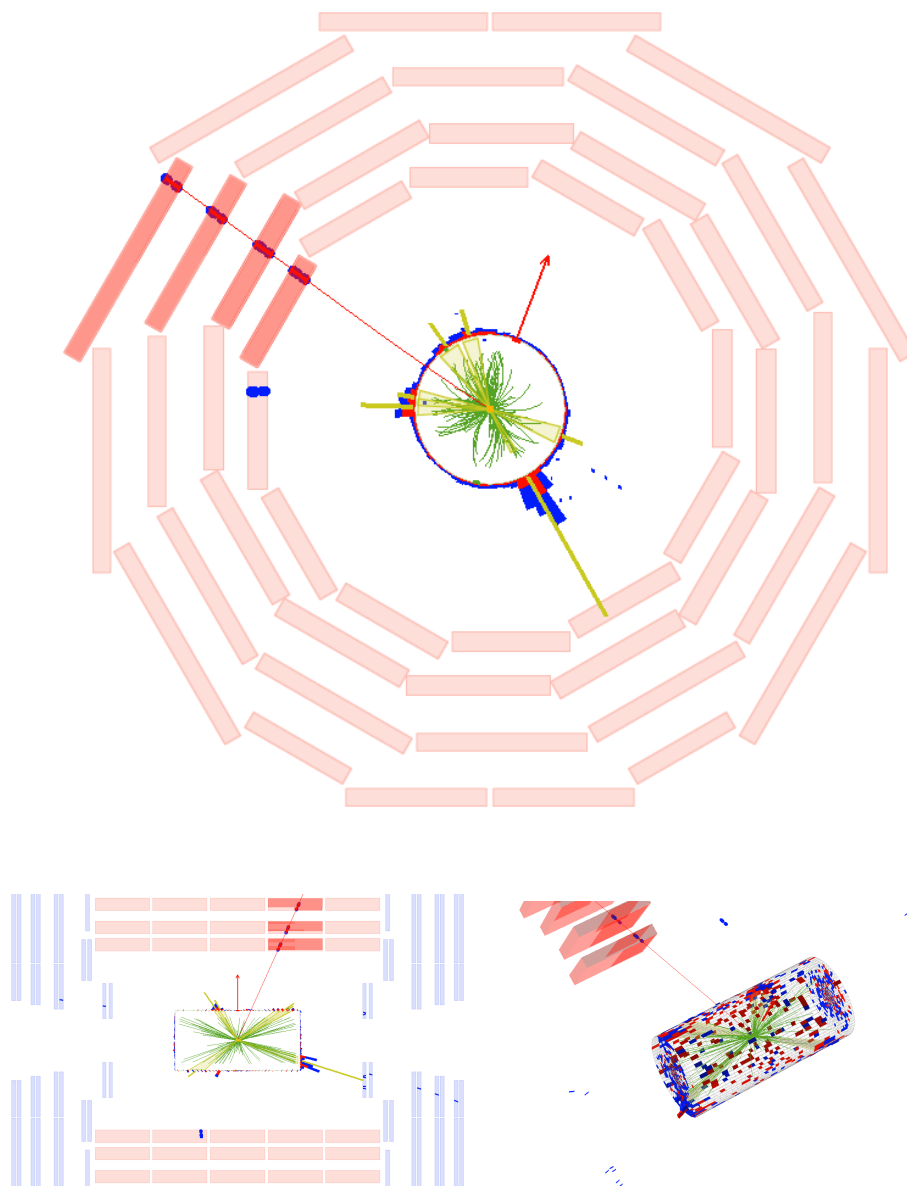


FIGURE 7.3: SUSY candidate event with a single muon (red line) and six jets (yellow towers). The direction of  $\cancel{E}_T$  is marked with a red arrow. The top plot shows the transverse ( $r$ - $\phi$ ) plane, the lower left plot the  $r$ - $\eta$  plane. A 3D tower view is shown in the lower right figure.

In this equation, *data* represents either the actual observation or simulated pseudo-data,  $b$  and  $s$  the expected background and signal yields, and  $\mu$  denotes the signal strength. The poissonian nature of data counts in all bins  $i$  is taken into account in the first part of the equation:

$$\text{Poisson}(data|b_i(\theta) + \mu \cdot s_i(\theta)) = \frac{(\mu s_i + b_i)^{n_i}}{n_i!} e^{-\mu s_i - b_i} \quad (7.4)$$

where  $n_i$  corresponds to the number of observed events in bin  $i$ . Constraints coming from systematic uncertainties are assumed to be logarithmic normal distributed and are treated as correlated between the different search bins. Correction factors  $\kappa$  coming from simulation are included as Gaussian distributed constraints. Expected QCD multijet event yields and other corrections applied to the observed yields in the sideband regions are treated as log normal distributed constraints.

Potential signal contamination in sideband and control regions are considered as well.

The measurement of the relative fractions of  $W$ +jets and  $t\bar{t}$  + jets events by using a b-tag multiplicity fit introduces an anticorrelation between these two numbers. This is modeled by introducing a parameter linking these two fractions.

The test statistic is defined using a profile likelihood ratio in the asymptotic limit [81]:

$$\tilde{q}_\mu = -2 \ln \frac{\mathcal{L}(\text{data}|\mu, \hat{\theta}_\mu)}{\mathcal{L}(\text{data}|\hat{\mu}, \hat{\theta})} \quad (7.5)$$

The denominator shows the global maximum of the likelihood, given by  $\hat{\mu}$  and  $\hat{\theta}$ . For a non-negative signal and one-sided limits the constraints on the signal strength modifier  $0 \leq \hat{\mu} \leq \mu$  apply. Besides providing one sided limits, the condition of  $\hat{\mu} \leq \mu$  also provides that interpretation in cases where  $\mu > \hat{\mu}$  does not lead to disfavoring the signal hypothesis. In general, observations with  $\tilde{q}_\mu > 0$  are more likely under the background hypothesis. For nuisances or systematic uncertainties, probability density functions (pdfs)  $\rho(\theta|\tilde{\theta})$  can be interpreted in a Bayesian way as posteriors arising from (fictional) measurements  $\tilde{\theta}$

$$\rho(\theta|\tilde{\theta}) \sim p(\tilde{\theta}|\theta) \cdot \pi_\theta(\theta) \quad (7.6)$$

with a flat prior  $\pi_\theta(\theta)$  [82]. This allows a representation of nuisances in a frequentistic way: Using these pdfs as a Bayesian posterior, one can utilize  $p(\tilde{\theta}|\theta)$  for constraining the likelihood function in a frequentistic manner. Moreover, it is then possible to build sampling distributions out of the pdf  $p(\tilde{\theta}|\theta)$  of the (fictional) measurements. This supersedes the computational costly process of conducting multiple toy experiments.

One then computes the observed value of  $\tilde{q}_\mu^{obs}$  for a given signal strength  $\mu$  as well as the values of the nuisance parameters  $\hat{\theta}_0^{obs}$  (background only hypothesis) and  $\hat{\theta}_\mu^{obs}$  (signal+background hypothesis) that maximize the likelihood in Eq. 7.3. Pdfs for the test statistics of the null and alternative hypothesis  $f(\tilde{q}_\mu|\mu, \hat{\theta}_0^{obs})$  and  $f(\tilde{q}_\mu|\mu, \hat{\theta}_\mu^{obs})$  are

generated using Monte Carlo simulations. Fixing the nuisances to the conditional maximum likelihood estimate which is called profile construction provides good coverage [83]. Then, one can calculate the p-values of the actual observation

$$p_\mu = P(\tilde{q}_\mu \geq \tilde{q}_\mu^{obs} | \text{signal+background}) = \int_{\tilde{q}_\mu^{obs}}^{\infty} f(\tilde{q}_\mu | \mu, \hat{\theta}_\mu^{obs}) d\tilde{q}_\mu \quad (7.7)$$

$$1 - p_b = P(\tilde{q}_\mu \geq \tilde{q}_\mu^{obs} | \text{background}) = \int_{\tilde{q}_\mu^{obs}}^{\infty} f(\tilde{q}_\mu | 0, \hat{\theta}_0^{obs}) d\tilde{q}_\mu \quad (7.8)$$

and use the results to obtain

$$CL_s(\mu) = \frac{p_\mu}{1 - p_b} . \quad (7.9)$$

Signals can be excluded with a confidence level of  $(1 - \alpha)$  for a given signal strength  $\mu$  if  $CL_s \leq \alpha$ . For the following results,  $\mu$  is varied until  $CL_s = 0.05$  is reached, which corresponds to a 95% confidence level. If the signal strength  $\mu$  is smaller than 1, a signal mass point is excluded.

The limits are obtained as combination of all the 13 search bins [84]. The final cross section limits obtained by the above described fully frequentistic method are shown in Fig. 7.4. The red dashed line represents the expected limit which corresponds to the expected background. Due to the downward fluctuations in the most sensitive bins the observed limit (black line) exceeds the expectation.

The color map represents the product of cross section and branching ratio  $\sigma \times \mathcal{B}^2$ . A branching ratio of 100% for the gluino cascade decay is assumed in this simplified model.

Different search bins show different sensitivity to the variety of mass points. Figure 7.5 shows the most sensitive bin for each mass point. The different sensitivity for different mass points explains the varying distance between expected and observed limit: While the zero observations in the most sensitive bins for masses around (1400,800) GeV push the limit further up, the most sensitive bins around (1400,0) are closer to the expectation. Therefore, the observed limit is closer to the expected one.

## 7.2 Comparison with other results

Comparing the obtained limits with searches from both the ATLAS and CMS collaboration in the previous run of LHC with a center of mass energy of 8 TeV [65, 85], the

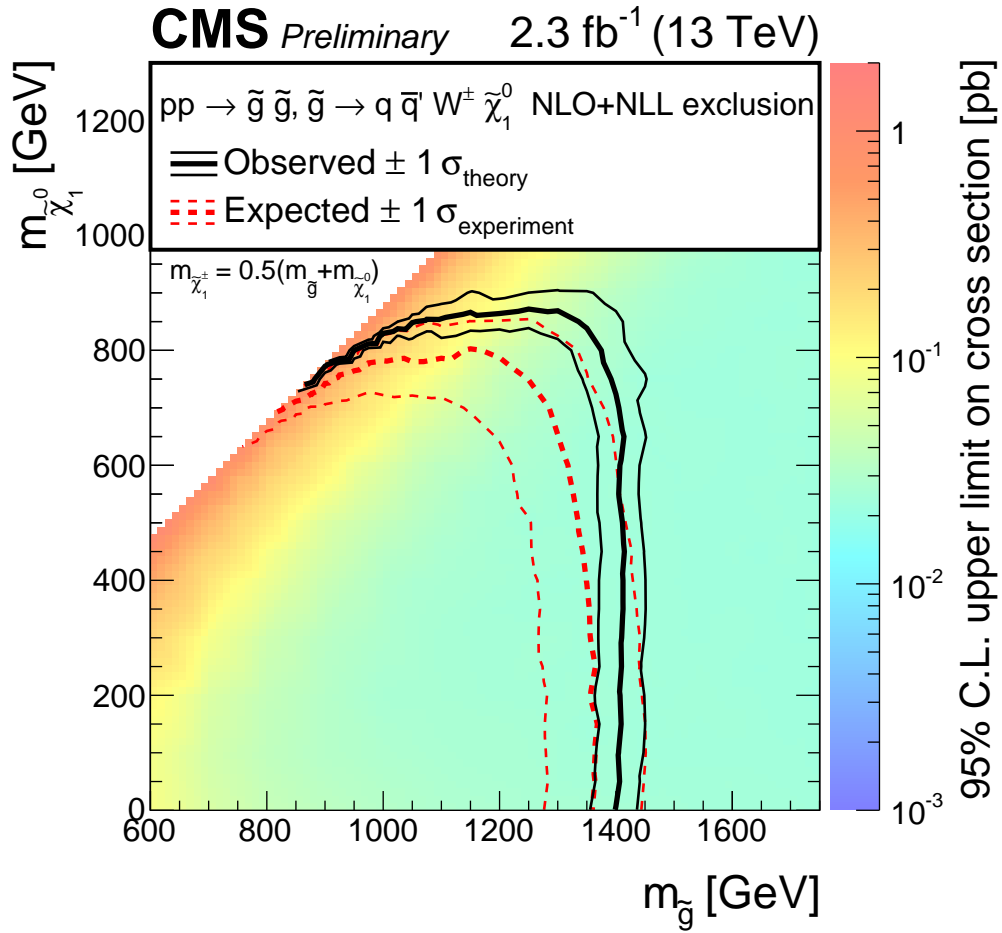


FIGURE 7.4: 95% CL cross section limits for the T5qqqWW model [71]. The observed and expected contours are shown in black and red, respectively.

observed limits on gluino and neutralino masses are improved by 150 (500) GeV and 150 (250) GeV, respectively. Two searches conducted by the ATLAS collaboration using data from the 2015 LHC run were also sensitive to the T5q<sup>4</sup>WW signal model [86, 87]. No significant excess was observed in these analyses. Obtained limits exclude gluinos up to 1600 GeV for low neutralino masses, extending the limits of this analysis by 200 GeV. However, in more compressed scenarios where gluino, chargino and neutralino masses are closer to each other, this analysis can significantly extend exclusion limits.

Three searches within the CMS collaboration using 13 TeV data from 2015 also targeted the same or similar models [88–90]. Models with Z and/or W bosons coming from the cascade decay of the gluino instead of W bosons only are also well motivated in theory. Limits set by this analysis are again very competitive, although a direct comparison with the above mentioned models is challenging. A combined plot for excluded mass points in the gluino-neutralino mass plane is shown in Fig. 7.6, which was presented at the *Moriond 2016* conference.

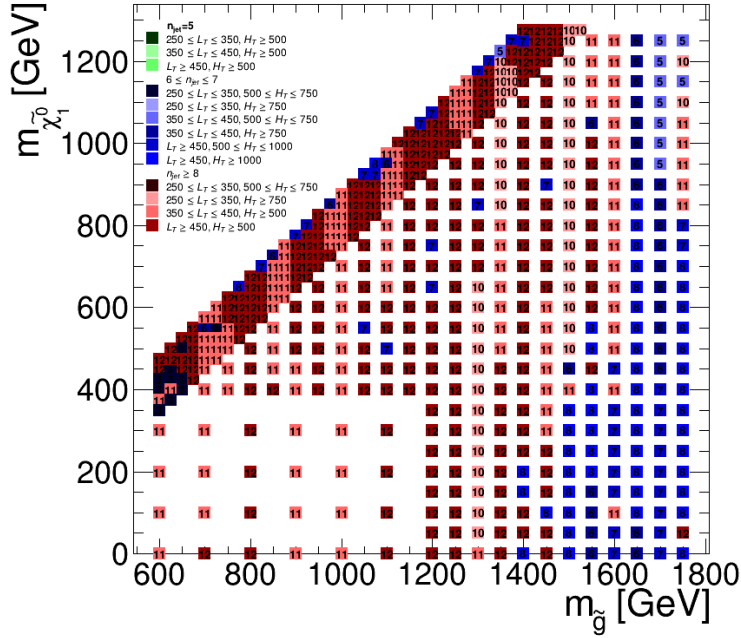


FIGURE 7.5: Most sensitive bin for each of the simulated mass points used for setting exclusion limits.

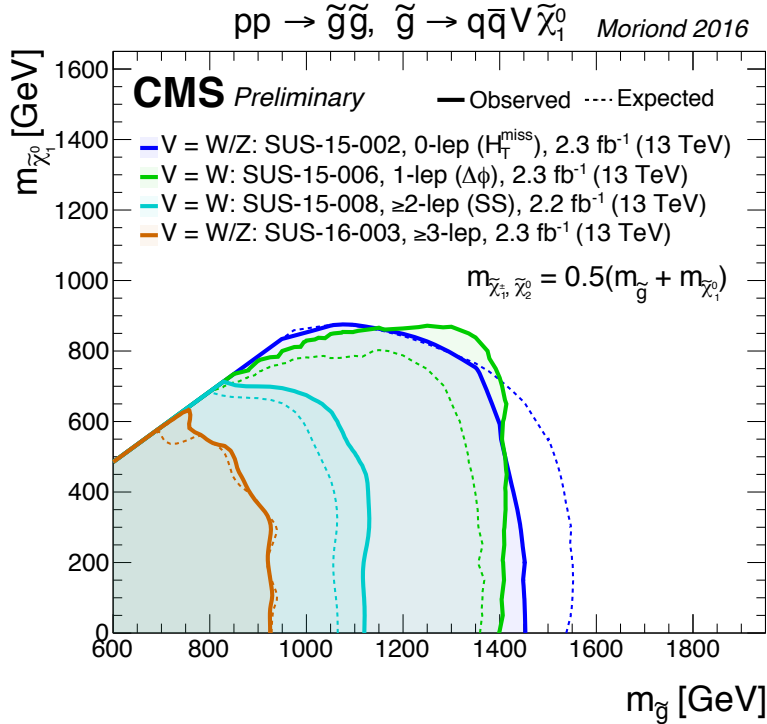


FIGURE 7.6: Exclusion curves in the gluino-neutralino mass plane for the T5qqqqVV model [91]. The green line represents the limits set by this analysis. Two analyses target the T5q<sup>4</sup>WW model, while the more inclusive T5qqqqVV is covered by the other two.



## Chapter 8

# Conclusion

A search for new physics beyond the Standard Model has been performed in the single lepton final state, requiring zero b-tagged jets, a high jet multiplicity and missing transverse energy. The targeted signal model is a simplified model with pair produced gluinos, undergoing a cascade decay to two neutralinos, which are considered to be stable, accompanied by several first and second generation quark jets and one electron or muon. The two stable neutralinos and a neutrino coming from a leptonic W boson decay introduce a sizable amount of  $\cancel{E}_T$ . Together with the expected large hadronic activity from the jets, sensitivity in the tails of kinematic distributions is high enough to probe for gluinos in the TeV range.

First, a robust data driven background prediction method was developed. The  $R_{CS}$  method for events coming from W+jets and  $t\bar{t}$ +jets processes closes well in simulations. The discriminative  $\Delta\phi(W, \ell)$  variable is used to measure  $R_{CS}$  in separate sideband regions for each Standard Model background process. The event yields in control regions are then scaled to the expected yields in signal regions using the obtained  $R_{CS}$  values. Yields in the sideband and control regions have to be corrected for events coming from QCD multijets. These events are estimated using polarization information of leptons from W boson decays, expressed through the  $L_P$  variable. An alternative approach, using the angle between jets and  $\cancel{E}_T$  in the transverse plane, was developed to check the validity of the method. Backgrounds from residual other background processes were directly taken from simulated samples. All methods were validated in simulation and data.

Several sources of systematic uncertainties of the background prediction have been studied. The largest uncertainties arise from possible residual dependencies of  $R_{CS}$  on the jet multiplicity, potential mismodeling of the dileptonic fraction of  $t\bar{t}$ +jets events in simulation and the limited number of events in simulated samples. Systematic uncertainties of

simulated signal events have been studied as well. Here, the largest contributions come from jet energy correction uncertainties and potential mismodeling of jet  $p_T$  spectra. Other uncertainties are below the 5% level.

Data from the CMS experiment taken in the 2015 run of the CERN LHC at a center of mass energy of 13 TeV have been analyzed. The dataset corresponds to an integrated luminosity of  $2.3\text{fb}^{-1}$ . No significant excess of data over the estimated Standard Model background was observed. Therefore, a frequentistic method was used to set limits on the production cross section in the gluino neutralino mass plane at the 95% confidence level. Previous limits on the gluino mass are extended to up to 1400 GeV, while neutralinos are excluded to up to 850 GeV.

The analysis was approved by the CMS collaboration on March 8th 2016. Results were presented at the *Rencontres de Moriond* 2016 conference.

# Appendices



# Appendix A

## Sideband region plots

Comparison of simulation and data of the major kinematic observables in the inclusive sideband regions are shown here. Simulation is scaled to an integrated luminosity of  $2.3\text{fb}^{-1}$ . Figure A.1 shows the sideband for measuring  $R_{\text{CS}}$  of  $W$ +jets events, requiring three to four jets and vetoing b-tagged jets,  $H_{\text{T}} > 500$  GeV and  $L_{\text{T}} > 250$  GeV in the muon channel. Although it is not used in this analysis, the electron channel is shown in Fig. A.2.

Figure A.3 and A.4 show the sideband for measuring  $R_{\text{CS}}$  of  $t\bar{t}$  + jets events, requiring four to five jets with one b-tagged jet,  $H_{\text{T}} > 500$  GeV and  $L_{\text{T}} > 250$  GeV, for muons and electrons.

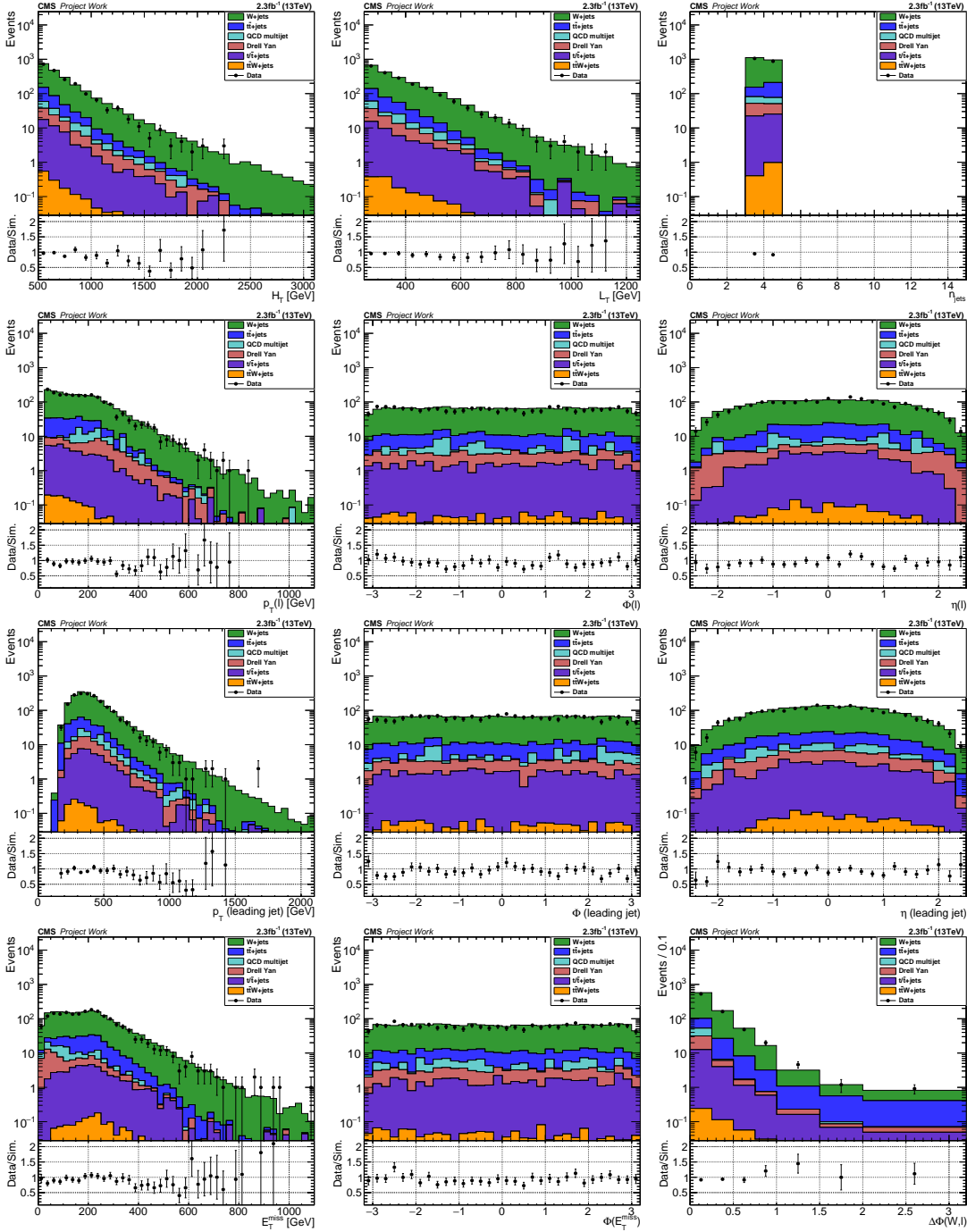


FIGURE A.1: Kinematic observables in the muon final state of the 3-4 jets sideband region.

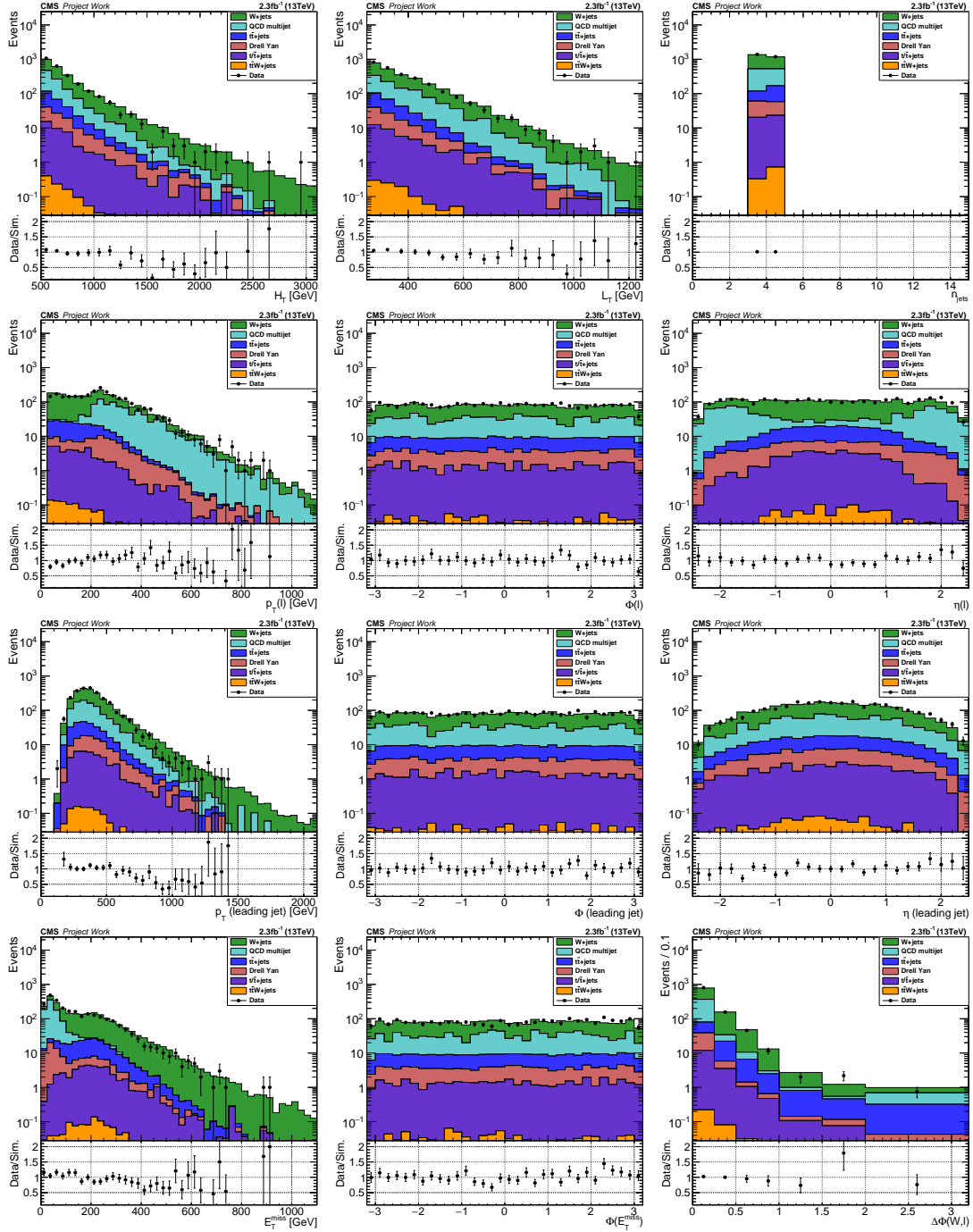


FIGURE A.2: Kinematic observables in the electron final state of the 3-4 jets sideband region.

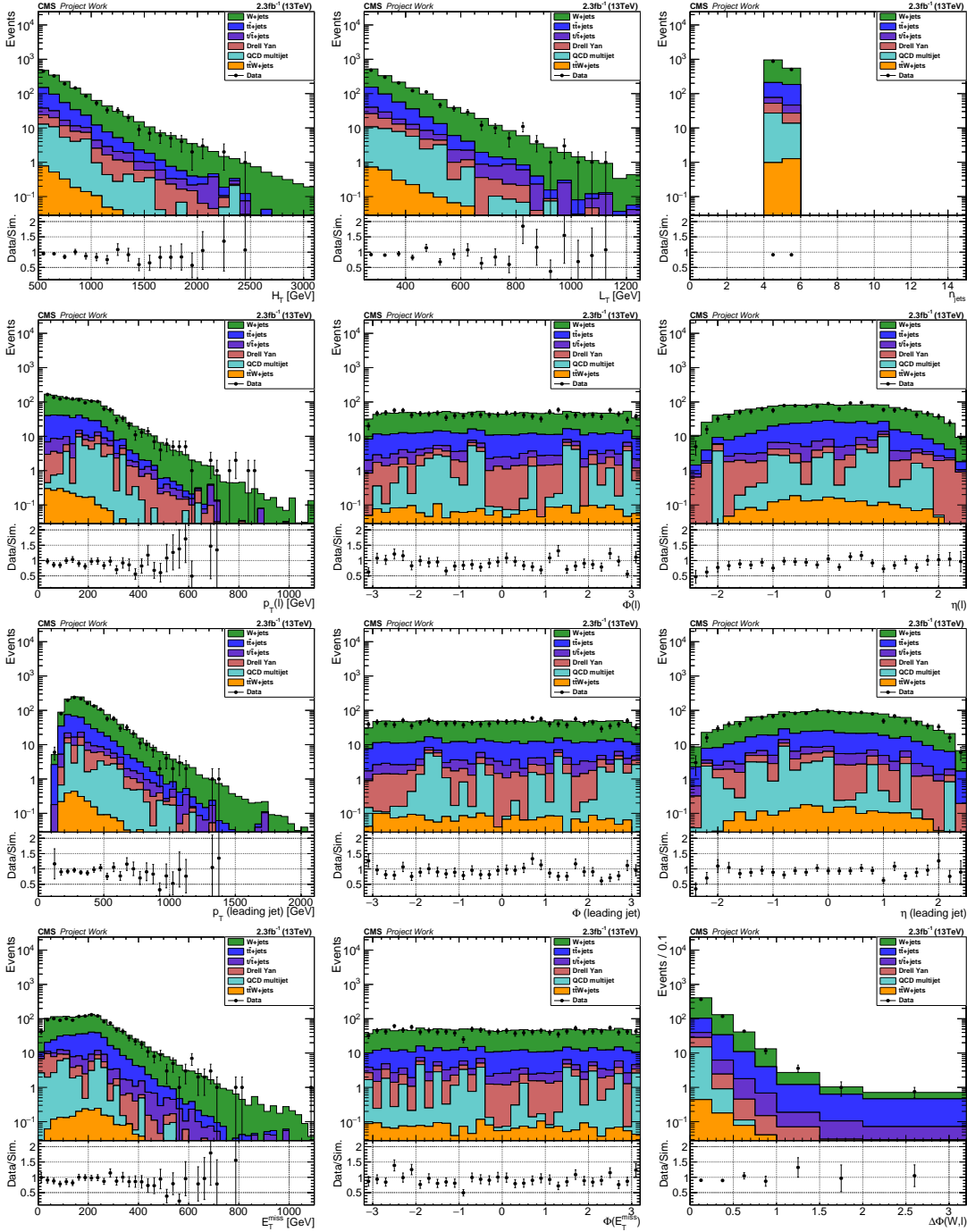


FIGURE A.3: Kinematic observables in the muon final state of the 4-5 jets, 1b sideband region.



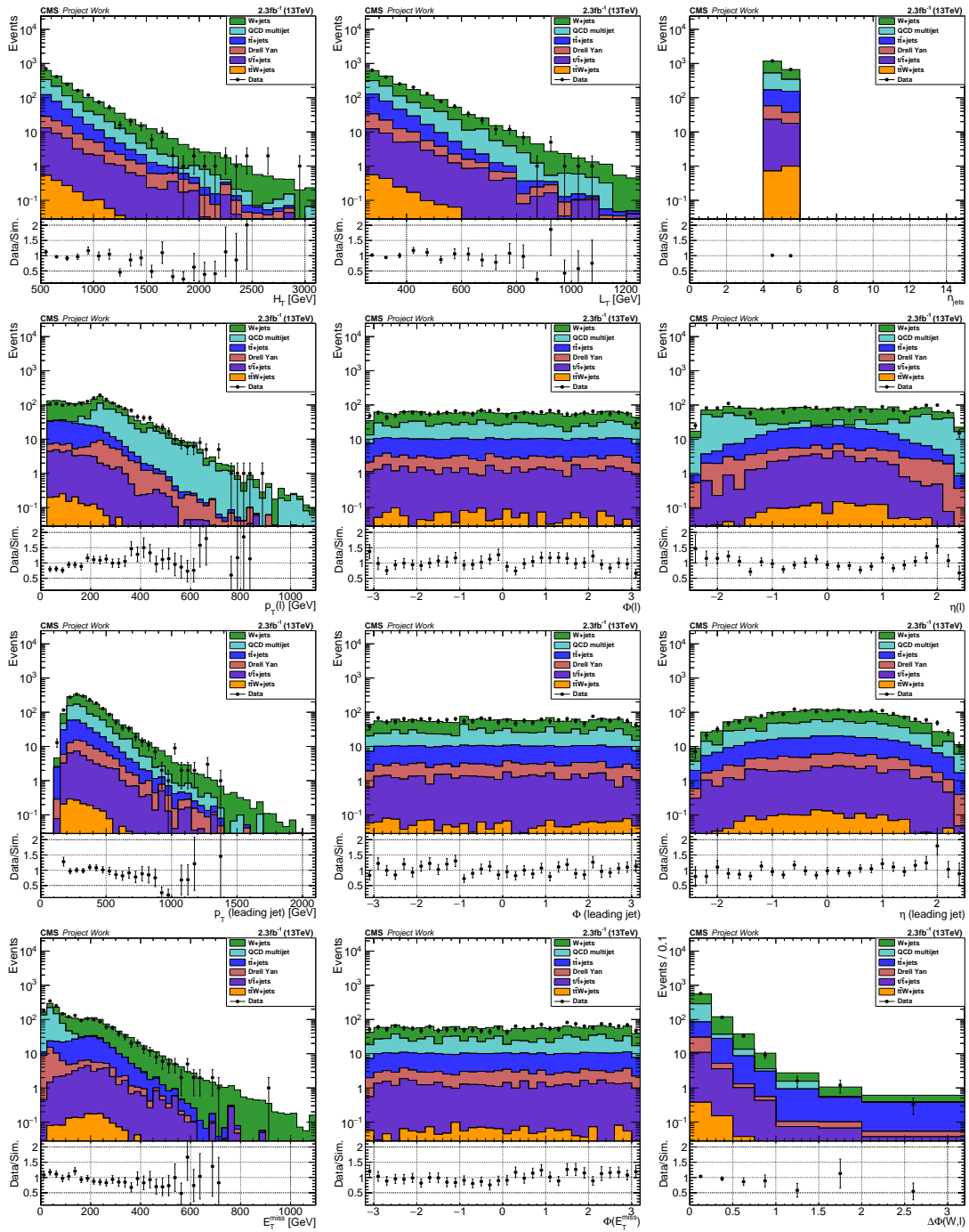


FIGURE A.4: Kinematic observables in the electron final state of the 4-5 jets, 1b sideband region.



# List of Figures

1.1	Overview of the particles contained in the framework of the SM. . . . .	3
1.2	Evolution of the gauge couplings. . . . .	9
1.3	Diagrams of loop corrections to the Higgs mass. . . . .	13
1.4	Exclusion limits on sparticle masses from LHC Run1. . . . .	15
1.5	Diagrams of gluino pair production at hadron colliders. . . . .	16
1.6	Cross sections of gluino pair production at the LHC. . . . .	17
1.7	Cross sections of SM processes at the LHC. . . . .	18
2.1	CERNs accelerator complex. . . . .	20
3.1	3D model of the CMS detector. . . . .	24
3.2	Cross section of a slice of the CMS detector. . . . .	25
3.3	The CMS pixel detector. . . . .	26
3.4	Sectional view of the CMS muon system. . . . .	28
4.1	B-tagging efficiency in $t\bar{t}$ + jets samples. . . . .	34
5.1	Diagrams of gluino mediated SUSY production. . . . .	38
5.2	Limits on gluino and neutralino masses from LHC Run 1. . . . .	38
5.3	B-tagged jet and jet multiplicity distributions. . . . .	38
5.4	Diagram of a W boson decaying into a charged lepton and the corresponding antineutrino or a quark / antiquark pair. . . . .	39
5.5	$\Delta\phi(W, \ell)$ distributions of SM background processes. . . . .	40
5.6	Distributions of kinematic observables. . . . .	41
5.7	$\Delta\phi(W, \ell)$ distributions with different $L_T$ requirements. . . . .	43
5.8	Trigger efficiencies in the $H_T$ leg. . . . .	45
5.9	Trigger efficiencies in the lepton leg. . . . .	45
5.10	Overview of mainband and sideband regions. . . . .	47
5.11	Results of the b-tag multiplicity fit. . . . .	48
5.12	Measured background composition in control regions. . . . .	48
5.13	QCD background estimation and validation using $L_P$ and $\Delta\phi(j, \cancel{E}_T)$ variables. . . . .	51
5.14	Diagram of a semi-leptonic $t\bar{t}$ + jets event. . . . .	52
5.15	$\Delta\phi(W, \ell)$ distribution of $t\bar{t}$ + jets events. . . . .	52
5.16	$R_{CS}$ values for $t\bar{t}$ + jets and W+jets events in simulated samples. . . . .	54
5.17	Diagram of a W+jets event. . . . .	55
5.18	Diagrams of other background processes. . . . .	56
6.1	$R_{CS}$ dependence on $L_T$ . . . . .	58

6.2	$R_{CS}$ plots using generated $\cancel{E}_T$ requirements. . . . .	58
6.3	Scatter plots of W+jets events. . . . .	59
6.4	$R_{CS}$ plots using generated and reconstructed information. . . . .	60
6.5	Minimum angular separation of jets and $\cancel{E}_T$ for $n$ leading jets. . . . .	61
6.6	$R_{CS}$ plots using $\min\Delta\phi(j_{1,2}, \cancel{E}_T)$ requirements. . . . .	62
6.7	$R_{CS}$ values for QCD multijet events. . . . .	63
6.8	Impact of b-tag scale factors on background prediction closure. . . . .	66
6.9	Linear fit to $R_{CS}$ values. . . . .	68
6.10	Systematic uncertainties of the background prediction. . . . .	69
6.11	Systematic uncertainties of the simulated signal. . . . .	72
6.12	Validation of the background estimation in simulation. . . . .	73
6.13	Validation of the background estimation in data. . . . .	73
7.1	Estimated background and observation in the signal regions. . . . .	76
7.2	Comparison of observed data with SM simulation. . . . .	77
7.3	Event display of a SUSY candidate event. . . . .	78
7.4	95% CL cross section limits for the T5qqqqWW model. . . . .	81
7.5	Most sensitive bin for limit setting. . . . .	82
7.6	CMS exclusion limits for the T5q <sup>4</sup> WW model. . . . .	82
A.1	Kinematic observables in the muon final state of the 3-4 jets sideband region. . . . .	88
A.2	Kinematic observables in the electron final state of the 3-4 jets sideband region. . . . .	89
A.3	Kinematic observables in the muon final state of the 4-5 jets, 1b sideband region. . . . .	90
A.4	Kinematic observables in the electron final state of the 4-5 jets, 1b sideband region. . . . .	91

# List of Tables

1.1	The chiral supermultiplets. . . . .	10
1.2	The gauge supermultiplets. . . . .	10
1.3	The additional particle content of the MSSM. . . . .	11
5.1	Event counts from simulation for backgrounds and signals. . . . .	42
5.2	Signal regions. . . . .	43
5.3	$R_{CS}$ values of $W$ +jets events in sideband regions. . . . .	49
5.4	$R_{CS}$ values of $t\bar{t}$ + jets events. . . . .	53
5.5	$R_{CS}$ values of $W$ +jets events . . . . .	56
6.1	QCD multijets contamination in the signal regions. . . . .	64
7.1	Results table of estimated and observed event yields. . . . .	75



# Bibliography

- [1] **CMS** Collaboration, S. Chatrchyan *et al.*, “Observation of a new boson at a mass of 125 GeV with the CMS experiment at the LHC”, *Phys. Lett.* **B716** (2012) 30–61, [arXiv:1207.7235](https://arxiv.org/abs/1207.7235) [hep-ex].
- [2] **ATLAS** Collaboration, G. Aad *et al.*, “Observation of a new particle in the search for the Standard Model Higgs boson with the ATLAS detector at the LHC”, *Phys. Lett.* **B716** (2012) 1–29, [arXiv:1207.7214](https://arxiv.org/abs/1207.7214) [hep-ex].
- [3] **Planck** Collaboration, P. A. R. Ade *et al.*, “Planck 2015 results. XIII. Cosmological parameters”, [arXiv:1502.01589](https://arxiv.org/abs/1502.01589) [astro-ph.CO].
- [4] Y. A. Golfand and E. P. Likhtman, “Extension of the Algebra of Poincare Group Generators and Violation of p Invariance”, *JETP Lett.* **13** (1971) , no. 8, 323–326.
- [5] J. Wess and B. Zumino, “Supergauge Transformations in Four-Dimensions”, *Nucl. Phys.* **B70** (1974) 39–50.
- [6] S. Dimopoulos and H. Georgi, “Softly Broken Supersymmetry and SU(5)”, *Nucl. Phys.* **B193** (1981) 150–162.
- [7] R. Barbieri, S. Ferrara, and C. A. Savoy, “Gauge Models with Spontaneously Broken Local Supersymmetry”, *Phys. Lett.* **B119** (1982) 343.
- [8] H. P. Nilles, “Supersymmetry, Supergravity and Particle Physics”, *Phys. Rept.* **110** (1984) 1–162.
- [9] H. E. Haber and G. L. Kane, “The Search for Supersymmetry: Probing Physics Beyond the Standard Model”, *Phys. Rept.* **117** (1985) 75–263.
- [10] S. Dawson, E. Eichten, and C. Quigg, “Search for Supersymmetric Particles in Hadron - Hadron Collisions”, *Phys. Rev.* **D31** (1985) 1581.
- [11] S. Weinberg, “A Model of Leptons”, *Phys. Rev. Lett.* **19** (1967) 1264–1266.
- [12] S. Node, “Go on a particle quest”, 2012. <https://sciencenode.org/spotlight/go-particle-quest-first-cern-hackfest.php>.

- [13] M. Maggiore, *A modern introduction to quantum field theory*. Oxford Master Series in Statistical, Computational, and Theoretical Physics. Oxford Univ., Oxford, 2005.
- [14] W. N. Cottingham and D. A. Greenwood, *An introduction to the standard model of particle physics*. Cambridge Univ. Press, Cambridge, 1998.
- [15] E. Fermi, “An attempt of a theory of beta radiation. 1.”, *Z. Phys.* **88** (1934) 161–177.
- [16] P. W. Higgs, “Broken Symmetries and the Masses of Gauge Bosons”, *Phys. Rev. Lett.* **13** (1964) 508–509.
- [17] F. Englert and R. Brout, “Broken Symmetry and the Mass of Gauge Vector Mesons”, *Phys. Rev. Lett.* **13** (1964) 321–323.
- [18] D. J. Gross and F. Wilczek, “Ultraviolet behavior of non-abelian gauge theories”, *Phys. Rev. Lett.* **30** (Jun, 1973) 1343–1346.
- [19] H. D. Politzer, “Reliable perturbative results for strong interactions?”, *Phys. Rev. Lett.* **30** (Jun, 1973) 1346–1349.
- [20] M. H. Goroff and A. Sagnotti, “The Ultraviolet Behavior of Einstein Gravity”, *Nucl. Phys.* **B266** (1986) 709–736.
- [21] P. J. E. Peebles, “Large scale background temperature and mass fluctuations due to scale invariant primeval perturbations”, *Astrophys. J.* **263** (1982) L1–L5.
- [22] **Super-Kamiokande** Collaboration, Y. Fukuda *et al.*, “Evidence for oscillation of atmospheric neutrinos”, *Phys. Rev. Lett.* **81** (Aug, 1998) 1562–1567.  
<http://link.aps.org/doi/10.1103/PhysRevLett.81.1562>.
- [23] P. Minkowski, “ $\mu \rightarrow e\gamma$  at a Rate of One Out of  $10^9$  Muon Decays?”, *Phys. Lett.* **B67** (1977) 421–428.
- [24] G. R. Farrar and P. Fayet, “Phenomenology of the Production, Decay, and Detection of New Hadronic States Associated with Supersymmetry”, *Phys. Lett.* **B76** (1978) , no. 5, 575–579.
- [25] S. P. Martin, “A Supersymmetry primer”, [arXiv:hep-ph/9709356](https://arxiv.org/abs/hep-ph/9709356) [hep-ph]. [Adv. Ser. Direct. High Energy Phys.18,1(1998)].
- [26] **MSSM Working Group** Collaboration, A. Djouadi *et al.*, “The Minimal supersymmetric standard model: Group summary report”, in *GDR (Groupement De Recherche) - Supersymetrie Montpellier, France, April 15-17, 1998*. 1998. [arXiv:hep-ph/9901246](https://arxiv.org/abs/hep-ph/9901246) [hep-ph].



- [27] J. Alwall, P. Schuster, and N. Toro, “Simplified Models for a First Characterization of New Physics at the LHC”, *Phys. Rev.* **D79** (2009) 075020, [arXiv:0810.3921 \[hep-ph\]](#).
- [28] **LHC New Physics Working Group** Collaboration, D. Alves, “Simplified Models for LHC New Physics Searches”, *J. Phys.* **G39** (2012) 105005, [arXiv:1105.2838 \[hep-ph\]](#).
- [29] **ATLAS** Collaboration, “ATLAS Supersymmetry (SUSY) searches”, 2016. <https://twiki.cern.ch/twiki/bin/view/AtlasPublic/SupersymmetryPublicResults>.
- [30] **CMS** Collaboration, “CMS Supersymmetry Physics Results”. Online, 2016. <https://twiki.cern.ch/twiki/bin/view/CMSPublic/PhysicsResultsSUS>.
- [31] R. Barbieri and G. F. Giudice, “Upper bounds on supersymmetric particle masses”, *Nucl. Phys. B* **306** (Aug., 1987) 63–76. 19 p.
- [32] P. Bechtle *et al.*, “Killing the cMSSM softly”, *Eur. Phys. J.* **C76** (2016) , no. 2, 96, [arXiv:1508.05951 \[hep-ph\]](#).
- [33] **CMS** Collaboration, V. Khachatryan *et al.*, “Search for Physics Beyond the Standard Model in Events with Two Leptons, Jets, and Missing Transverse Momentum in pp Collisions at  $\sqrt{s} = 8$  TeV”, *JHEP* **04** (2015) 124, [arXiv:1502.06031 \[hep-ex\]](#).
- [34] **ATLAS** Collaboration, G. Aad *et al.*, “Search for supersymmetry in events containing a same-flavour opposite-sign dilepton pair, jets, and large missing transverse momentum in 8 TeV pp collisions with the ATLAS detector”, *Eur. Phys. J.* **C75** (2015) , no. 7, 318, [arXiv:1503.03290 \[hep-ex\]](#). [Erratum: *Eur. Phys. J.* **C75**, no. 10, 463 (2015)].
- [35] M. Kramer, A. Kulesza, R. van der Leeuw, M. Mangano, S. Padhi, T. Plehn, and X. Portell, “Supersymmetry production cross sections in  $pp$  collisions at  $\sqrt{s} = 7$  TeV”, [arXiv:1206.2892 \[hep-ph\]](#).
- [36] C. Borschensky, M. Kramer, A. Kulesza, M. Mangano, S. Padhi, T. Plehn, and X. Portell, “Squark and gluino production cross sections in pp collisions at  $\sqrt{s} = 13, 14, 33$  and 100 TeV”, *Eur. Phys. J.* **C74** (2014) , no. 12, 3174, [arXiv:1407.5066 \[hep-ph\]](#).
- [37] W. Stirling, “Parton luminosity and cross section plots”, 2012. <http://www.hep.ph.ic.ac.uk/~wstirlin/plots/plots.html>.

- [38] N. Craig, “The State of Supersymmetry after Run I of the LHC”, in *Beyond the Standard Model after the first run of the LHC Arcetri, Florence, Italy, May 20-July 12, 2013*. 2013. arXiv:1309.0528 [hep-ph].
- [39] **UA1** Collaboration, G. Arnison *et al.*, “Experimental Observation of Isolated Large Transverse Energy Electrons with Associated Missing Energy at  $s^{1/2} = 540\text{-GeV}$ ”, *Phys. Lett.* **B122** (1983) 103–116. [,611(1983)].
- [40] **UA1** Collaboration, G. Arnison *et al.*, “Experimental Observation of Lepton Pairs of Invariant Mass Around  $95\text{-GeV}/c^2$  at the CERN SPS Collider”, *Phys. Lett.* **B126** (1983) 398–410.
- [41] CERN, “CERN’s accelerator complex”, 2015.  
<https://espace.cern.ch/acc-tec-sector/default.aspx>.
- [42] O. S. Bruning, P. Collier, P. Lebrun, S. Myers, R. Ostojic, J. Poole, and P. Proudlock, “LHC Design Report Vol.1: The LHC Main Ring”, 2004.
- [43] O. Buning, P. Collier, P. Lebrun, S. Myers, R. Ostojic, J. Poole, and P. Proudlock, “LHC Design Report Vol.2: The LHC infrastructure and general services”, 2004.
- [44] M. Benedikt, P. Collier, V. Mertens, J. Poole, and K. Schindl, “LHC Design Report Vol.3: The LHC injector chain”, 2004.
- [45] **CMS** Collaboration, S. Chatrchyan *et al.*, “The CMS experiment at the CERN LHC”, *JINST* **3** (2008) S08004.
- [46] **CMS** Collaboration, G. L. Bayatian *et al.*, “CMS physics: Technical design report Volume I: Detector Performance and Software”, 2006.
- [47] **CMS** Collaboration, G. L. Bayatian *et al.*, “CMS technical design report, volume II: Physics performance”, *J. Phys.* **G34** (2007) 995–1579.
- [48] T. Sakuma and T. McCauley, “Detector and Event Visualization with SketchUp at the CMS Experiment”, *J. Phys. Conf. Ser.* **513** (2014) 022032, arXiv:1311.4942 [physics.ins-det].
- [49] **CMS** Collaboration, M. S. Kim *et al.*, “CMS reconstruction improvement for the muon tracking by the RPC chambers”, *PoS RPC2012* (2012) 045, arXiv:1209.2646 [physics.ins-det]. [JINST8,T03001(2013)].
- [50] **CMS** Collaboration, “Particle-Flow Event Reconstruction in CMS and Performance for Jets, Taus, and MET”, 2009.

- [51] **CMS** Collaboration, “Commissioning of the Particle-flow Event Reconstruction with the first LHC collisions recorded in the CMS detector”, Tech. Rep. CMS-PAS-PFT-10-001, 2010. <https://cds.cern.ch/record/1247373>.
- [52] S. Baffioni, C. Charlot, F. Ferri, D. Futyan, P. Meridiani, I. Puljak, C. Rovelli, R. Salerno, and Y. Sirois, “Electron reconstruction in CMS”, *Eur. Phys. J.* **C49** (2007) , no. 4, 1099–1116.
- [53] **CMS** Collaboration, V. Khachatryan *et al.*, “Performance of Electron Reconstruction and Selection with the CMS Detector in Proton-Proton Collisions at  $s = 8$  TeV”, *JINST* **10** (2015) , no. 06, P06005, [arXiv:1502.02701](https://arxiv.org/abs/1502.02701) [[physics.ins-det](https://arxiv.org/abs/1502.02701)].
- [54] R. Frühwirth, “Application of Kalman filtering to track and vertex fitting”, *Nucl. Instrum. Meth.* **A262** (1987) , no. 2-3, 444–450.
- [55] **CMS** Collaboration, S. Chatrchyan *et al.*, “Description and performance of track and primary-vertex reconstruction with the CMS tracker”, *JINST* **9** (2014) , no. 10, P10009, [arXiv:1405.6569](https://arxiv.org/abs/1405.6569) [[physics.ins-det](https://arxiv.org/abs/1405.6569)].
- [56] W. Adam, R. Frühwirth, A. Strandlie, and T. Todorov, “Reconstruction of electrons with the Gaussian-sum filter in the CMS tracker at the LHC”, *Journal of Physics G: Nuclear and Particle Physics* **31** (July, 2005) N9–N20.
- [57] **CMS** Collaboration, S. Chatrchyan *et al.*, “Performance of CMS muon reconstruction in  $pp$  collision events at  $\sqrt{s} = 7$  TeV”, *JINST* **7** (2012) P10002, [arXiv:1206.4071](https://arxiv.org/abs/1206.4071) [[physics.ins-det](https://arxiv.org/abs/1206.4071)].
- [58] M. Cacciari, G. P. Salam, and G. Soyez, “The Anti-k(t) jet clustering algorithm”, *JHEP* **04** (2008) 063, [arXiv:0802.1189](https://arxiv.org/abs/0802.1189) [[hep-ph](https://arxiv.org/abs/0802.1189)].
- [59] **CMS** Collaboration, S. Chatrchyan *et al.*, “Determination of Jet Energy Calibration and Transverse Momentum Resolution in CMS”, *JINST* **6** (2011) P11002, [arXiv:1107.4277](https://arxiv.org/abs/1107.4277) [[physics.ins-det](https://arxiv.org/abs/1107.4277)].
- [60] **CMS** Collaboration, S. Chatrchyan *et al.*, “Identification of b-quark jets with the CMS experiment”, *JINST* **8** (2013) P04013, [arXiv:1211.4462](https://arxiv.org/abs/1211.4462) [[hep-ex](https://arxiv.org/abs/1211.4462)].
- [61] **CMS** Collaboration, S. Chatrchyan *et al.*, “Missing transverse energy performance of the CMS detector”, *JINST* **6** (2011) P09001, [arXiv:1106.5048](https://arxiv.org/abs/1106.5048) [[physics.ins-det](https://arxiv.org/abs/1106.5048)].
- [62] **CMS** Collaboration, V. Khachatryan *et al.*, “Performance of the CMS missing transverse momentum reconstruction in  $pp$  data at  $\sqrt{s} = 8$  TeV”, *JINST* **10** (2015) , no. 02, P02006, [arXiv:1411.0511](https://arxiv.org/abs/1411.0511) [[physics.ins-det](https://arxiv.org/abs/1411.0511)].

- [63] **CMS** Collaboration, S. Chatrchyan *et al.*, “Search for supersymmetry in pp collisions at  $\sqrt{s}=8$  TeV in events with a single lepton, large jet multiplicity, and multiple b jets”, *Phys. Lett.* **B733** (2014) 328–353, [arXiv:1311.4937 \[hep-ex\]](#).
- [64] R. M. Barnett, J. F. Gunion, and H. E. Haber, “Gluino Decay Patterns and Signatures”, *Phys. Rev.* **D37** (1988) , no. 7, 1892–1907.
- [65] **CMS** Collaboration, S. Chatrchyan *et al.*, “Search for new physics in events with same-sign dileptons and jets in pp collisions at 8 TeV”, *JHEP* **01** (2014) 163, [arXiv:1311.6736](#). [Erratum: *JHEP*01,014(2015)].
- [66] J. Alwall, R. Frederix, S. Frixione, V. Hirschi, F. Maltoni, O. Mattelaer, H. S. Shao, T. Stelzer, P. Torrielli, and M. Zaro, “The automated computation of tree-level and next-to-leading order differential cross sections, and their matching to parton shower simulations”, *JHEP* **07** (2014) 079, [arXiv:1405.0301 \[hep-ph\]](#).
- [67] E. Re, “Single-top Wt-channel production matched with parton showers using the POWHEG method”, *Eur. Phys. J.* **C71** (2011) 1547, [arXiv:1009.2450 \[hep-ph\]](#).
- [68] T. Sjstrand, S. Ask, J. R. Christiansen, R. Corke, N. Desai, P. Ilten, S. Mrenna, S. Prestel, C. O. Rasmussen, and P. Z. Skands, “An Introduction to PYTHIA 8.2”, *Comput. Phys. Commun.* **191** (2015) 159–177, [arXiv:1410.3012 \[hep-ph\]](#).
- [69] N. Kidonakis, “NNLL threshold resummation for top-pair and single-top production”, *Phys. Part. Nucl.* **45** (2014) , no. 4, 714–722, [arXiv:1210.7813 \[hep-ph\]](#).
- [70] Artur Lobanov, “Trigger efficiencies”. Private communication, 2015.
- [71] **CMS** Collaboration, “Search for supersymmetry in events with one lepton in proton-proton collisions at  $\sqrt{s}=13$  TeV with the CMS experiment”, Tech. Rep. CMS-PAS-SUS-15-006, CERN, Geneva, 2016. <http://cds.cern.ch/record/2140638>.
- [72] B. Efron, “Bootstrap Methods: Another Look at the Jackknife”, in *Breakthroughs in Statistics*, pp. 569–593. Springer New York, New York, NY, 1992.
- [73] D. Handl, “Background estimation for searches for supersymmetry in the single lepton final state in 13 TeV pp collisions”, Master’s thesis, 2016.
- [74] **CMS** Collaboration, S. Chatrchyan *et al.*, “Measurement of differential top-quark pair production cross sections in pp collisions at  $\sqrt{s} = 7$  TeV”, *Eur. Phys. J.* **C73** (2013) , no. 3, 2339, [arXiv:1211.2220 \[hep-ex\]](#).

- [75] **CMS** Collaboration, V. Khachatryan *et al.*, “Measurement of the differential cross section for top quark pair production in pp collisions at  $\sqrt{s} = 8$  TeV”, *Eur. Phys. J.* **C75** (2015) , no. 11, 542, [arXiv:1505.04480](#) [hep-ex].
- [76] **CMS** Collaboration, “CMS Luminosity Measurement for the 2015 Data Taking Period”, Tech. Rep. CMS-PAS-LUM-15-001, CERN, Geneva, 2016.  
<https://cds.cern.ch/record/2138682>.
- [77] S. Agostinelli and others, “GEANT4: A Simulation toolkit”, *Nucl. Instrum. Meth.* **A506** (2003) , no. 3, 250–303.
- [78] R. Rahmat, R. Kroeger, and A. Giammanco, “The fast simulation of the CMS experiment”, *J. Phys. Conf. Ser.* **396** (2012) , no. 6, 062016.
- [79] D. Kovalskyi, M. Tadel, A. Mrak-Tadel, B. Bellenot, V. Kuznetsov, C. D. Jones, L. Bauerdick, M. Case, J. Mülmenstädt, and A. Yagil, “Fireworks: A physics event display for CMS”, *J. Phys. Conf. Ser.* **219** (May, 2010) 032014.
- [80] A. L. Read, “Presentation of search results: The CL(s) technique”, *J. Phys.* **G28** (2002) 2693–2704. [,11(2002)].
- [81] G. Cowan, K. Cranmer, E. Gross, and O. Vitells, “Asymptotic formulae for likelihood-based tests of new physics”, *The European Physical Journal C* **71** (Feb., 2011) 1–19.
- [82] **ATLAS and CMS** Collaboration, “Procedure for the LHC Higgs boson search combination in summer 2011”, ATL-PHYS-PUB-2011-011; CMS-NOTE-2011-005.
- [83] K. Cranmer, “Statistical challenges for searches for new physics at the LHC”, [arXiv:physics/0511028](#). [http://www.physics.ox.ac.uk/phystat05/proceedings/files//Cranmer\\_LHCStatisticalChallenges.ps](http://www.physics.ox.ac.uk/phystat05/proceedings/files//Cranmer_LHCStatisticalChallenges.ps).
- [84] T. Junk, “Confidence level computation for combining searches with small statistics”, *Nucl. Instrum. Meth.* **A434** (1999) 435–443, [arXiv:hep-ex/9902006](#) [hep-ex].
- [85] **ATLAS** Collaboration, G. Aad *et al.*, “Search for squarks and gluinos in events with isolated leptons, jets and missing transverse momentum at  $\sqrt{s} = 8$  TeV with the ATLAS detector”, *JHEP* **04** (2015) 116, [arXiv:1501.03555](#) [hep-ex].
- [86] **ATLAS** Collaboration, “Search for squarks and gluinos in final states with jets and missing transverse momentum at  $\sqrt{s} = 13$  TeV with the ATLAS detector”, Tech. Rep. ATLAS-CONF-2015-062, CERN, Geneva, Dec, 2015.  
<https://cds.cern.ch/record/2114828>.

- [87] **ATLAS** Collaboration, “Search for gluinos in events with an isolated lepton, jets and missing transverse momentum at  $\sqrt{s}=13$  TeV with the ATLAS detector”, Tech. Rep. ATLAS-CONF-2015-076, CERN, Geneva, Dec, 2015.  
<https://cds.cern.ch/record/2114848>.
- [88] **CMS** Collaboration, “Search for supersymmetry in the multijet and missing transverse momentum channel in pp collisions at 13 TeV”, Tech. Rep. CMS-PAS-SUS-15-002, CERN, Geneva, 2015.  
<https://cds.cern.ch/record/2114817>.
- [89] **CMS** Collaboration, “Search for SUSY in same-sign dilepton events at  $\sqrt{s}=13$  TeV”, Tech. Rep. CMS-PAS-SUS-15-008, CERN, Geneva, 2015.  
<https://cds.cern.ch/record/2114813>.
- [90] **CMS** Collaboration, “Search for SUSY with multileptons in 13 TeV data”, Tech. Rep. CMS-PAS-SUS-16-003, CERN, Geneva, 2016.  
<https://cds.cern.ch/record/2140637>.
- [91] M. F. Sevilla, “SUSY searches in leptonic final states at CMS”, Recontres de Moriond, QCD and High Energy Interactions, 2016.  
<http://moriond.in2p3.fr/QCD/2016/MondayMorning/Sevilla.pdf>.